New Methods for Investigating the Interplay of Photoluminescence Intermittency and Local Dielectric Constant

Chelsea Hess Haupt

A dissertation
submitted in partial fulfillment of the
requirements for the degree of

Doctor of Philosophy

University of Washington

2015

Reading Committee:

Philip Reid, Chair

Munira Khalil

Daniel Chiu

Program Authorized to Offer Degree:
Department of Chemistry

University of Washington

Abstract

New Methods for Investigating the
Interplay of Photoluminescence Intermittency
and Local Dielectric Constant

Chelsea Hess Haupt

Chair of the Supervisory Committee:
Professor Philip Reid
Department of Chemistry

New experimental and data analysis methods for investigating the influence of local environment on the photoluminescence intermittency (PI) or "blinking" exhibited by single luminophores are presented. Specifically, the relationship between PI and local dielectric constant (ε) for nile red (NR) embedded in poly(vinylidene fluoride) (PVDF) is determined using these new methods.

Experimentally, quasi-single molecule (SM) microscopy is used to spatially resolve the distribution of ε in polymer films. By measuring the solvatochromic emission from NR, a direct correlation between the emission maximum and ε is established and used to measure the spatial varaition in ε for PVDF. The effect of sample annealing is explored, with non-annealed films exhibiting much larger ε distributions in comparison to annealed films. In addition, a decrease in the average ε with annealing time is observed and attributed to a phase transformation of PVDF from γ- to β-phase.

New data analysis methods employing cumulative distribution functions (CDFs) are also presented. These techniques allow for the statistical analysis of PI without first assuming a parametric form for the underlying probability distribution function (PDF) describing the duration of emissive and non-emissive events. For NR in PVDF, changes in PI with variation in ε are observed and shown to be consistent with a

photoinduced electron transfer mechanism. The experimental and analytical methods outlined here should prove useful in SM studies of guest-host materials designed to elucidate the role of host environment on PI exhibited by the guest luminophore.

TABLE OF CONTENTS

List of Figures

List of Tables

ACKNOWLEDGMENTS

First, I want to express my sincere gratitude to my advisor Professor Phil Reid. Phil is an incredibly wise, patient, creative, and supportive advisor, whom I feel honored to have as a mentor. Thank you Phil for not only believing in me as a chemist but as a teacher. To Dr. Colleen Craig, thank you for providing great advice and encouragement. To my committee members Professors Munira Khalil, Daniel Chiu, and Nikolai Tolich, thank you for offering kind guidance throughout this journey.

To all of my coworkers, I am forever indebted to you for your help and ideas. Dr. Erin Riley, thank you for being my mentor and teaching me so much. Patrick Whitham, I have so very much enjoyed our productive and not so productive conversations! Dr. Angela Rudolph, although our time as coworkers was short, I am forever grateful for all of your help with my projects (this thesis in particular) and for always being so gracious.

Next, to my best friend and fellow grad student Audra Johansen, you were there through the highs and the lows. Many tears were shed on your shoulder but they always quickly turned to laughter. Thank you for everything!

Finally, and most importantly, I thank my family. With unyielding support and enthusiasm you have shaped me into the woman I am today. Thank you Dad for always answering my phone calls. Your ability to deal with my crazy will never be matched! Mom, you are without a doubt the greatest role model that I have. I am so honored to be your daughter but more importantly your friend. Richard, you are my brother. Thank you for always making me laugh. To the Haupts, thank you for accepting me into your family and encouraging me to achieve my goals. To my

wonderful husband Stephen, I thank you. The amount of love and support that you give me everyday is unbelievable. I truly would not have made it to this point without you and I thank you for always believing in me! Last, I thank my dog Chica for the countless hours of cuddling and companionship, including the hours spent trying to distract me from writing, reading literature and studying. Luckily, it didn't always work!

DEDICATION

To my guardian angels, Nana and Greymare.

I miss and love you so much.

Chapter 1

INTRODUCTION

NEW TOOLS FOR ELUCIDATING THE ENVIRONMENTAL ORIGINS OF SINGLE MOLECULE PHOTOLUMINESCENCE INTERMITTENCY

This chapter has been submitted to Chemical Physics Letters as an invited Frontiers article.

1.1 New Tools for Elucidating the Environmental Origins of Single Molecule Photoluminescence Intermittency

Following the optical detection of single molecules (SM) in 1991,[1] SMs have been extensively employed as probes of complex materials reporting on molecular-length scales.[2] A long-standing promise of SM studies is the ability to study chemistry that is largely obscured in ensemble measurements. By studying the chemistry of individual molecules, novel and/or infrequent behavior becomes readily observable. This ability is especially attractive for studies of complex guest-host systems where the details of the local environment around a SM can have a profound effect on the chemistry exhibited by the guest molecule.

We are particularly interested in using SM techniques to interrogate guest-host organic electro-optical (EO) materials. Applications of EO devices are currently limited by photodecomposition of the chromophore, even in oxygen deficient environments.[3] Identifying and subsequently blocking the operative photodecomposition pathways is essential in the development of more robust EO materials. Photodecomposition is ubiquitous in SM studies, with the abrupt or "single step" loss of emission being a key experimental check that one is interrogating SMs. However, the rate and mechanism of photodecomposition is highly dependent on the nature of the luminophore and surrounding environment. For example, multi-chromophore systems have been used to probe whether subsequent photobleaching that appears to occur in a stepwise manner is sequential[4,5] while other studies have concluded that a two-step photolysis is responsible for photobleaching[6] and that suppression of this process is possible.[7]

Our research has focused on measuring photoluminescence intermittency (PI) or "blinking" of SMs and using this information to test various hypotheses for luminophore photodecomposition. PI is characterized by alternating periods of SM emission and non-emission, with non-emissive events corresponding to the population of "dark states" that may serve as gateways to photodecomposition (Figure 1.1).[8] The

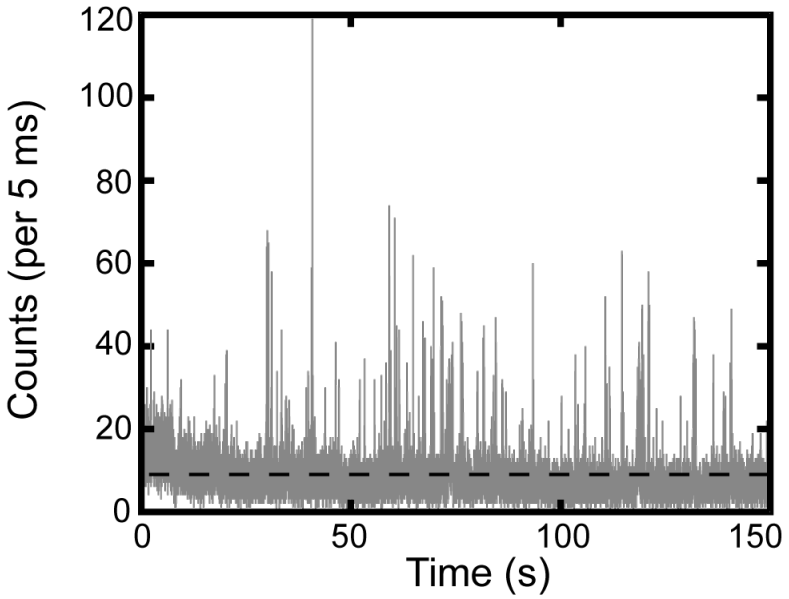

Figure 1.1: Fluorescence time trace of a single molecule of NR embedded in poly(vinylidene fluoride) (PVDF). The emission threshold is shown as the black dotted line.

simplest model for PI involves the production and decay of a dark state corresponding to a triplet-state of the luminophore.[9] In SM studies, the rate constant for dark state population and decay are determined by analyzing histograms of the emissive and non-emissive event durations. Evidence for triplet-state formation is therefore found through the correspondence of the dark-state lifetime as measured in a SM experiment with the ensemble measured triplet-state lifetime.[10]

While a handful of studies have observed a correlation between the dark-state and triplet-state lifetime, the vast majority of SM studies have not. Specifically, emissive and non-emissive event duration histograms are found to correspond to complex distribution functions that are inconsistent with triplet-state formation and decay. Power-law distributions of the form $P(t)=At^{-\alpha}$ have found wide application for modeling these more-complex distributions.[11] Power-law distributions are consistent with an evolution in the rate constants for dark state production and decay on the timescale of the experiment.[12] For organic luminophores, the prevailing explanation why systems exhibit power-law distributions is the formation of a radical species through electron transfer to the host. In this etiology for PI, the distribution of electron trapping sites available within the host provides a change in the rate constant for electron transfer and corresponding dark-state formation.[2,13–16] Charge recombination then returns the molecule to an emissive state. Alternative hypotheses have been advanced for PI including conformational flexibility,[17,18] spectral diffusion,[19,20] and proton transfer.[21]

A critical step in evaluating any proposed mechanism for PI is elucidating the role of the host in promoting dark-state formation and decay. For example, our group previously compared the PI exhibited by violamine R (VR) incorporated into potassium acid phthalate (KAP) crystals and poly(vinyl alcohol) (PVA) films. It was found that the PI exhibited by VR demonstrated opposing trends with changing temperature in the two hosts.[14,22] This observation was interpreted as two different mechanisms being responsible for PI depending on environment. Specifically, electron transfer was

found to be the origin of PI in PVA while proton transfer is responsible for the PI exhibited in KAP. Further evidence supporting an electron-transfer mechanism for PI exhibited by organic luminophores embedded in polymers includes the observation of a decrease in the power-law exponent used to describe the non-emissive event duration histograms with an increase in dielectric constant (ε) of the host.[15] This finding is consistent with the stabilization of the charge-transfer state in higher dielectric environments providing for longer non-emissive event durations.[15] This trend was further explored in the work of Issac *et al.* on quantum dot PI.[16] However, these studies were limited by the modification of ε being accomplished through changing the chemical composition of the host.[15,16] That said, these early studies have brought to light some interesting questions. Can methods be developed that provide an easy way to characterize the distribution of local environments provided by the host? Can one connect changes in PI with changes in local environment in a way that allows for the application of statistical methods to characterize the extent of PI alteration with environment?

We have developed experimental and analytical techniques to directly link changes in PI with local environment, and have used these techniques to study the guest-host system of nile red (NR) embedded in films of poly(vinylidene fluoride) (PVDF). PVDF is a semi-crystalline polymer that is of interest for its piezo- and pyroelectric properties. This polymer is known to exhibit multiple phases of differing polarity, and external perturbations such as annealing or the application of an electric field can promote transformation between these phases providing a unique opportunity to explore the role of ε on PI.[23] By employing films in which NR is incorporated at quasi-single molecule (quasi-SM) concentrations, and using the bathochromic shift in emission with an increase in ε exhibited by NR,[24–27] we have spatially resolved the dielectric environments present within the various phases of PVDF.[28] We have also been able to investigate the impact of annealing on both the polymorphic phase and ε exhibited by the NR/PVDF films.[29,30] In addition, SM techniques have been

used to directly investigate the impact of ε on PI,[29] and we have developed a new statistical method for analyzing PI data.[31] This thesis presents a review of the quasi-SM techniques and the new PI analysis method. The tools presented here have allowed for a thorough investigation of NR in PVDF, but more importantly they should find wide application in the study of other guest-host materials.

1.2 Quasi-Single Molecule Microscopy

For NR/PVDF a critical first step in investigating the role of the host on PI is measurement of the distribution of dielectric (ε) environments within the polymer. Previous methods for measuring ε in polymer films were limited by spatial resolution on the order of micrometers (broad-band dielectric spectroscopy),[32] the requirement for extremely thin films (nanoscale dielectric microscopy),[33] and the ability to measure ε only at the surface of the polymer film (frequency modulation electrostatic force microscopy).[34,35] To overcome these limitations, we developed a new technique termed quasi-SM microscopy that allows for the measurement of dielectric distributions in polymer films. This technique involves doping the polymer of interest with probe molecules at concentrations that provide ~2 molecules in the focal volume. This concentration is roughly 100 times larger than that used in traditional SM studies, corresponding to a luminophore number density of ~10 molecules/μm^2. Using standard fluorescence confocal microscopy techniques, we are able to rapidly measure the distribution of ε present within a polymer film as subsequently described.[28] NR exhibits a ~100 nm bathochromic shift in the peak emission wavelength with a change in ε from 2 to 32.[24–27] Measurement of the NR emission maximum was performed and converted to energy (in wavenumbers). This energy was then converted to ε by employing the following relationship:[28]

$$\Delta E\left(cm^{-1}\right) = 1.077 \times 10^4 e^{-0.8\varepsilon} + 1.67 \times 10^4 e^{-5\times 10^{-4}\varepsilon} \tag{1.1}$$

This relationship allows for conversion of NR emission maxima images to images of

local dielectric. We chose PVDF as the polymer host since it exhibits a wide range of dielectric environments depending on polymorphic phase. The three dominant phases of PVDF are denoted α, β and γ. The α-phase is the most common and is non-polar with a cis-trans conformation. The β-phase is polar and ferroelectric with an all-trans conformation. Finally, the γ-phase is an intermediate between the α- and β-phases with a kinked all-trans conformation resulting in this phase being less polar than the β-phase. The phases expressed by PVDF are dependent on processing conditions, with interconversion between phases promoted through external perturbation such as electric-field poling, annealing, or mechanical straining.[23]

Our initial studies of the NR/PVDF guest-host system involved spatial mapping of the distribution of ε within a β-phase film. By measuring the emission wavelength maximum of NR as a function of spatial position within the polymer film, spatial maps of ε were generated as shown in Figure 1.2. The figure demonstrates the variation in emission wavelength maximum and correspondingly ε in a β-phase PVDF film. The distributions presented in Figure 1.2 help to illustrate the relatively unique dielectric environment provided by PVDF, with the observation of a heavy tailed distribution of ε. In order to further investigate the distribution of ε observed in PVDF, annealing was used to transition between polymorphic phases of PVDF while the corresponding changes in dielectric environment were measured as shown in Figure 1.3 and 1.4. Figure 1.3 presents spatial maps of the variation in ε across the film for annealed and non-annealed films while Figure 1.4 illustrates the impact of annealing on the distributions of ε. This large variation in the distribution of ε between annealed and non-annealed films was attributed to the non-annealed films being primarily in the γ-phase while annealed films are primarily in the β-phase. This result allowed for us to present the first visualization of the interconversion from γ- to β-phase in a PVDF film.

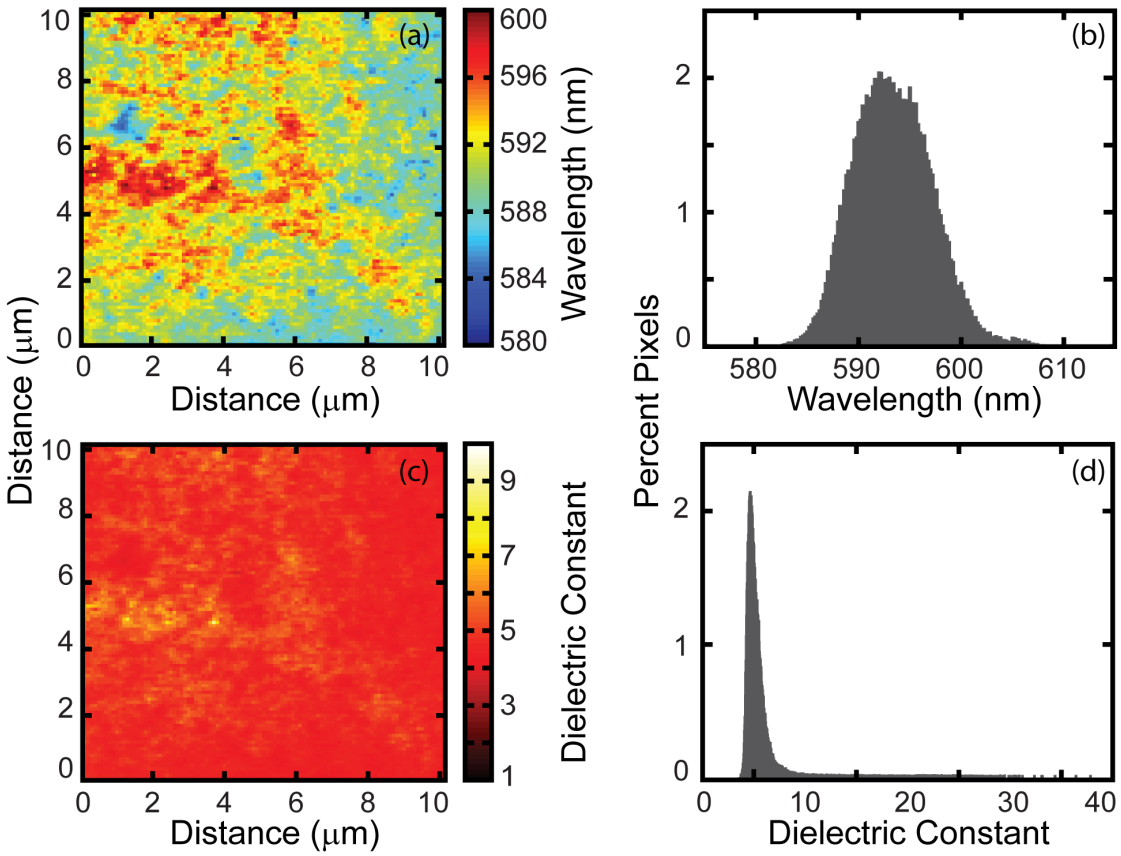

Figure 1.2: Images and plots showing the spatial variation in wavelength and dielectric constant (ε) for ∼30 μm thick films of NR/ PVDF. Image (a) corresponds to the variation in NR emission wavelength maximum versus position in the film while (b) shows the distribution of wavelength maximum for ten 10 × 10 μm image scans. Image (c) corresponds to the variation in ε for the same film as (a) with (d) representing the distribution of ε from the ten 10 × 10 μm image scans. Emission intensity is separated by a 600-nm short pass dichroic mirror and is collected on two separate APDs. The ratio of the intensities (reflected to transmitted) is transformed first to wavelength and then to ε to create the images and plots presented here.

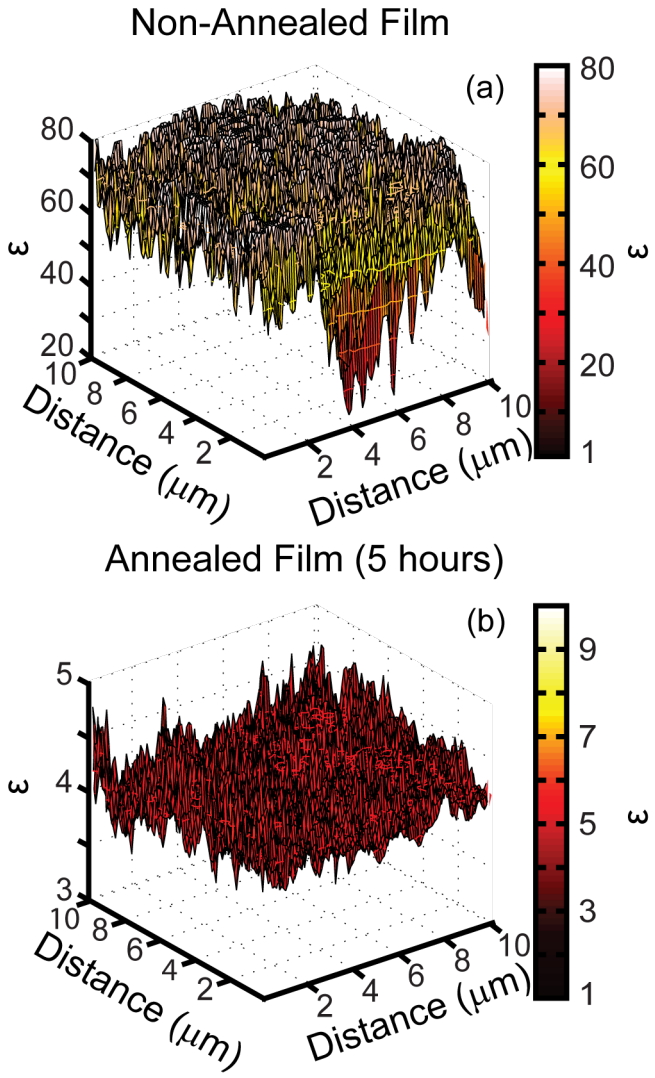

Figure 1.3: Representation of the spatial variation of dielectric constants (ε) present in quasi-SM non-annealed (a) and annealed (b) NR/PVDF films. From the difference in ε scale between the non-annealed and annealed films, it is clear that the larger ε values are a consequence of the film not being annealed.

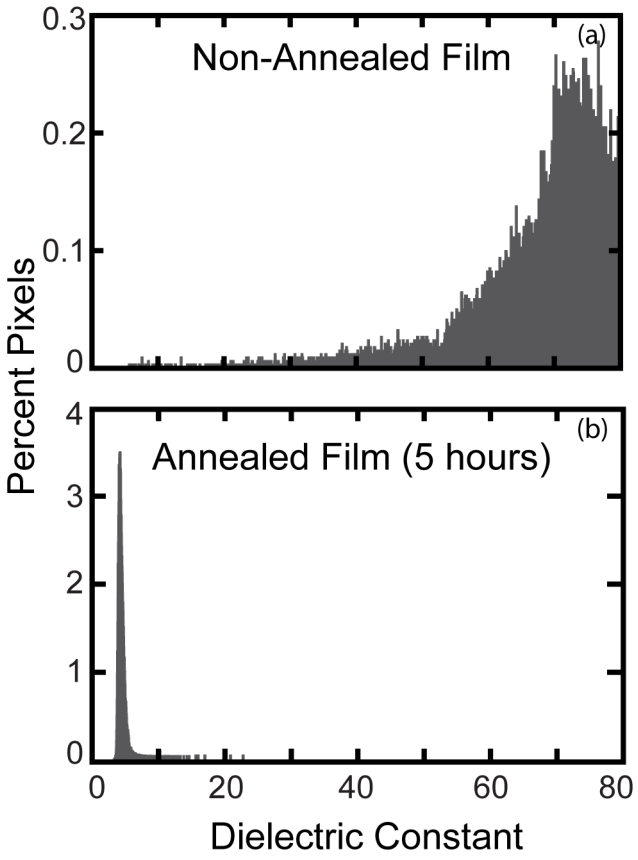

Figure 1.4: Distributions of the dielectric constant (ε) present in quasi-SM non-annealed γ-phase (a) and annealed β-phase (b) NR/PVDF films. The shifting and narrowing of the ε distribution between non-annealed and annealed films is believed to be a consequence of the film being in the γ-phase with transformation into the β-phase occurring upon annealing.

1.3 A More Robust Method for Analyzing PI Data

As mentioned previously, in many SM studies emissive and non-emissive event distributions are modeled using a power-law distribution. Correspondingly, variations in environment which impact the emissive statistics should be reflected by a change in the power-law distribution. However, teasing out statistically-significant changes in emissive statistics that accompany environmental perturbations by analyzing power-law distributions can be extremely difficult. Instead, a method for analyzing PI that allows for the application of well-known statistical characterization techniques (for example, confidence intervals, p-values, etc.) is needed to connect PI and environmental changes. To address this need we have employed two new analysis techniques: (1) an efficient algorithm for detecting changes in emissive intensities in a PI trace and (2) a new method for analyzing and comparing emissive and non-emissive event distributions.

First, we have employed a new algorithm (Bayesian detection of intensity changes, BDIC) that provides much more efficient detection of change points in the PI traces than the change point detection (CPD) method we previously employed, as illustrated in Figure 1.5.[19,36] A full description of the BDIC method is provided in detail elsewhere.[29,37] Briefly, by assuming the molecule's emission is Poisson distributed, it is preliminarily determined that a change point is probable. This probability is termed the Bayes factor and is defined as the ratio of the probability that there are two emitting states (separated by a time change point) and the probability that there is no change point. For our analysis of NR/PVDF PI traces, a Bayes factor of 10 was used corresponding to 91% confidence that a change point occurred. Once a change point is found to be probable, the location of the change point is calculated using the maximum of the Poisson probability distribution. The time calculated is then confirmed by employing a recursive algorithm to negate any spurious change points. Not only does this BDIC algorithm demonstrate greater accuracy in determining the

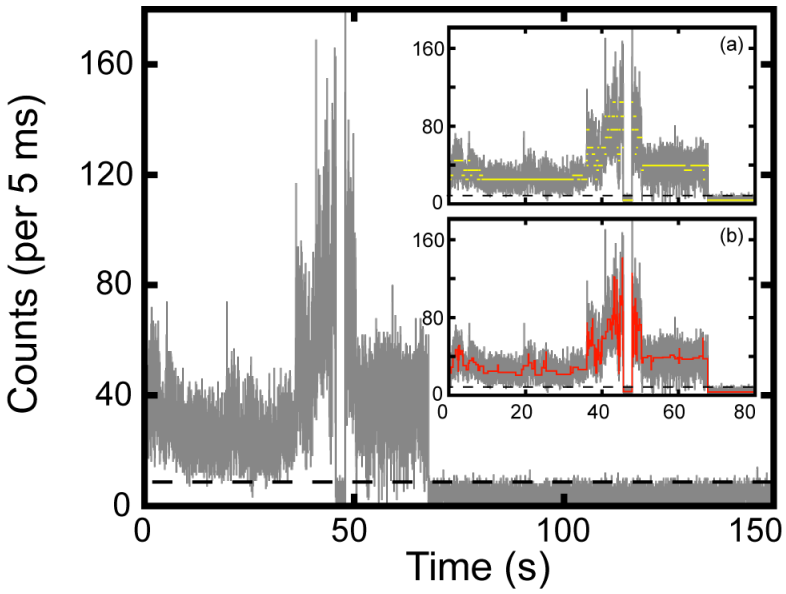

Figure 1.5: Additional PI trace for a single NR molecule in PVDF with the emissive threshold shown as the black dotted line. (a) The first 80 seconds of the trace enlarged with the result of the CPD algorithm overlaid on top (yellow) and (b) the first 80 seconds of the trace enlarged but with the results of the BDIC algorithm overlaid on top (red). Comparison of both insets illustrates the sensitivity of the two algorithms to detect emissive intensity changes.

change points, but this method was also found to be computationally faster, with a PI trace taking days to deconvolve using the CPD algorithm in comparison to the few hours it takes using the BDIC algorithm.

Once the change points are detected and the emissive and non-emissive PI events are determined, the next challenge is to develop statistical methods that allow one to determine when a perturbation to the guest-host system results in a statistically-meaningful change in PI. Previous approaches to this problem involved the creation and analysis of event histograms that were assumed to follow a power-law distribution. When plotted on log-log axes of event duration time versus occurrence, the distributions are modeled using a straight line with the slope of the best-fit line providing a measure of the power-law exponent.[12] In this approach, changes in PI statistics should manifest as a change in the power-law exponent (and thus the slope of the best-fit line). One issue with this analysis is that it assumes that a power-law is the underlying probability distribution function (PDF) describing emissive and non-emissive event duration distributions. For many systems, significant deviations between event distributions and the straight-line fit are observed, calling into question the application of a power-law distribution function. Motivated by these observations, we began to question to what extent power-law exponents can be compared between PI data sets. For example, Figure 1.6 shows a clear deviation from power-law behavior for the PI exhibited by NR/PVDF. Thus the question arose whether the extent to which a power-law PDF represents a given PI data set can be quantified.

A common statistical tool when comparing data sets involves the calculation of p-values (or probabilities) which represent the extent to which a hypothesis exceeds the null hypothesis by some threshold value (for example, 95% probability that the hypothesis is correct).[38] To quantitatively compare PI data sets and to determine the best possible PDF for describing PI data, we explored the idea of using p-values to statistically compare the accuracy of various PDFs to "fit" PI data. To accomplish this, an algorithm for determining the most probable PDF consistent with a given PI

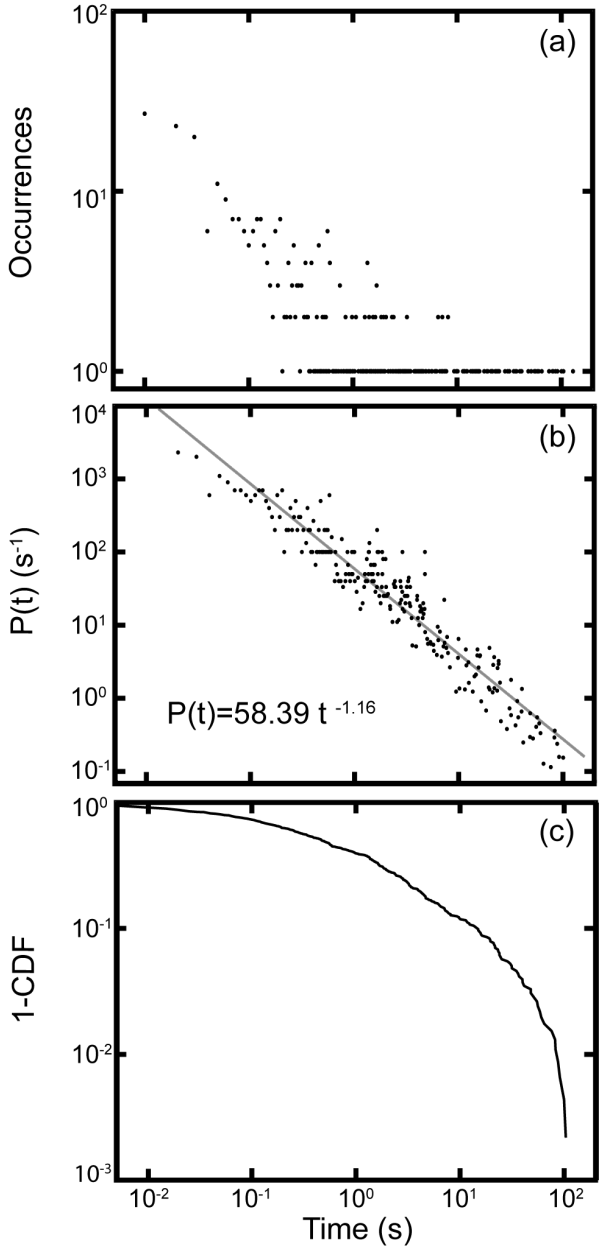

Figure 1.6: Emissive event duration histograms for 100 NR molecules in PVDF with 5.7 $< \varepsilon <$ 28. (a) Raw PI histogram presented on a log-log plot. (b) Continuous probability density for the emissive events calculated from dividing each point in the raw histogram by the average time to the nearest neighbor. Overlaid on the probability density is the linear least squares regression fit to the data corresponding to the power-law distribution shown. (c) The CDF of the data. Comparison of (b) and (c) help illustrate the difference between the commonly used PDF and the CDF. Note that the CDF is already a continuous function negating the need to smooth (and potentially bias) the data.

data set was developed, as was a second method allowing for the quantitative comparison of PI data sets without assuming a PDF. These techniques allow for the determination of whether a change to the PI exhibited by a luminophore occurs following a perturbation without having to first assume an underlying PDF.[31]

The first step in our approach is the use of a cumulative distribution function (CDF), which is simply a sum of event occurrences between two time points (with the initial time point being the shortest time measured). The most notable feature of the CDF is that it is intrinsically a continuous function that does not need additional processing to construct a continuous probability distribution (Figure 1.6). This greatly simplifies PI data analysis and negates any bias that may be introduced when "smoothing" PDFs. CDFs are then compared using the Kolmogorov-Smirnov (KS) test corresponding to calculating a p-value for the best fit of a proposed distribution to the CDF and a comparative test to determine if the two CDFs are drawn from the same distribution.[31] A more detailed explanation of these methods is provided below.

Our new analysis method begins with the application of maximum likelihood estimates (MLE) to initially determine the best-fit parameters of a hypothesized PDF. Then CDFs are calculated for both the raw data and the fit where the CDF is simply defined as the integral of the PDF:

$$\mathrm{CDF}\,(t) = \int_{t_{min}}^{t} \mathrm{PDF}\,(\tau)\,d\tau \tag{1.2}$$

The CDF can also be constructed from the raw data through summation of the histogram:

$$\mathrm{CDF}(t) = \frac{1}{N}\sum_{i=1}^{N} 1 \;\; \{t_i < t\} \tag{1.3}$$

In equation 1.3, t_i is an event duration greater than time t and N is the number of events. This distribution is zero for all t less than the bin-time of the experiment (typically 10 ms in our experiments) and one for all t greater than the longest event. It is important to note that the complimentary CDF (1-CDF(t)) provides a more familiar visualization of the PI data since the probabilities for observing a given emissive or

non-emissive event duration are greatest at short observation times. Next, the KS test is used to compare these CDFs derived from the data and the best fit. The KS statistic, D, is a measure of the absolute maximum difference between two CDFs:

$$D = max_{-\infty<t<\infty}|\mathrm{CDF}_1(t) - \mathrm{CDF}_2(t)| \tag{1.4}$$

Once both the CDFs have been created, the D value can be calculated using the equation above. From here synthetic data sets are calculated (with the same number of entries as the experimental data) from the hypothesized distribution, and MLE methods are again employed to estimate the parameters of the distribution drawn from the synthetic data. The CDF of the synthetic data is then compared to the CDF using the MLE fit and a D value is calculated as before. This process is repeated 10,000 times to create an array of $D_{synthetic}$ statistics. A comparison of all the D values found for the synthetic data versus the empirical data is performed to calculate the p-value:

$$p - \text{value} = \frac{\sum D_{synthetic} \geq D_{real}}{\#\ of synthetic\ sets} \tag{1.5}$$

A p-value determines if a hypothesis should be accepted or rejected. Our hypothesis is that a specific distribution is a good fit to the data, so if the p-value is less than 0.05 we must reject our hypothesis as it is less than 95% likely to be the true distribution describing our data.

One of the first results to emerge from this new analysis was that the emissive and non-emissive event durations observed for NR in PVDF are not well described by a power-law (Figure 1.7). Two additional distributions (lognormal and Weibull) were also investigated, with neither distribution providing p-values greater than 0.05. In short, we have yet to find the distribution that best describes this PI data. However even without having identified the distribution of best fit, we can continue to analyze the impact of ε on PI by simply comparing the CDFs from emissive events in varying ε environments in PVDF. To do this, PI data was collected from single NR molecules embedded in varying ε environments in PVDF.[29] The emission of these NR molecules

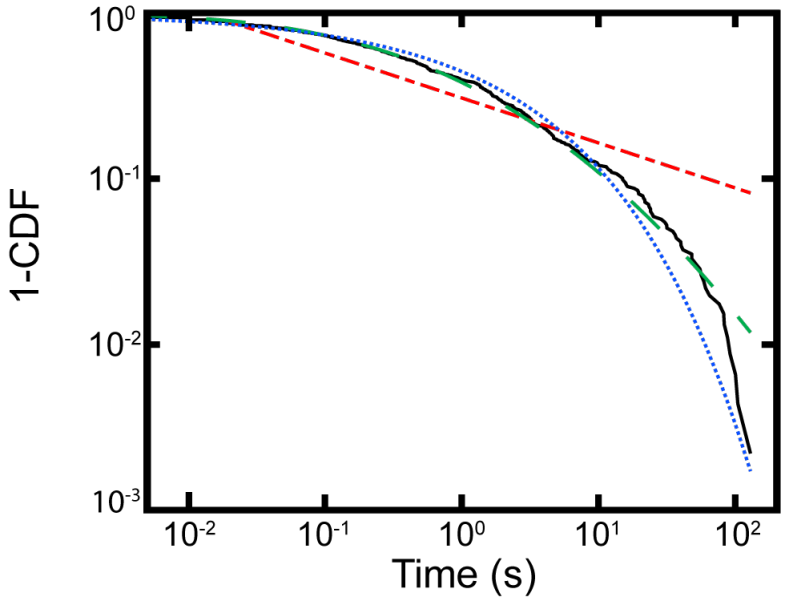

Figure 1.7: Complementary CDFs (black) for the emissive events observed for 100 single molecules of NR embedded in PVDF with $5.7 < \varepsilon < 28$. Best fits to the functions are overlaid: Power-law (red - · -), Lognormal (blue ·) and Weibull (green -). The p-values for all distributions are less than 0.05.

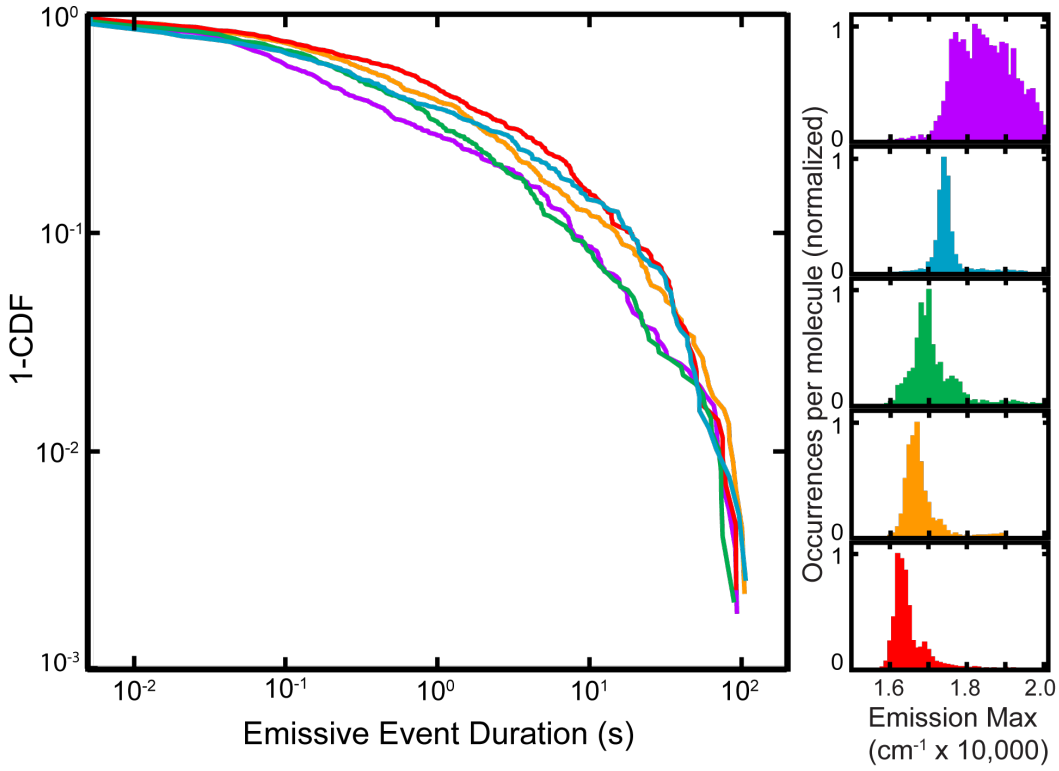

Figure 1.8: Complementary CDFs for the emissive events of single NR molecules in PVDF corresponding to five different dielectric environments: purple ($\varepsilon < 2.8$), blue ($3.2 < \varepsilon < 3.6$), green ($4.2 < \varepsilon < 5.7$), orange ($5.7 < \varepsilon < 28$) and red ($28 < \varepsilon < 58$). Panel on right illustrates the distribution of emission maxima that are contained within each dielectric environment.

was used as described in the quasi-SM method to determine the value of ε giving the following five ε categories: $\varepsilon < 2.8$, $3.2 < \varepsilon < 3.6$, $4.2 < \varepsilon < 5.7$, $5.7 < \varepsilon < 28$, and $28 < \varepsilon < 58$. The emissive event duration CDFs for NR molecules in all five ε environments are shown in Figure 1.8 with the distributions of emission maxima that make up each ε environment. From the CDFs, an increase in the emissive event duration with an increase in the ε is detected. This observation is consistent with a simple comparison involving the median values of the CDFs in Figure 1.8. By comparing the median of each CDF, we observed a rapid increase in emissive event duration as the ε of the environment increased from 2 to 5, then a slower increase with further increase in ε. Thus, through the use of this new analysis method, we were able to directly correlate the PI statistics of a luminophore guest with the local dielectric environment of its host, without altering the chemical composition of either the guest or host or having to assume a parametric form for CDF.

Finally, to connect the observed relation between the PI statistics and ε to the mechanism responsible for PI, the NR/PVDF system was modeled using a photoinduced electron-transfer mechanism between electron donor NR and acceptor PVDF.[29] We employed the semi-classical Marcus expression for the electron transfer rate (k_{et}) where κ_{el} is the electronic coupling energy between the reactant and product states, λ is the reorganization energy, ΔG_{el} is the free energy, k_B is the Boltzmann constant, T is temperature, d_{cc} is the distance between reaction centers of the donor and acceptor, and β describes the fall off of the orbital interaction between the donor and acceptor with distance:[39–41]

$$k_{\mathrm{et}} = \kappa_{\mathrm{el}} \times \frac{1}{\sqrt{4\pi\lambda k_{\mathrm{B}} T}} \times e^{-(\lambda+\Delta G_{\mathrm{el}})^2/4\lambda k_{\mathrm{B}} T} \tag{1.6}$$

$$\kappa_{\mathrm{el}} = \frac{2\pi}{\hbar}|H_{\mathrm{el}}|^2 \tag{1.7}$$

$$H_{\mathrm{el}} = H_{\mathrm{el}}^0 e^{-\beta d_{\mathrm{cc}}} \tag{1.8}$$

By estimating the distance to the nearest trap as the PVDF domain size, which ranges from 10-40 nm[42] and using $\beta = 0.85$ Å^{-1}, we estimate H_{el} to be $\sim 1 \times 10^{-6}$ eV.[39] To

complete this modeling, λ was estimated using:

$$\lambda\,(\mathrm{eV}) = \frac{e^2}{4\pi\epsilon_0}\left\{\frac{1}{\eta^2} - \frac{1}{\varepsilon}\right\}\left\{\frac{1}{2r_\mathrm{D}} + \frac{1}{2r_\mathrm{A}} - \frac{1}{d_\mathrm{cc}}\right\} \tag{1.9}$$

where $r_{D/A}$ are the radii of the donor and accepter species, respectively, η is the index of refraction of the solvent, e is electronic charge, ϵ_0 is the permittivity of free space, and ε is the dielectric constant of the solvent. Finally, ΔG_{el} was estimated:[39]

$$\begin{aligned}\Delta G_\mathrm{el}\,(\mathrm{eV}) = e\left(E^0_{\mathrm{D}^+/\mathrm{D}} - E^0_{\mathrm{trap/trap}^-}\right) - \Delta E_{00} \\ - \frac{e^2}{8\pi\epsilon_0}\left(\frac{1}{r_\mathrm{D}} + \frac{1}{r_\mathrm{A}}\right)\left(\frac{1}{37} - \frac{1}{\varepsilon}\right) - \frac{e^2}{4\pi\epsilon_0\varepsilon d_\mathrm{cc}}\end{aligned} \tag{1.10}$$

$$E^0\left(\mathrm{trap/trap}^-\right) \approx E_\mathrm{trap} - \Delta E\left(1 - \frac{1}{\varepsilon}\right) \tag{1.11}$$

where $E_{D^+/D}{}^0$ = -0.95 V (the oxidation potential of NR in acetonitrile is +0.95 V)[43], $\Delta E(1 - \varepsilon^{-1})$ is equal to the width of the trap distributions over the observed range of ε, measured to be ∼0.3 V, and E_{trap} (the only adjustable parameter) is modeled to be -2.35 eV. Further explanations of each term in the expression above has been published previously.[29]

Employing the half-life as a proxy for the median emissive event duration (half-life = $\log(2)/k_{et}$), we were able to accurately test our hypothesis that the observed trend in emissive event durations arises from a photoinduced electron transfer from NR to PVDF. The results of the model predicted a rapid initial increase in half-life as ε increases from ∼2 to 5, then a slower increase with further increase in ε, a prediction that is entirely consistent with the observed trend in emissive event durations.[29] In summary, we were able to accurately model the ε dependent PI exhibited by NR in PVDF using a photoinduced electron-transfer mechanism. We also note that this approach is not confined to NR/PVDF, but is applicable to a variety of guest-host systems as reported in the literature.[21,31,44]

1.4 Conclusion

This thesis outlines new experimental and analytical methods for investigating the effect of the surrounding environment on the PI exhibited by single luminophores. Using quasi-SM microscopy and new analysis methods the PI exhibited by NR in PVDF has been investigated. The distribution of ε present within films of PVDF was spatially resolved (Chapter 2) and connected to the PI exhibited by NR, and the effect of sample annealing was quantified (Chapter 3). While the new analysis techniques outlined here allow researchers studying SMs to describe the effect of external perturbations on PI in statistically-quantifiable terms (Chapter 4). Finally, by successfully monitoring the PI of NR in the various ε environments of PVDF, it is established that photoinduced electron transfer from NR to PVDF is responsible for the PI exhibited by this system (Chapter 5).

1.5 Acknowledgements

This material is based upon work supported by the National Science Foundation under DMR 1005819 and CHE 1404674.

1.6 Bibliography

[1] Ambrose, W., Basché, T., & Moerner, W. (1991). *The Journal of Chemical Physics* **95**, 7150–7163.

[2] Orrit, M. (2010). *Photochemical & Photobiological Sciences* **9**, 637–642.

[3] Zondervan, R., Kulzer, F., Kol'chenk, M.A., & Orrit, M. (2004). *The Journal of Physical Chemistry A* **108**, 1657–1665.

[4] Hernando, J., Hoogenboom, J., Van Dijk, E., Garcia-Lopez, J., Crego-Calama, M., Reinhoudt, D., Van Hulst, N., & Garcia-Parajo, M. (2004). *Physical Review Letters* **93**, 236404.

[5] Issac, A., Hildner, R., Hippius, C., Würthner, F., & Köhler, J. (2014). *ACS Nano* **8**, 1708–1717.

[6] Eggeling, C., Widengren, J., Rigler, R., & Seidel, C. (1998). *Analytical Chemistry* **70**, 2651–2659.

[7] Deschenes, L.A. & Bout, D.A.V. (2002). *Chemical Physics Letters* **365**, 387–395.

[8] Hoogenboom, J.P., van Dijk, E.M., Hernando, J., van Hulst, N.F., & García-Parajó, M.F. (2005). *Physical Review Letters* **95**, 097401.

[9] Bernard, J., Fleury, L., Talon, H., & Orrit, M. (1993). *The Journal of Chemical Physics* **98**, 850–859.

[10] Zondervan, R., Kulzer, F., Orlinskii, S.B., & Orrit, M. (2003). *The Journal of Physical Chemistry A* **107**, 6770–6776.

[11] Frantsuzov, P., Kuno, M., Janko, B., & Marcus, R.A. (2008). *Nature Physics* **4**, 519–522.

[12] Kuno, M., Fromm, D., Hamann, H., Gallagher, A., & Nesbitt, D. (2000). *The Journal of Chemical Physics* **112**, 3117–3120.

[13] Clifford, J.N., Bell, T.D., Tinnefeld, P., Heilemann, M., Melnikov, S.M., Hotta, J., Sliwa, M., Dedecker, P., Sauer, M., Hofkens, J., & Yeow, E.K.L. (2007). *The Journal of Physical Chemistry B* **111**, 6987–6991.

[14] Riley, E.A., Bingham, C., Bott, E.D., Kahr, B., & Reid, P.J. (2011). *Physical Chemistry Chemical Physics* **13**, 1879–1887.

[15] Schuster, J., Cichos, F., & von Borczyskowski, C. (2005). *Applied Physics Letters* **87**, 051915.

[16] Issac, A., von Borczyskowski, C., & Cichos, F. (2005). *Physical Review B* **71**, 161302.

[17] Kobayashi, H., Onda, S., Furumaki, S., Habuchi, S., & Vacha, M. (2012). *Chemical Physics Letters* **528**, 1–6.

[18] Osad'ko, I. & Fedyanin, V. (2011). *Physical Review A* **83**, 063841.

[19] Wustholz, K.L., Bott, E.D., Kahr, B., & Reid, P.J. (2008). *The Journal of Physical Chemistry C* **112**, 7877–7885.

[20] Ai, N., Walden-Newman, W., Song, Q., Kalliakos, S., & Strauf, S. (2011). *ACS Nano* **5**, 2664–2670.

[21] Riley, E.A., Hess, C.M., Pioquinto, J.R.L., Kaminsky, W., Kahr, B., & Reid, P.J. (2012). *The Journal of Physical Chemistry B* **117**, 4313–4324.

[22] Sluss, D., Bingham, C., Burr, M., Bott, E.D., Riley, E.A., & Reid, P.J. (2009). *Journal of Materials Chemistry* **19**, 7561–7566.

[23] Lovinger, A.J. (1982). In *Developments in Crystalline Polymers–1*, pp. 195–273. Springer.

[24] Greenspan, P. & Fowler, S.D. (1985). *Journal of Lipid Research* **26**, 781–789.

[25] Levitsky, I., Krivoshlykov, S.G., & Grate, J.W. (2001). *Analytical Chemistry* **73**, 3441–3448.

[26] Hou, Y., Bardo, A.M., Martinez, C., & Higgins, D.A. (2000). *The Journal of Physical Chemistry B* **104**, 212–219.

[27] Rei, A., Ferreira, M.I.C., & Hungerford, G. (2008). *Journal of Fluorescence* **18**, 1083–1091.

[28] Hess, C.M., Riley, E.A., Palos-Chávez, J., & Reid, P.J. (2013). *The Journal of Physical Chemistry B* **117**, 7106–7112.

[29] Hess, C.M., Riley, E.A., & Reid, P.J. (2014). *The Journal of Physical Chemistry B* **118**, 8905–8913.

[30] Hess, C.M., Rudolph, A.R., & Reid, P.J. (2015). *The Journal of Physical Chemistry B*, 10.1021/jp512486n.

[31] Riley, E., Hess, C., Whitham, P., & Reid, P. (2012). *The Journal of Chemical Physics* **136**, 184508.

[32] Serghei, A., Tress, M., & Kremer, F. (2006). *Macromolecules* **39**, 9385–9387.

[33] Fumagalli, L., Ferrari, G., Sampietro, M., & Gomila, G. (2009). *Nano Letters* **9**, 1604–1608.

[34] Crider, P., Majewski, M., Zhang, J., Oukris, H., & Israeloff, N. (2007). *Applied Physics Letters* **91**, 013102–013102.

[35] Riedel, C., Arinero, R., Tordjeman, P., Lévêque, G., Schwartz, G.A., Alegría, A., & Colmenero, J. (2010). *Physical Review E* **81**, 010801.

[36] Watkins, L.P. & Yang, H. (2005). *The Journal of Physical Chemistry B* **109**, 617–628.

[37] Ensign, D.L. & Pande, V.S. (2009). *The Journal of Physical Chemistry B* **114**, 280–292.

[38] Clauset, A., Shalizi, C.R., & Newman, M.E. (2009). *SIAM Review* **51**, 661–703.

[39] Kavarnos, G.J. (1993). *Fundamentals of Photoinduced Electron Transfer*, Volume 1. VCH Publishers New York.

[40] Marcus, R. (1990). *Journal of Physical Chemistry* **94**, 4963–4966.

[41] Marcus, R. (1984). *The Journal of Chemical Physics* **81**, 4494–4500.

[42] Guan, F., Wang, J., Pan, J., Wang, Q., & Zhu, L. (2010). *Macromolecules* **43**, 6739–6748.

[43] Miyata, S. (1997). *Organic Electroluminescent Materials and Devices*. CRC press.

[44] Riley, E.A., Hess, C.M., & Reid, P.J. (2012). *International Journal of Molecular Sciences* **13**, 12487–12518.

Chapter 2

MEASURING THE SPATIAL DISTRIBUTION OF DIELECTRIC CONSTANTS IN POLYMERS THROUGH QUASI-SINGLE MOLECULE MICROSCOPY

Chelsea M. Hess, Erin A. Riley, Jorge Palos-Chávez, and Philip J. Reid

Department of Chemistry, University of Washington, Box 351700, Seattle, WA 98195, United States

2.1 Abstract

The variation in dielectric constant is measured for thin films of poly(methyl methacrylate) (PMMA) and poly(vinylidene fluoride) (PVDF) using confocal fluorescence microscopy. Spatial variation in the local dielectric constant of the polymer films on the ∼250 nm length scale is measured using the solvochromatic emission from incorporated nile red (NR) at "quasi-single molecule" (10^{-7} M) and true-single molecule (SM) concentrations (10^{-9} M). Correlation of the NR fluorescence wavelength maximum with dielectric constant is used to transform images of NR's emission maxima to spatial variation in local dielectric constant. We demonstrate that the distributions of dielectric environments measured in the quasi- and true-SM approaches are equivalent; however, the enhanced signal rates present in the quasi-SM approach results in this technique being more efficient. In addition, the quasi-SM technique reports directly on the continuous spatial variation in dielectric constant, information that is difficult to obtain in true-SM studies. With regards to the polymers of interest, the results presented here demonstrate that a limited distribution of dielectric environments is present in PMMA; however, a broad distribution of environments exists in PVDF consistent with this polymer existing as a distribution of structural phases.

2.2 Introduction

Measuring the distribution of dielectric environments at the nanoscale is an emerging area of interest.[1–3] Largely motivated by the development of new materials such as nano-patterned dielectrics, knowledge of the spatial distribution of dielectric constants (ε) is requisite in describing the properties of these materials. Our group is particularly interested in the dielectric properties of polymers used in electro-optical (EO) devices. Recent studies demonstrated a two-fold increase in the hyperpolarizability of EO chromophores with an increase in ε from 2 to 36.[4] Given the dependence of EO activity on ε, knowledge of the distribution of ε within the polymer host is fundamental for predicting the EO activity of guest chromophores and overall material performance.

Measurements of ε for polymer films as thin as 5 nm can be performed using broad-band dielectric spectroscopy; however, this technique has limited spatial resolution.[5] Recently, measurements of ε on nanometer length scales have been performed using nanoscale dielectric microscopy.[1] This technique employs a nanoscale capacitance microscope (NCM) corresponding to a modified atomic force microscope (AFM) equipped with a low frequency alternating current detection system. The NCM acquires two scans of the sample: one scan measuring film thickness and the other measuring ε through a sub-attofarad capacitance detector. A significant limitation of this technique is that film thickness must be < 20 nm. Another promising technique for measuring the dielectric properties of polymers is frequency modulation electrostatic force microscopy (fm-EFM).[3,6] Though this method does not directly measure ε, it does provide a measure of the dielectric response with $\sim$40-nm spatial resolution. Finally, it should be noted that both NCM and fm-EFM are surface measurement techniques.

Approaches for measuring distributions of ε in polymers generally employ solvatochromic dyes serving as nanoreporters of the local environment. Nile red (NR) has

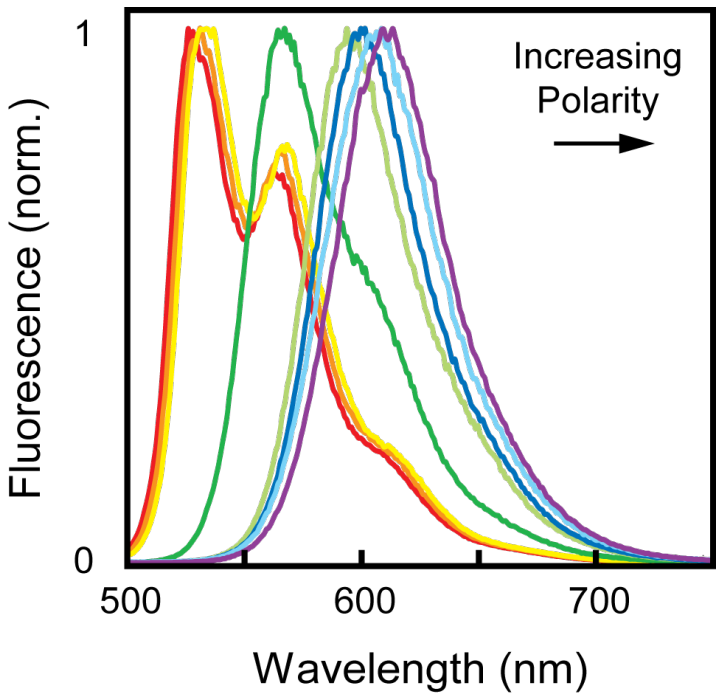

Figure 2.1: Fluorescence spectra of NR in hexane (red), heptane (orange), cyclohexane (yellow), toluene (dark green), chloroform (light green), dichloromethane (dark blue), acetone (light blue), and acetonitrile (dark purple) obtained with a 488-nm excitation.

been widely used for this purpose, with the solvatochromic properties of this dye illustrated in Figure 2.1. The emission from NR exhibits a ∼100 nm bathochromic shift with a change in ε from ∼2 to ∼32.[7–10] The figure demonstrates that changes in the NR emission line shape are also observed between non-polar (cyclohexane, heptane and hexane) and polar solvents. These changes have been attributed to specific solvent interactions such as dipole-dipole which increase the homogeneous line width.[7,11] NR has previously been used to measure the evolution in ε for poly(vinylidene fluoride) (PVDF) films accompanying the transition from disordered α-phase to ferroelectric β-phase upon stretching.[12] NR has also been used in single molecule (SM) studies of dielectric heterogeneity in poly(methyl methacrylate) (PMMA) and poly(vinyl alcohol).[9] Although informative, SM studies involve the measurement of many individual molecules to achieve a statistically-significant measure of the distribution of ε such that this approach can be time consuming. In addition, information regarding the spatial variation in ε is extremely difficult to obtain using SM approaches.

We report here a quasi-SM method for measuring the spatial variation of ε in polymer films. Specifically, confocal fluorescence microscopy is used to measure the distribution of ε in PMMA and PVDF films. PMMA is a widely studied polymer[13] with a modest dielectric constant ($\varepsilon \approx 3$).[14] In comparison, PVDF has a range of $\varepsilon \approx 6$ to 13 for α- and β-phase films, respectively,[14] and its dielectric, ferroelectric, piezoelectric, and pyroelectric properties have been exploited in innumerable technical applications such as optical devices, sensors, biomedical materials, and fuel cells.[15] The variation in ε for these polymers is determined by measuring solvatochromic shifts of NR emission which directly report on the local ε of the surroundings. This approach has been employed at the SM level by others;[9] however, in these previous studies the chromophores were separated by distances of microns such that measurement of the spatial variation in ε was not possible. In this study, NR concentrations roughly 100-fold higher than those used in earlier SM studies are employed such that spatial variations in ε are readily observed. Convergence of this "quasi-SM" approach

with the distributions of ε measured in true-SM studies is demonstrated. For PMMA a Gaussian distribution of ε is observed, with the mean of this distribution consistent with literature values. In PVDF three distinct optically excited populations are observed corresponding to separate dielectric environments within the polymer. In addition, the distribution of ε measured in PVDF spans an order of magnitude. Spatially resolved ($\sim$250 nm) images of ε in PMMA and PVDF obtained in the quasi-SM studies are also presented, with PMMA demonstrating fewer environments with smoother boundaries in comparison to PVDF which demonstrates spatial variation in ε. In summary, the results presented here demonstrate that quasi-SM confocal microscopy provides a simple and direct way to measure distributions of ε in polymer films with nanometer lateral resolution.

2.3 Experimental

2.3.1 Sample Preparation

PMMA Films

Nile red (NR, Aldrich, powder, 99+% pure by LC-MS) was used as received. A 3.5×10^{-5} M NR solution and a 10 wt.% poly(methyl methacrylate) (PMMA, Sigma Aldrich, MW $\approx$ 15,000 by GPC) solution in toluene (Fisher Scientific, HPLC grade) were prepared. Aliquots of the NR stock solution were then added to the polymer solution to produce final NR concentrations of 10^{-7} M and 10^{-9} M in 10 wt.% PMMA/toluene corresponding to quasi-single molecule and true-single molecule samples, respectively. Glass coverslips were cleaned by boiling in a solution of 3:2:1 nanopure water (Barnstead, NANOpure II): ammonium hydroxide: hydrogen peroxide for 2 hours, cooled, rinsed with nanopure water, and rapidly dried with nitrogen gas. PMMA films were prepared by spin coating coverslips at 3000 rpm for 60 seconds. The samples were then dried under vacuum for 30 minutes. Film thicknesses of 390 $\pm$ 10 nm were determined by ellipsometry (J.A Woollam Co., Inc., M-2000).

PVDF Films

A 3.1×10^{-5} M NR and a 5 wt.% poly(vinylidene fluoride) (PVDF, Sigma Aldrich, MW $\approx$ 534,000 by GPC) solution were prepared in dimethyl sulfoxide (DMSO, EMD Chemicals Inc., ACS grade). PVDF films were prepared as the PMMA films described above except that to maximize the amount of β-phase present in the PVDF films the NR in 5 wt.% PVDF/DMSO solutions were heated to 90 °C then spun onto clean glass coverslips at room temperature for 60 seconds at 1000 rpm. The films were then dried at room temperature for one hour and in a 60 °C oven for 15 minutes. The resulting films thicknesses were 290 ± 10 nm as measured by ellipsometry. Films were confirmed to be in the β-phase through X-ray diffraction (Bruker AXS, D8 Discover w/ GADDS) with a diffraction peak at $2\theta = 20.8°$ confirming that maximum percentage (60%) of PVDF exists in the β-phase in agreement with the literature.[16]

Ensemble Spectroscopy

Fluorescence spectra of NR in solutions and in polymer films were acquired using 488-nm excitation (Horiba Fluorolog 3) for both polymers, and also with 579-nm excitation for PVDF. UV-vis absorption spectra of the samples were also measured (Varian Cary Eclipse 5000). Heavily dyed films of NR in PMMA and PVDF were prepared by drop casting a $\sim 10^{-5}$ M NR sample at room temperature resulting in faintly colored films. Solution phase fluorescence spectra of $\sim 10^{-6}$ M solutions of NR dissolved in hexane (Sigma Aldrich, >95%), heptane (Fisher Scientific, HPLC grade), cyclohexane (EMD, OmniSolv), toluene, chloroform (Fisher Scientific, HPLC grade), dichloromethane (EMD, HPLC grade), acetone (Sigma Aldrich, HPLC grade), and acetonitrile (EMD, HPLC grade) were collected.

Confocal Microscopy

Confocal microscopy studies were performed by placing the sample on a piezoelectric nanopositioning stage (Queensgate, NPS-XY-100B). Excitation at 488-nm (Novalux, Protera) with a power of 3 μW as measured at the entrance port of the microscope was employed. The polarization of the 488-nm excitation field was defined using a 488-nm polarizing beam splitter and converted to circular polarization using a 488-nm λ/4 waveplate. The excitation field was directed into a 1.3 NA objective (Nikon, Plan-Fluor) using a 488-nm dichroic long-pass filter. Emission was collected in an epi-geometry, the excitation field rejected using a 500-nm long-pass filter (Chroma, HQ500LP), and the emission was focused onto a pinhole (CVI, 75-μm diameter) to provide confocal resolution. The emission was split by a 600-nm short-pass dichroic mirror, with the reflected and transmitted intensity focused onto two separate avalanche photodiode detectors (Perkin-Elmer SPCM-AQR-16). Ten 10 μm × 10 μm fluorescence intensity images were collected employing a step size of 0.1 μm and an integration time of 0.2 s per step. In the single molecule studies ∼10 individual molecules were detected per scan resulting in a total of ∼100 molecules for the total SM data set.

All data processing was performed in MATLAB (version R2012b). Single NR mole-cules were identified using an emissive threshold defined as the average of the brightest pixel recorded by each detector in three scans of dye free polymer films (500 and 1000 counts, for PMMA and PVDF, respectively). Images were processed by first assigning pixel values less than or equal to the threshold a null value (NaN), and the ratio of the reflected and transmitted intensities (R/T) were determined for each pixel. The remaining real-valued pixels were compiled into an array containing the data from all 10 scans, with each pixel corresponding to an element in this array. This process was repeated for the 10^{-7} M films, but without employing an emissive threshold. A mapping of the R/T ratio to emission wavelength maxima was performed by

convolving ensemble NR emission spectra in hexane, toluene and acetonitrile with the APD efficiency curves, the emission filter transmission curve, and the 600-nm dichroic reflectance and transmission curves to calculate the expected reflected (R) and transmitted (T) spectra as described previously.[17] A mapping of the R/T ratio to NR emission maximum was performed by numerically shifting the NR emission spectrum in the solvents listed above and calculating R/T. The curves that resulted were then combined to produce a "hybrid" curve that continually transforms the R/T ratio to wavelength. This incorporates the change in fluorescence line shape as the polarity of the solvent increases (see the Supporting Information). The calculated relationship between R/T and emission maximum was experimentally verified by measuring R/T values from within droplets of NR solutions on the microscope employing each solvent identified above.

2.4 Results and Discussion

The studies outlined here employ NR emission solvatochromism to determine the distribution of ε in PMMA and PVDF. At room temperature PMMA exists in a single phase and is thus expected to demonstrate a single distribution of ε with variation between local environments providing width to this distribution. Literature values for ensemble measurements of ε in PMMA are 3.0 ± 0.6.[9,14] In contrast, PVDF exists as a mixture of two dominant phases (α and β), each of which can be preferentially expressed through processing conditions. The α-phase is monoclinic and has a trans-gauche-trans-gauche (TGTG) chain conformation. The β-phase of PVDF exhibits ferroelectric behavior useful in piezoelectric and pyroelectric applications. This phase is orthorhombic with an all-trans chain conformation.[18] PVDF in the α-phase exhibits a dielectric constant of $\varepsilon = 6$, increasing to 13 with an increase in the amount of β-phase.[12] In our studies, processing conditions described above were chosen to maximize the percentage of β-phase in order to produce a broad range of dielectric constants.

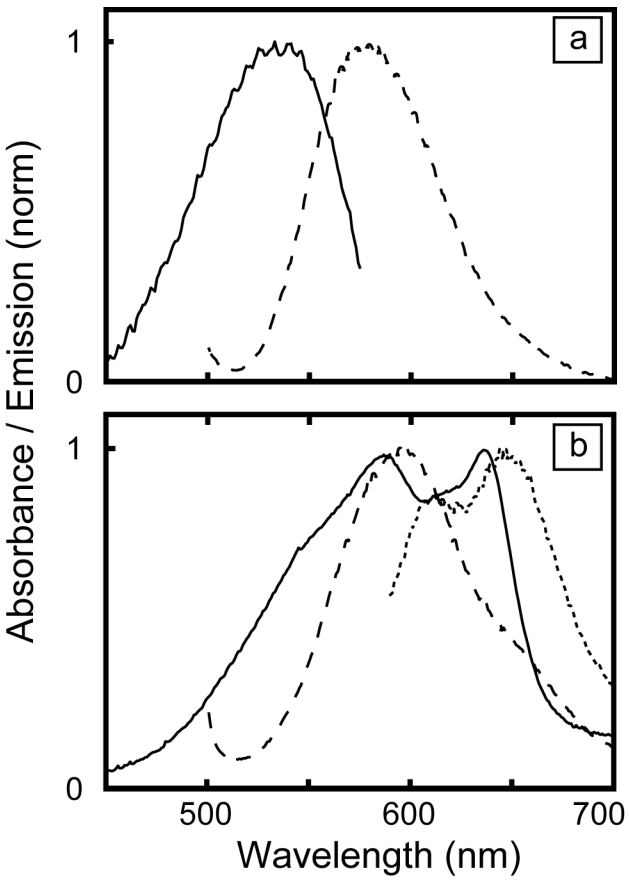

Figure 2.2: Absorbance (solid) and emission (dashed) spectra for (a) NR in PMMA with 488-nm excitation. Band maxima occur at $\lambda_{abs} = 533$ nm and $\lambda_{fluor} = 579$ nm. (b) NR in PVDF with a 488-nm excitation (large dash) and 579-nm excitation (small dash). Band maxima occur at $\lambda_{abs} = 550$ nm, 587 nm and 636 nm while $\lambda_{fluor} = 600$ nm and 650 nm for NR in PVDF.

Ensemble absorption and emission spectra of NR in PVDF and PMMA films are presented in Figure 2.2. For NR in PMMA a Stokes shift of ∼40 nm is observed with absorption and emission demonstrating similar line shapes. In contrast, for NR in PVDF the line shapes for absorption and emission are significantly different. Computational studies of NR assign the absorption of NR to an electronic transition between a single ground (S_0) and locally excited (LE) state; therefore, the multiple peaks evident in the absorbance spectrum of NR in PVDF suggest that there are subpopulations of NR in different dielectric environments.[11] With regards to the emission spectrum, previous observations of "dual-emission" or multiple emission peaks for NR have been attributed to emission from both locally-excited (LE) and twisted intramolecular charge transfer (TICT) states.[9,19–21] The TICT excited state is formed via intramolecular charge transfer from the LE state through rotation of the amine group. Population of the TICT excited state occurs in polar, protic solvents where hydrogen bonds stabilize the TICT excited state, and the energy of the TICT state is lower relative to the LE state. The fluorescence quantum yield for NR in alcohols is diminished relative to non-polar solvents, and the shift in emission maximum follows a different relationship with dielectric constant than is seen with polar aprotic solvents.[10] Since PVDF is polar and aprotic, we expect the NR emission to be dominated by LE state emission such that Figure 2.2 is interpreted as reflecting NR emission from different dielectric environments. Previous evidence for NR existing in different dielectric environments was found in studies of NR dual emission in polystyrene films.[21] To test the dielectric-subpopulation hypothesis, the excitation wavelength was changed from 488-nm to 579-nm which resulted in enhanced emission at longer wavelengths (Figure 2.2) consistent with the emission arising from sub-populations of NR in different dielectric environments.

In quasi-SM studies, 10^{-7} M NR concentrations were used to measure the dielectric heterogeneity of the polymer films. This concentration is roughly 100 times greater than that used in true-SM studies, corresponding to a luminophore number density

$\sim$10 molecules/μm^2. When compared to the spatial resolution of the microscope ($\sim$0.250 μm) this concentration should result (on average) in two molecules being present in the illuminated volume. Figure 2.3 presents a 10 $\times$ 10 μm image of the NR emission maxima in PMMA and PVDF films obtained by measuring the reflected and transmitted emission intensities from a 600-nm dichroic mirror. Differences between reflected and transmitted intensity provides a measure of the NR emission maximum as a function of position. Spatial variation in the NR emission maximum is evident in both films corresponding to a spatial variation in ε in the polymer films. Comparison of the two images reveals that PVDF demonstrates a greater variation in ε relative to PMMA. This difference is further evidenced by the plot of emission wavelength versus distance for a line profile across the images as shown in Figures 2.3(c) and (d). The PVDF film exhibits domains of different emission wavelengths including the "blue" and "red" emitting domains (550 nm and 650 nm respectively) in addition to the dominant domain corresponding to the "green" (600 nm) domains. This result suggests that PVDF films are characterized by multiple dielectric environments supporting the interpretation of the ensemble absorbance and emission spectra presented earlier. The images shown in Figure 2.3 provide a direct measure of the degree of spatial variation in ε for the polymer films. For example, the line scan provided in Figure 2.3(d) reveals a region of red-shifted NR emission in PVDF centered at $\sim$2 μm with a full width at half maximum of $\sim$1 μm. The direct measurement of spatial variation in ε is a unique capability of this technique, with lower concentration studies lacking the NR number density to compare neighboring regions in the films.

Convergence of quasi and true-SM measured ε distributions is demonstrated in Figure 2.4. The figure presents histograms of emission maxima for the 10^{-7} M (quasi) and 10^{-9} M (true-SM) NR films. Both techniques demonstrate that the distribution of emission maxima is narrower for PMMA in comparison to PVDF, consistent with a greater distribution of ε in PVDF. Distributions of emission maxima obtained in the SM studies (bottom panels of Figure 2.4) are in very good agreement with the

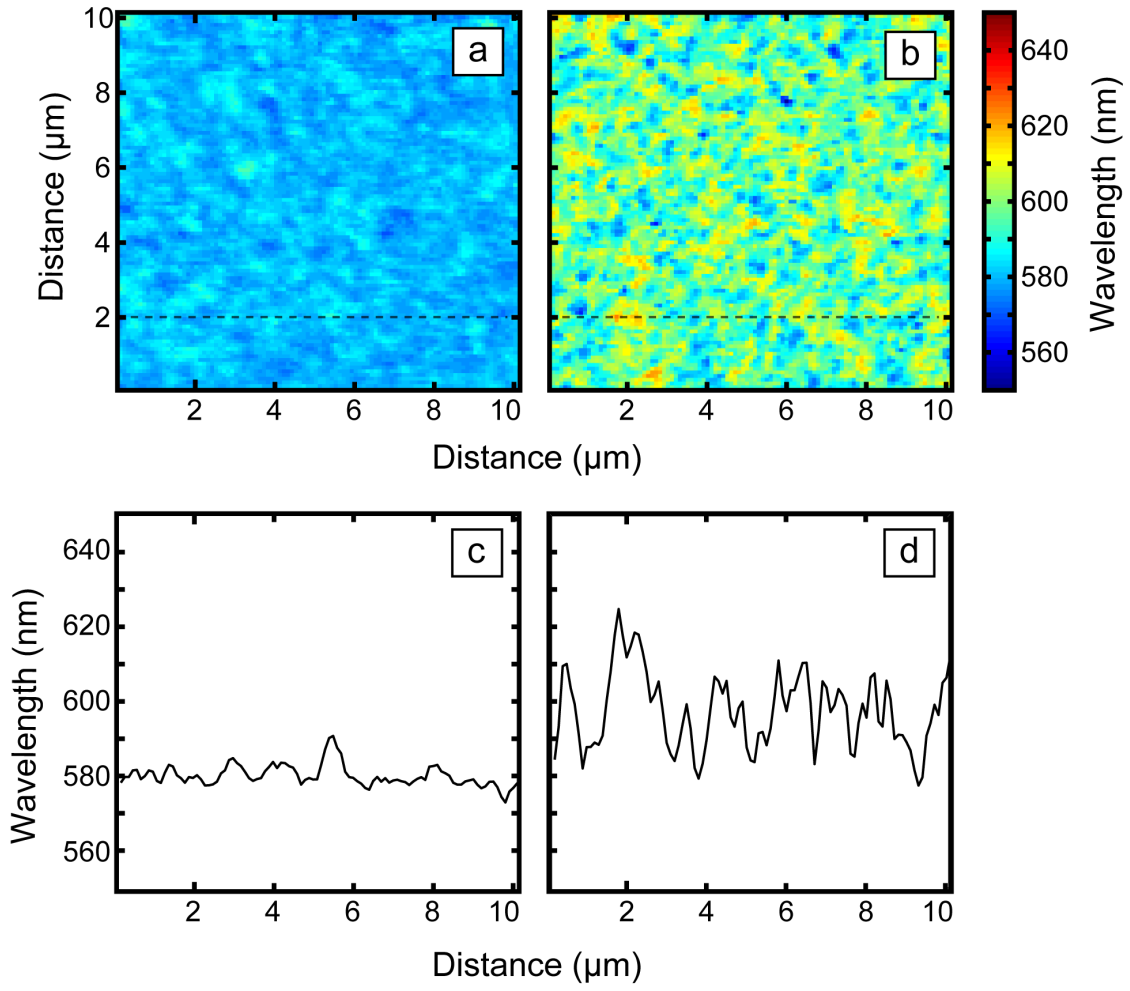

Figure 2.3: 10 × 10 μm images of 10^{-7} M NR in ∼400 nm and ∼300 nm thick films of (a) PMMA and (b) PVDF, respectively. Images correspond to the variation in NR emission maximum versus position in the film. Data was collected by separating the emission using a 600-nm short pass mirror and detecting the reflected and transmitted intensity using separate APDs. The ratio of the intensities for a specific location are calculated and transformed into wavelength as described in the text. Dashed line in (a) corresponds to the line plot shown in (c) demonstrating the relatively modest spatial variation in ε in PMMA. In contrast the dashed line in (b) corresponds to the line plot shown in (d) where substantial spatial variation in ε is observed in PVDF.

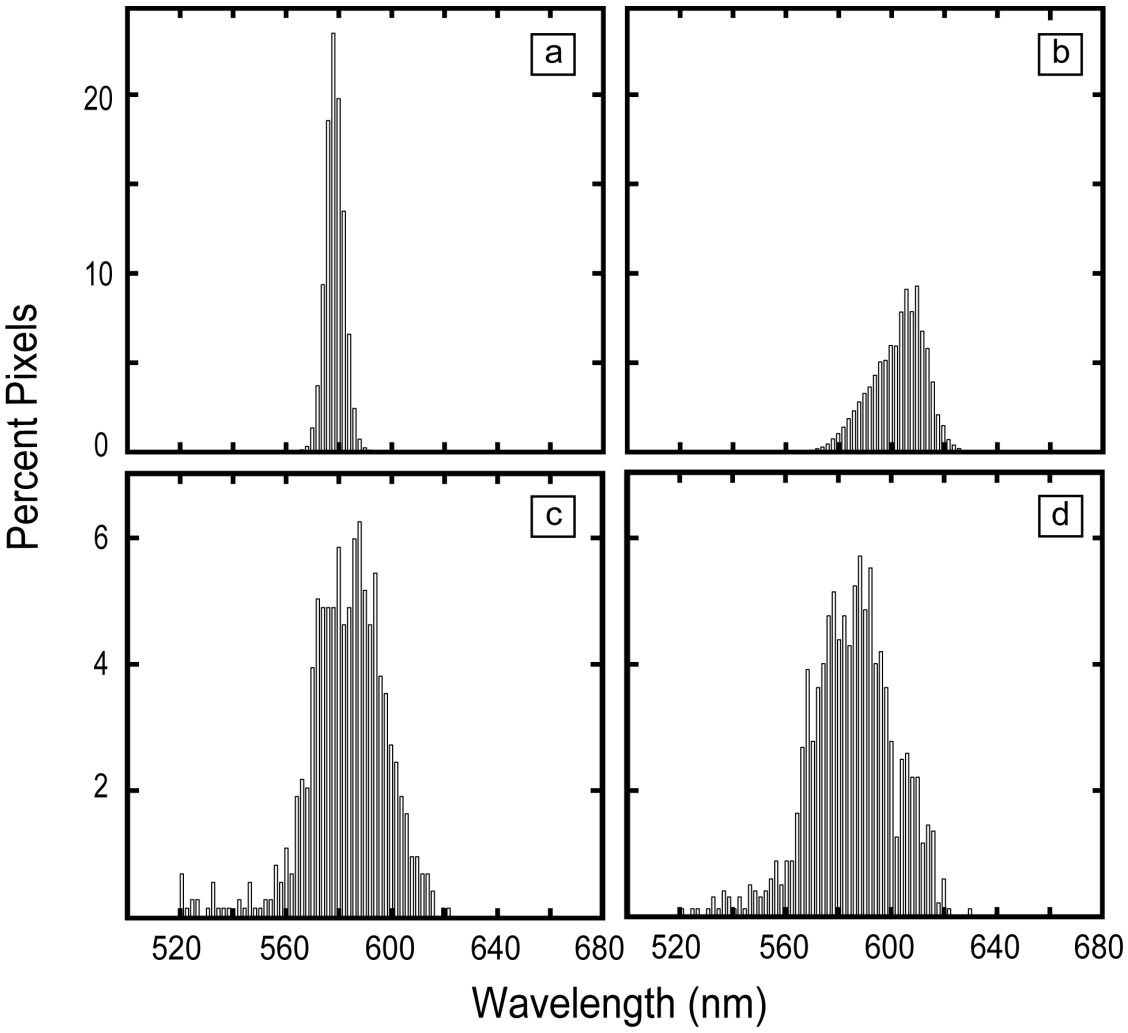

Figure 2.4: NR emission wavelength histograms obtained in quasi-SM (10^{-7} M) and true-SM (10^{-9} M) studies. (a) 10^{-7} M NR in PMMA, (b) 10^{-7} M NR in PVDF, (c) 10^{-9} M NR in PMMA, and (d) 10^{-9} M NR in PVDF. All histograms were compiled from 10 scans each which allowed for the inclusion of ∼100 molecule's data into the single molecule histograms.

quasi-SM results, with differences reflecting the limited emission statistics available in the SM studies. In terms of distribution averages, the single molecule data have an average emission wavelength in PMMA of $\lambda_{average}$=583 nm (quasi λ_{max}= 580 nm) and 586 nm in PVDF (quasi λ_{max}= 603 nm).

The quasi-SM technique relies on correlation between the NR emission maxima and ε. This correlation has been previously quantified using the spectral shift in NR emission in condensed environments relative to the vapor phase:[12]

$$\Delta E_F = E_F - E_F^0 = c_1 \frac{n_2 - 1}{2n_2 + 1} + c_2 \left(\frac{\varepsilon - 1}{\varepsilon + 2} - \frac{n^2 - 1}{n^2 + 2} \right) \tag{2.1}$$

In the above expression E_F is the measured NR emission maximum in eV, $E_F{}^0$ is the vapor phase emission maximum, n is the index of refraction, ε is the dielectric constant, c_1 = -1.128 eV and c_2 = -0.556 eV are empirical constants. Though the equation above is in qualitative agreement with the solvatochromic shifts exhibited by NR (Figure 2.1), the model does not accurately capture the relationship between ε and emission maximum at values of ε less than 5 and greater than 10. The connection between NR's solvatochromism and ε was central to the previous work of Higgins and co-workers[9]. In this previous work the NR emission energy is given by $\bar{\nu}_{fl}$ = ΔG° - λ_0 - λ_i, where λ_0 is the solvent reorganization energy and λ_i is the internal molecular reorganization energy of the solute. The solvent reorganization energy was modeled as a dielectric continuum such that:

$$\lambda_0 = \frac{(\Delta\mu)^2}{hca^3} \left[\frac{\varepsilon - 1}{2\varepsilon + 1} - \frac{\eta^2 - 1}{2\eta^2 + 1} \right] \tag{2.2}$$

In the above expression ε is the static dielectric constant, η^2 is the optical dielectric constant (index of refraction), a is the radius of the spherical cavity in which the solute resides, h is Planck's constant, c is the speed of light, and $\Delta\mu$ is the change in dipole

moment between the ground and excited states. Next, λ_0 can be separated into static and dynamic components, denoted as λ_{00} and λ_{0i}, respectively. In this approach, λ_{0i} represents the contribution to the reorganization energy from solvent relaxation during excited state lifetime (i.e. vibrational relaxation), denoted as a dynamic dielectric constant, $\varepsilon_{\mathrm{dyn}}$ and in general $\varepsilon > \varepsilon_{\mathrm{dyn}}$ due to $\varepsilon_{\mathrm{dyn}}$ corresponding solvent dynamics on the ~2 ns timescale. Using the following substitution $f(D) = \frac{D-1}{2D+1}$, the solvent reorganization energy becomes:[22]

$$\lambda_0 = \lambda_{0i} + \lambda_{00} \tag{2.3}$$

$$\lambda_{00} = \frac{(\Delta\mu)^2}{hca^3}\left(f(\varepsilon) - f(\varepsilon_{dyn})\right) \tag{2.4}$$

$$\lambda_{0i} = \frac{(\Delta\mu)^2}{hca^3}\left(f(\varepsilon_{dyn}) - f(\eta^2)\right) \tag{2.5}$$

Finally, Higgins identifies the part of ΔG° that gives rise to emission energy shifts relative to the vapor phase as $\Delta\Delta G$:

$$\Delta G^\circ = \Delta G_\nu - \Delta\Delta G \tag{2.6}$$

and

$$\Delta\Delta G = \frac{\Delta(\mu^2)}{hca^3}\left[\frac{\varepsilon - 1}{2\varepsilon + 1}\right] \tag{2.7}$$

In the above expression $\Delta(\mu^2) = (\mu_e{}^2 - \mu_g{}^2)$ with subscripts e and g denoting the excited and ground state permanent dipole moments, respectively. The above expressions allow one to estimate the contributions from λ_{0i} and $\Delta\Delta G$ to the solvatochromic shift in NR emission. Using reasonable parameters for NR[9,23] in PMMA (μ_g of 11 D,

$\Delta\mu$ of 5 D, a = 5 Å, η = 1.4), we find that for ε and ε_{dyn} = 2, $\lambda_{0i} \sim 10$ cm^{-1} and $\Delta\Delta G \sim 1000$ cm^{-1}; and for ε and ε_{dyn} = 5, $\lambda_{0i} \sim 150$ cm^{-1} and $\Delta\Delta G \sim 2000$ cm^{-1}. In short, these estimates demonstrate that the solvatochromic shift exhibited by NR is dominated by $\Delta\Delta G$, and this quantity is directly related to ε.

The empirical relationship between NR emission max and ε was established by measuring the NR emission energies in various solvents of known ε as shown in Figure 2.5. For completeness, the variation in NR emission maximum with solvent E_T30 value is also shown.[24] The figure demonstrates that small variations in dielectric constant result in large shifts in emission energy when $\varepsilon < 5$, but only modest shifts in emission are observed when $\varepsilon > 10$. The solvochromatic shift of NR with ε was best fit by a sum of two exponentials: $E_F(\varepsilon) = Ae^{-B\varepsilon} + Ce^{-D\varepsilon}$, with best fit corresponding to A = $(1.076 \pm 1.179) \times 10^4$, B = 0.8 ± 0.6, C = $(1.67 \pm 0.05) \times 10^4$ and D = 0.0005 ± 0.001. Using this equation, the maximum of emission wavelength distributions for PMMA and PVDF from Figures 2.4(a) and (b) (580 nm and 603 nm respectively) correspond to ε = 3.64 for PMMA and ε = 10.72 for PVDF, in good agreement with ensemble measurements.[14] This conversion is further illustrated through of the transformation of the spatially mapped emission wavelength maximum to ε for the scans in Figure 2.3 as shown in Figure 2.6. The best-fit used to transform the distribution of E_F to distributions of ε is also shown in Figure 2.7. The quasi-SM PMMA film demonstrates a Gaussian distribution of dielectric constants with a maximum at ε = 3.64 and standard deviation of 0.21. The corresponding histogram for PVDF is a heavy tailed distribution with values of ε spanning an order of magnitude. A component of the distribution tailing towards higher ε arises from the modest change in NR emission when $\varepsilon > 10$ noted earlier. However, this tailing is not due exclusively to this effect as the observation of high-ε domains in PVDF is not unreasonable. Specifically, the ensemble emission spectra demonstrate a shoulder at 650 nm (1.54×10^4 cm^{-1}) consistent with $\varepsilon > 40$ demonstrating that high-dielectric environments are present.

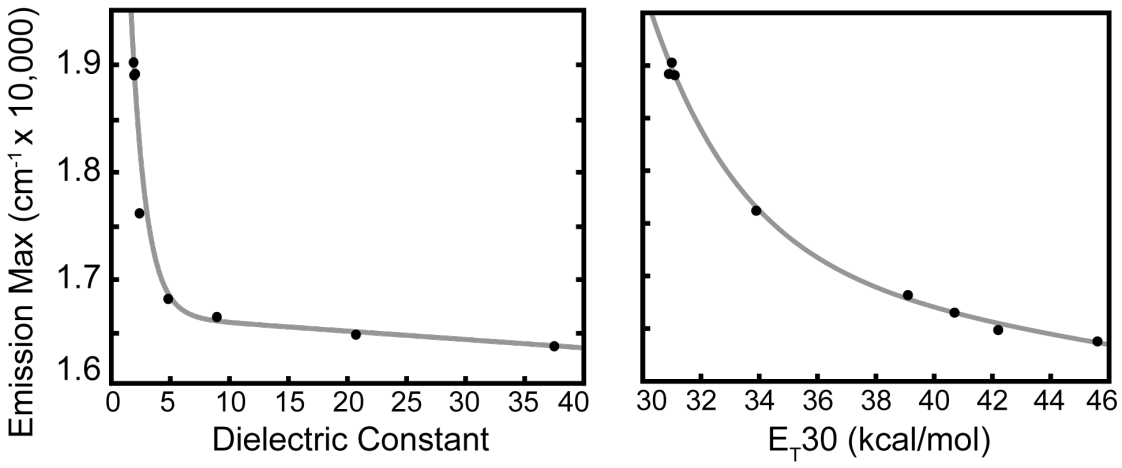

Figure 2.5: (a) NR fluorescence emission maximum versus ε. Data are fit to a sum of two exponentials (grey line) of the form $E_F = Ae^{-B\varepsilon} + C^{-D\varepsilon}$ with best-fit parameters A = $(1.076 \pm 1.179) \times 10^4$, B = 0.8 ± 0.6, C = $(1.67 \pm 0.05) \times 10^4$ and D = 0.0005 ± 0.001. (b) NR emission maximum versus solvent E_T30 values. Best fit to a sum of two-exponentials is shown (grey line), with best-fit parameters A = $(3 \pm 20) \times 10^7$, B = 0.3 ± 0.25, C = $(1.8 \pm 0.4) \times 10^4$ and D = 0.003 ± 0.005.

Figure 2.7(b) demonstrates that environments for which $40 < \varepsilon < 80$ are not very probable, and comprise only 5% of the distribution. A second result in PVDF is that the ε distributions vary significantly between different regions of the film. The inset in Figure 2.7(b) presents a plot of the mean ε calculated for 10 individual scans with the error bars representing one standard deviation. This plot demonstrates the substantial variation in both the mean and width of the ε distribution in different regions of the PVDF film. This result validates the importance of investigating relatively large regions of polymer films in order to get a true sense of the total variation of ε, an investigation which is easily done using the quasi-SM technique. In comparison, a single 10×10 μm region of PMMA (Figure 2.7(a) inset) captures the full extent of the variation of ε, with the mean value of ε for 10 scans (taken from different regions of the film) falling within the standard deviation of a single scan. This result demonstrates that for PMMA variations in ε only occur on sub-micron length scales.

Given the limited variation in NR emission energy at higher ε we explored an alternate method of characterizing the polymer environment in terms of E_T30 values.[25] Figure 2.5(b) presents the NR emission maximum versus E_T30 for the solvents studied.[24,26] The variation in emission maximum with E_T30 was best fit to a sum of two exponentials with best fit corresponding to $A = (3 \pm 20) \times 10^7$, $B = 0.3 \pm 0.25$, $C = (1.8 \pm 0.4) \times 10^4$ and $D = 0.003 \pm 0.005$. The figure demonstrates that greater variation in the NR emission maximum at higher E_T30 is observed in comparison to the dependence on ε described above. Similar findings have been reported by Deye *et al.*[27] Using the best fit, the distribution of E_T30 values in both PMMA and PVDF were determined as shown in Figure 2.7. Similar to dielectric constant, the distribution of E_T30 in PMMA is narrow, and becomes significantly broader in PVDF, which exhibits a right skew in the distribution indicating the presence of regions with considerable polarity.

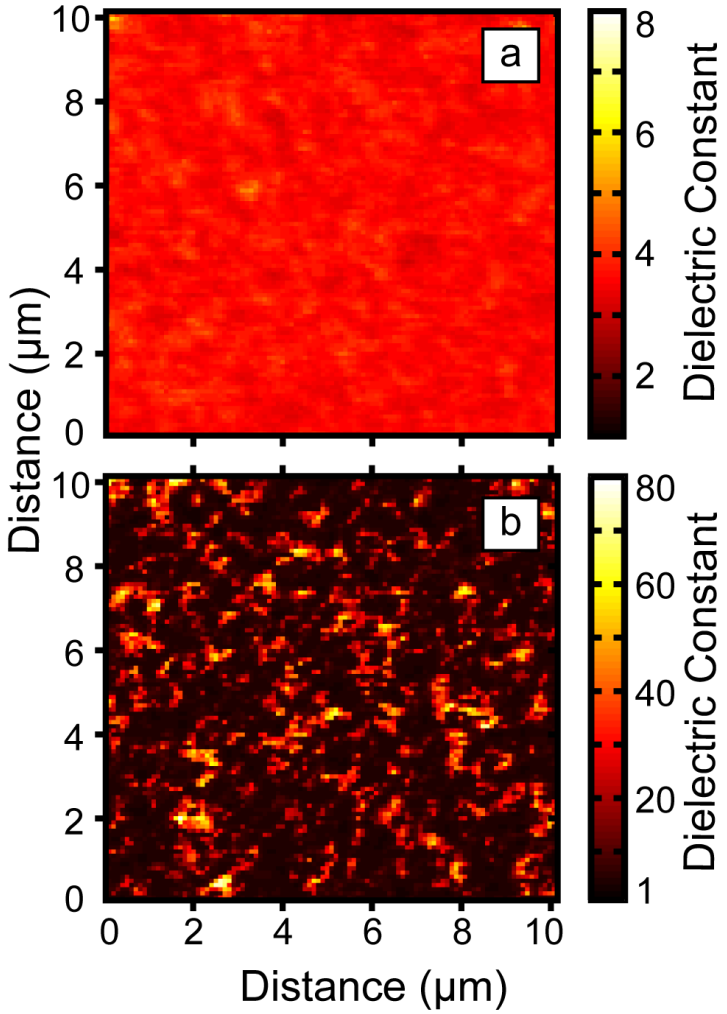

Figure 2.6: 10 × 10 μm images depicting the spatial distribution in ε for the same scans as in Figure 2.3. Images correspond to the polymer's dielectric constant versus position in the film. Note the order of magnitude difference in the color bar scale between (a) and (b).

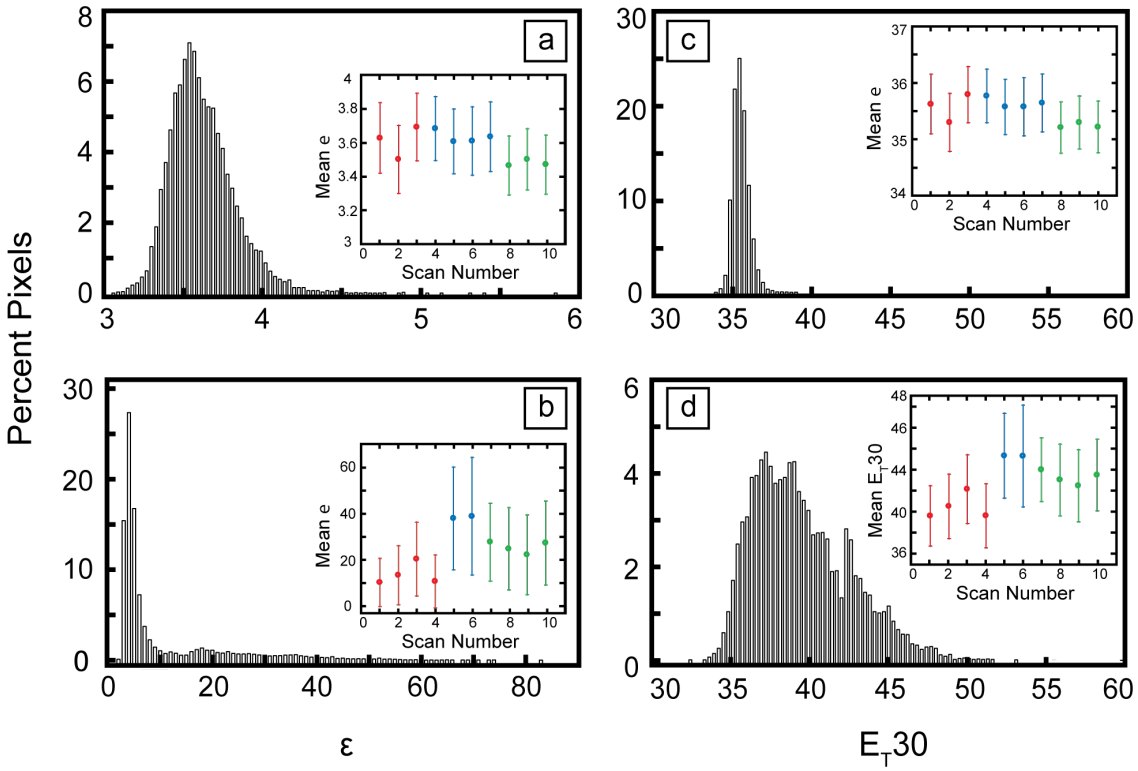

Figure 2.7: Histograms representing the distribution of ε and E_T30 values from the 10 $\times$ 10 μm scans in Figure 2.3. Shown are dielectric distributions in (a) PMMA (ε_{mean} = 3.64 $\pm$ 0.21, ε_{mode} = 3.55) and (b) PVDF (ε_{mean} = 10.72, ε_{mode} = 16.99). Also shown are distributions of E_T30 values in (c) PMMA (mean = 35.64 $\pm$ 0.51) and (d) PVDF (mean = 39.61 $\pm$ 3.05). Each histogram is comprised of 100 bins. The insets in (a) through (d) show the mean value of ε determined for 10 individual scans (error bars: one standard deviation). The data of the same color represent adjacent areas while the distances between red, blue and green regions are $\sim$1 mm.

2.5 Conclusion

The results presented here demonstrate that quasi-SM microscopy can be used to measure both the distribution and spatial variation in dielectric environments in polymer films from sub-micron to millimeters. Compared to previous techniques employed to measure the dielectric constant of polymers, this approach is flexible, efficient, and allows for the measurement of the spatial variation in dielectric constant. Using this approach, the variation of ε in films of PMMA and PVDF was determined. PMMA exhibited a narrow distribution of dielectric environments while the corresponding distribution in PVDF is much broader. Perhaps the most intriguing capability of the quasi-SM measurements is the ability to map out the spatial variation of ε in the polymer films (Figures 2.6(a) and (b)). Time-resolved applications of this technique could be used to provide information on the time and length scales for the interchange of dielectric environments in polymer films, information that would be critical in testing current models of dynamic heterogeneity in polymers.[28–30] In summary, quasi-SM confocal microscopy provides a novel approach to classifying and studying the dielectric environments of polymer films.

2.6 Acknowledgements

This work was supported by the National Science Foundation (DMR 1005819). Part of this work was conducted at the University of Washington NanoTech User Facility, a member of the NSF National Nanotechnology Infrastructure Network (NNIN). EAR was supported in part by the UW NIEHS-sponsored Biostatistics, Epidemiologic and Bioinformatic Training in Environmental Health (BEBTEH) Training Grant, Grant #: NIEHS T32ES015459.

2.7 Supporting Information

This information is available free of charge via the internet at http://pubs.acs.org.

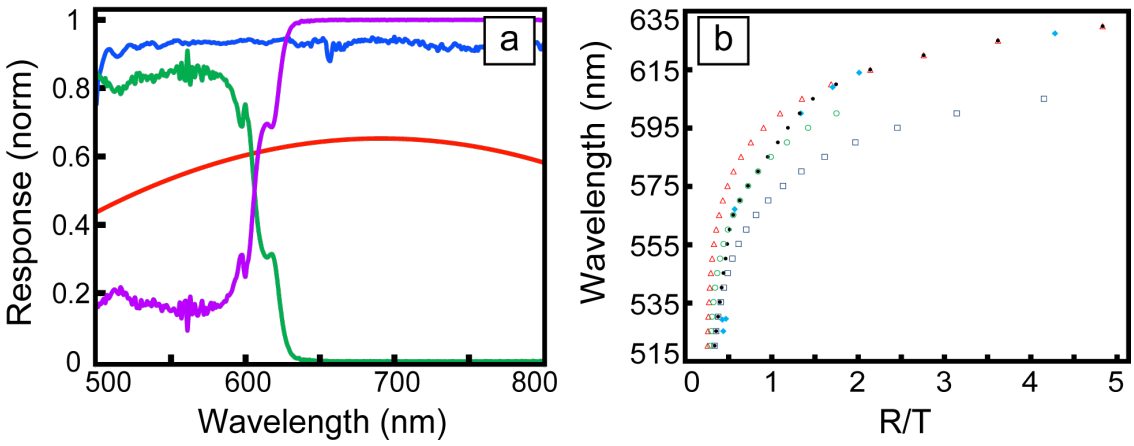

Figure 2.8: Plots representing the method used to transform R/T to emission wavelength max. (a) APD efficiency curve (red), emission filter transmission curve (blue), and 600-nm dichroic reflectance (purple) and transmission (green) curves used to calculate the expected reflected and transmitted spectra. (b) Curves representing the relationship between emission wavelength and R/T values as obtained from shifting the bulk fluorescence spectrum of hexane (dark blue square), toluene (green circle) and acetonitrile (red triangle) and convolving with the curves presented in (a). Black circles represent the "hybrid" curve, constructed by weighing the variation in NR emission line shape with a change in solvent polarity, used to accurately transform R/T to wavelength. Blue diamonds represent the R/T values measured for NR solutions on the microscope for verification of the "hybrid" curve's accuracy.

2.8 Bibliography

[1] Fumagalli, L., Ferrari, G., Sampietro, M., & Gomila, G. (2009). *Nano Letters* **9**, 1604–1608.

[2] Riedel, C., Arinero, R., Tordjeman, P., Lévêque, G., Schwartz, G., Alegría, A., & Colmenero, J. (2010). *Physical Review E* **81**, 010801.

[3] Riedel, C., Sweeney, R., Israeloff, N., Arinero, R., Schwartz, G.A., Alegría, A., Tordjeman, P., & Colmenero, J. (2010). *Applied Physics Letters* **96**, 213110.

[4] Bale, D.H., Eichinger, B.E., Liang, W., Li, X., Dalton, L.R., Robinson, B.H., & Reid, P.J. (2011). *The Journal of Physical Chemistry B* **115**, 3505–3513.

[5] Serghei, A., Tress, M., & Kremer, F. (2006). *Macromolecules* **39**, 9385–9387.

[6] Crider, P., Majewski, M., Zhang, J., Oukris, H., & Israeloff, N. (2007). *Applied Physics Letters* **91**, 013102–013102.

[7] Greenspan, P. & Fowler, S.D. (1985). *Journal of Lipid Research* **26**, 781–789.

[8] Levitsky, I., Krivoshlykov, S.G., & Grate, J.W. (2001). *Analytical Chemistry* **73**, 3441–3448.

[9] Hou, Y., Bardo, A.M., Martinez, C., & Higgins, D.A. (2000). *The Journal of Physical Chemistry B* **104**, 212–219.

[10] Rei, A., Ferreira, M.I.C., & Hungerford, G. (2008). *Journal of Fluorescence* **18**, 1083–1091.

[11] Freidzon, A.Y., Safonov, A.A., Bagaturyants, A.A., & Alfimov, M.V. (2012). *International Journal of Quantum Chemistry* **112**, 3059–3067.

[12] Martins, P., Nunes, J.S., Hungerford, G., Miranda, D., Ferreira, A., Sencadas, V., & Lanceros-Mendez, S. (2009). *Physics Letters A* **373**, 177–180.

[13] Gross, S., Camozzo, D., Di Noto, V., Armelao, L., & Tondello, E. (2007). *European Polymer Journal* **43**, 673–696.

[14] Brandrup, J., Immergut, E.H., Grulke, E.A., Abe, A., & Bloch, D.R. (1999). *Polymer Handbook*, Volume 89. Wiley New York.

[15] Ameduri, B. (2009). *Chemical Reviews* **109**, 6632–6686.

[16] Satapathy, S., Pawar, S., Gupta, P., & Varma, K. (2011). *Bulletin of Materials Science* **34**, 727–733.

[17] Riley, E.A., Hess, C.M., Pioquinto, J.R.L., Kaminsky, W., Kahr, B., & Reid, P.J. (2012). *The Journal of Physical Chemistry B* **117**, 4313–4324.

[18] Lovinger, A.J. (1982). In *Developments in Crystalline Polymers–1*, pp. 195–273. Springer.

[19] Dutta, A.K., Kamada, K., & Ohta, K. (1996). *Journal of Photochemistry and Photobiology A: Chemistry* **93**, 57–64.

[20] Jee, A.Y., Park, S., Kwon, H., & Lee, M. (2009). *Chemical Physics Letters* **477**, 112–115.

[21] Kim, H.H., Song, N.W., Park, T.S., & Yoon, M. (2006). *Chemical Physics Letters* **432**, 200–204.

[22] Marcus, R. (1990). *Journal of Physical Chemistry* **94**, 4963–4966.

[23] Kawski, A., Bojarski, P., & Kukliński, B. (2008). *Chemical Physics Letters* **463**, 410–412.

[24] Reichardt, C. (1994). *Chemical Reviews* **94**, 2319–2358.

[25] Rauf, M.A., Soliman, A.A., & Khattab, M. (2008). *Chemistry Central Journal* **2**, 1–8.

[26] Deng, Q., Li, Y., Wu, J., Liu, Y., Fang, G., Wang, S., & Zhang, Y. (2012). *Chemical Communications* **48**, 3009–3011.

[27] Deye, J.F., Berger, T.A., & Anderson, A.G. (1990). *Analytical Chemistry* **62**, 615–622.

[28] Gebremichael, Y., Schrøder, T., Starr, F.W., & Glotzer, S. (2001). *Physical Review E* **64**, 051503.

[29] Ediger, M.D. (2000). *Annual Review of Physical Chemistry* **51**, 99–128.

[30] Wolynes, P.G. (2009). *Proceedings of the National Academy of Sciences* **106**, 1353–1358.

Chapter 3

IMAGING THE EFFECTS OF ANNEALING ON THE POLYMORPHIC PHASES OF POLY(VINYLIDENE FLUORIDE)

Chelsea M. Hess, Angela R. Rudolph, and Philip J. Reid

Department of Chemistry, University of Washington, Box 351700, Seattle, WA 98195, United States

Reproduced with permission from Hess, C.M.; Rudolph, A.R.; Reid, P.J., *The Journal of Physical Chemistry B* **2015**, Article ASAP. DOI: 10.1021/jp512486n.

3.1 Abstract

The effect of annealing on the phase transformation and the dielectric properties of poly(vinylidene fluoride) (PVDF) is explored using quasi-single molecule (quasi-SM) microscopy. The solvatochromic properties of nile red (NR) are employed to measure the spatial distribution of the local dielectric constant (ε) in $\sim$30 μm thick PVDF films before and after annealing at 90 °C. The results presented here demonstrate that non-annealed films exhibit much larger ε distributions, both in terms of magnitude and distribution, when compared to annealed films. The polymorphic phase of PVDF before and after annealing is also confirmed using X-ray diffraction. Non-annealed films are found to be in the γ-phase with annealing promoting the transition to primarily β-phase. Combining these results, we conclude that the decrease in ε with annealing time is due to the phase transformation from γ- to β-phase. Using quasi-SM imaging techniques one can readily visualize the ε environments present within different polymorphic phases of PVDF.

3.2 Introduction

Poly(vinylidene fluoride) (PVDF) is a semi-crystalline polymer that is of interest for its unique pyro- and piezoelectric properties which arise from the polymorphic phases PVDF exhibits.[1] Current interest in PVDF involves understanding the relationship between polymorphic composition and crystallization conditions,[2–4] which ultimately influence the dielectric properties of the polymer.[5] The three most common phases of PVDF (Figure 3.1) are the non-polar α-phase (cis-trans conformation), polar and ferroelectric β-phase (all trans conformation), and γ-phase (kinked all trans conformation). Interconversion between these phases is induced through electric-field poling,[6] annealing,[2] or mechanical straining (i.e., "stretching" or "drawing").[7,8]

Previously, X-ray diffraction (XRD) and infrared spectroscopy have been employed to study the relationship between crystallization conditions and the polymorphic composition of PVDF.[2,8] While both of these techniques provide information on the phase of PVDF, these techniques provide limited information on the microscopic details of phase transformations. In 2009, Martins *et al.* explored the relationship between polymorphic phase and the dielectric properties of PVDF. By employing the solvatochromic organic dye nile red (NR), they were able to monitor the effect of "stretching" a PVDF film, which induced a transition from α- to β-phase, with the observed shift in the NR emission to longer wavelengths consistent with increased polarity of the β-phase.[5]

In this manuscript, we explore the effect of annealing on the dielectric properties of PVDF using our developed quasi-single molecule (quasi-SM) technique that measures the spatial variation in the dielectric constant (ε) in polymer films.[9] By employing the solvatochromic properties of NR embedded in non-annealed and annealed PVDF films, we are able to spatially map the dielectric environments present within a polymer before and after annealing. The results presented here demonstrate that PVDF non-annealed films contain much larger values of ε as compared to that of annealed

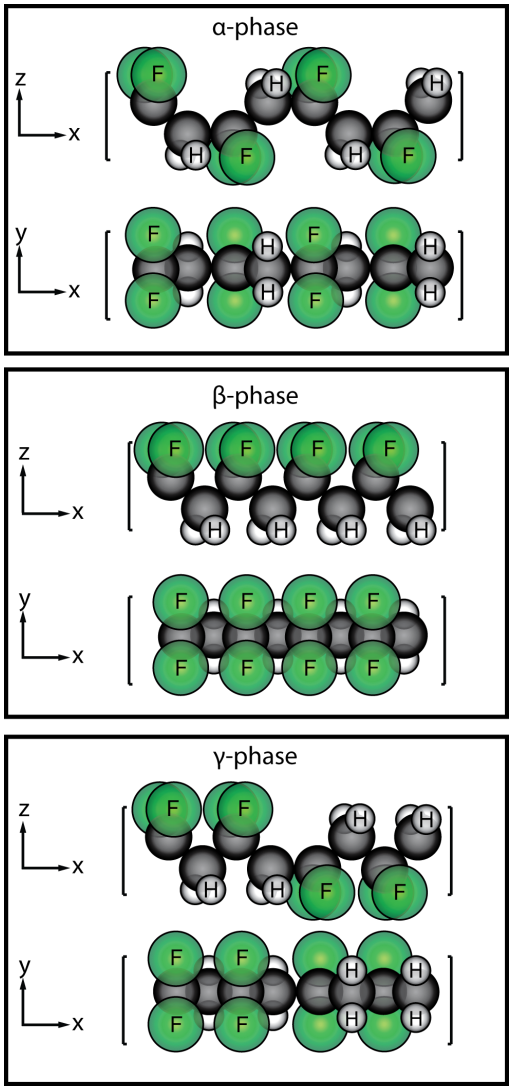

Figure 3.1: Space filling models illustrating the three polymorphic phases of PVDF. The α-phase (top) is non-polar with a cis-trans conformation. The β-phase (middle) is ferroelectric and polar with an all trans conformation. The γ-phase (bottom) is a kinked all trans conformation.[1] Green = fluorine, white = hydrogen, and black = carbon.

films, with a continuous decrease in ε with annealing time.

In addition, we have measured the effect of phase transformation on the dielectric properties of PVDF. Specifically, by varying the annealing conditions we can alter the polymorphic phase of PVDF. Through the use of XRD, non-annealed films of PVDF are found to be in the γ-phase, and annealing at 90 °C promotes transformation to the β-phase. By connecting this result with the corresponding evolution in ε measured for annealed and non-annealed films, we establish a direct correlation between the polymorphic phase of PVDF and the corresponding dielectric properties of the polymer.

3.3 Experimental

3.3.1 Sample Preparation

Films of nile red (NR, Aldrich, 99+% pure by LC-MS) embedded in poly(vinylidene fluoride) (PVDF, Sigma-Aldrich, MW ≈ 534000 by GPC) were prepared as follows. A 3.1×10^{-5} M solution of NR and a 15 wt.% PVDF solution was prepared in dimethyl sulfoxide (DMSO, EMD Chemicals INC., ACS grade). In order to produce NR concentrations suitable for this experiment, aliquots of the NR solution were added to the 15 wt.% polymer solution to produce a final NR concentration of $\sim 1 \times 10^{-6}$ M which we will later refer to as quasi-single molecule (quasi-SM). Indium tin oxide (ITO) coated coverslips (SPI Supplies, 70-100 ohms) were cleaned using multi-purpose detergent (Meri-suds, CH_2O Inc.), rinsed with nanopure water (Barnstead, NANOpure II), dried with nitrogen gas, and irradiated in a UV-box for one hour. NR/PVDF films were deposited onto the coverslips by taking the 1×10^{-6} M NR in 15 wt.% PVDF/DMSO solution heated to 90 °C and spin coating this solution onto the cleaned ITO coated coverslips at room temperature for 45 s at 700 rpm. These non-annealed films were left at room temperature for 1 hour and then dried in a 60 °C oven until dry (∼1.5 hours). Annealed films were prepared by placing the samples

directly into a room temperature oven after spin coating. The oven temperature was then ramped to 90 °C at a rate of 2 °C/min. Once the oven reached 90 °C the films remained in the oven for time periods of 0.625 hours, 1.25 hours, 1.825 hours, 2.5 hours and 5 hours. Films annealed for shorter than 0.625 hours are not included in this study as 0.625 hours is the minimum amount of time required to dry the films at 90 °C. The annealed and non-annealed films were ∼30 μm thick as measured with a high accuracy micrometer.

3.3.2 Polymorphic Phase Analysis

Non-annealed films were confirmed to be in the γ-phase through X-ray diffraction (XRD, Bruker AXS, D8 Discover w/ GADDS) (Figure 3.2) as evidenced by two diffraction peaks near $2\theta = 20°$.[2] In contrast, annealed films were found to contain both α- and β-phases as evidenced by the XRD spectrum (Figure 3.2) with multiple peaks observed corresponding to the two phases (α-phase peaks: $2\theta = 17.8°$, 18.4°, 19.9°, 26.6°; β-phase peaks: $2\theta = 20.7°$, 20.8°) in agreement with the literature.[2,10] Given the overlap between the α- and β-phase peaks at $2\theta = 20°$ it is difficult to calculate the exact percent crystallinity of the film from XRD; therefore, alternate characterization methods were employed. Specifically, measurement of the ferroelectric properties of the annealed films can differentiate between phases since the β-phase is ferroelectric while the α-phase is not. Using adhesive copper tape on top of the sample as one electrode and the conductive ITO coverslip as the other, an electric field of 1000 kV/cm was applied to the film. This resulted in a clear hysteresis loop with remnant polarization = 6.6 μC/cm^2, consistent with the ferroelectric annealed films having a larger amount of β-phase relative to α-phase.[1,2]

3.3.3 Confocal Microscopy

Emission images of the films were obtained using an inverted scanning confocal microscope described in detail elsewhere.[9,11] Briefly, a circularly polarized 488-nm

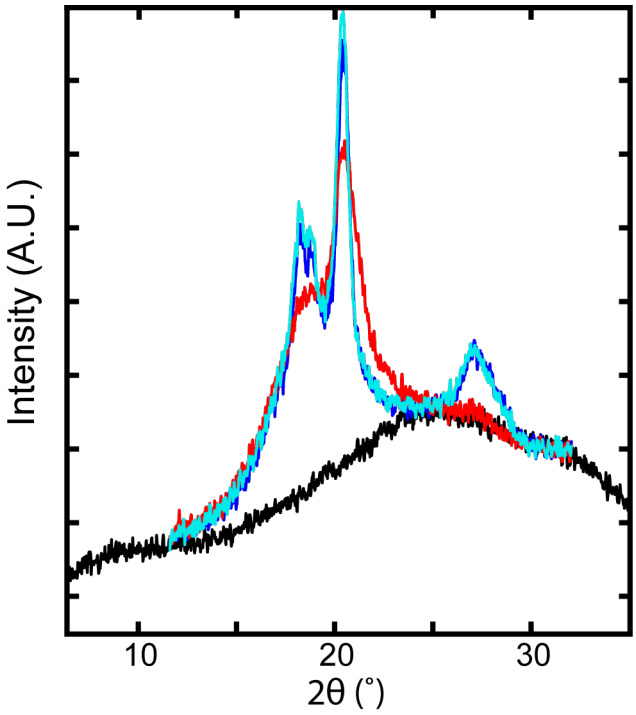

Figure 3.2: X-ray diffraction pattern of a blank ITO coated coverslip (black), a NR/PVDF non-annealed film (red), a NR/PVDF film annealed for 0.625 hours (light blue), and a NR/PVDF film annealed for 5 hours (dark blue). The peaks present in the non-annealed film are consistent with the film being in the γ-phase while the annealed films both exhibit peaks representative of both α- and β-phase.

(Novalux, Protera) excitation field of ∼3 μW was used to excite all orientations of the dye within the films. By raster scanning the film across the objective (Nikon, Plan-Fluor) focal volume in 100 nm steps, the emission from the quasi-SM film was split by a 600-nm short-pass dichroic mirror. Transmitted (T) and reflected (R) fields were then focused on two separate avalanche photodiode detectors (APD, PerkinElmer SPCM-AQR-16). Ten 10 μm × 10 μm fluorescence intensity images were collected from multiple films processed at each time point by employing an integration time of 0.2 s per 100 nm step.

3.3.4 Data Analysis

All data processing was performed in MATLAB (version R2014a) as described previously.[9,11] Images were collected and processed by calculating the ratio of the reflected and transmitted (R/T) intensities for each pixel of 10 × 10 μm image scans acquired at each annealing time. R/T values were transformed to emission wavelength maxima by first convolving ensemble NR fluorescence spectra in various solvents with the APD efficiency curves, the emission filter transmission curve, and the 600-nm dichroic reflectance and transmission curves in order to calculate the expected R and T spectra. A calibration curve that takes into account the emission line shape of NR in solvents of differing polarity was determined and used to transform the R/T ratio into emission wavelength maximum. The emission wavelength maximum was converted to maximum emission energy, and the solvatochromic property of NR was employed for a final conversion from maximum emission energy to dielectric constant. As described previously the function that converts emission energy max (ΔE_{00}) to dielectric constant (ε) is a two-term exponential function of the form:

$$\Delta E_{00}\left(cm^{-1}\right) = 1.077 \times 10^{4} e^{-0.8\varepsilon} + 1.67 \times 10^{4} e^{-5\times 10^{-4}\varepsilon} \tag{3.1}$$

All conversions have been fully presented elsewhere.[9,11]

3.4 Results and Discussion

Poly(vinylidene fluoride) (PVDF) is known to demonstrate multiple polymorphic phases illustrated in Figure 3.1(a-c). These phases correspond to different conformations of the polymer chain and the associated crystalline structures. For instance, the α-phase is non-polar with anti-parallel chains of the pattern TGTG'. PVDF in the β-phase is polar with parallel chains of the pattern TTTT, and is the only phase that is ferroelectric (i.e., contains polar crystals whose polarization direction can be reversed by application of an electric field). The γ-phase conformation is an intermediate between that of the α- and β-phases with a TTTGTTTG' pattern commonly viewed as a kinked all-trans conformation. Interconversion between these phases is accomplished through electric-field poling, annealing, or mechanical straining.[1]

Our interest here is the effect annealing has on the properties of PVDF. First, the annealing time was varied between 0.625 and 5 hours, and the corresponding interconversion between the PVDF phases was measured using XRD as shown in Figure 3.2. Non-annealed films were found to be in the γ-phase while annealed films were found to contain both α- and β-phases. For reference, a γ-phase diffraction pattern consists of two peaks adjacent to each other near $2\theta = 20^\circ$ while the α- and β-phase patterns demonstrate substantially more diffraction peaks (α-phase peaks: $2\theta = 17.8^\circ, 18.4^\circ, 19.9^\circ, 26.6^\circ$; β-phase peaks: $2\theta = 20.7^\circ, 20.8^\circ$).[2,10] The overlap between the α- and β-phase peaks around $2\theta = 20^\circ$ makes it difficult to calculate the exact percent crystallinity of the film. Therefore, alternate characterization methods were employed to establish the presence of the β-phase. Since the β-phase is the only phase of PVDF that is ferroelectric we characterized the ferroelectric behavior of the films. Copper tape was placed on top of the film to provide one electrode, the conductive ITO coverslip provided the other, and an electric field of 1000 kV/cm (100 V/μm) was applied to the film. This resulted in a clear hysteresis loop with remnant polarization = 6.6 μC/cm^2 (1.75 C/m^2), consistent with the ferroelectric annealed films having a

larger amount of β-phase relative to α-phase.[1,2] This result, in combination with the XRD results, demonstrates that annealing promotes the transition of PVDF from γ- to largely β-phase.

Given the XRD results presented above, we became interested in exploring the relationship between polymorphic phase and local dielectric constant (ε) in PVDF. Similar to our previous studies on NR embedded in PVDF, the solvatochromism of NR was used to determine the distribution of ε present within annealed (γ-phase) and non-annealed (primarily β-phase) films.[9,11] In these studies the annealing time was varied as follows: 0.625 hours, 1.25 hours, 1.825 hours, 2.5 hours and 5 hours. By measuring the variation in emission wavelength max of NR across several 10 μm × 10 μm images of annealed and non-annealed films at quasi-SM concentrations (i.e., luminophore number density of ∼10 molecules/(μm^2), we were able to spatially resolve this variation versus position in the film.[9] Figure 3.3(a-f) presents images of this spatial variation in the NR emission maximum for annealed and non-annealed films. The figure demonstrates that a substantial change in the emission maximum occurs with annealing. The majority of the emission from the annealed film is blue shifted in comparison to the non-annealed film, with continued blue shifting of the emission maximum as the annealing time increases. This evolution is shown in Figure 3.4, where a clear blue shift in the emission maximum is observed with increasing annealing time. The emission maximum distributions presented in Figure 3.4(a-c) were compiled from 10 individual scans at each annealing time. The average emission wavelengths ($\lambda_{average}$) for the three annealing times presented in Figure 3.4 are $\lambda_{average}$ (non-annealed) = 620 nm, $\lambda_{average}$ (annealed 0.625 hours) = 595 nm, and $\lambda_{average}$ (annealed for 5 hours) = 588 nm corresponding to images (a), (b), and (f) in Figure 3.3, respectively.

The distribution of NR emission wavelength maxima can be transformed to a distribution of ε as follows.[9,11] Specifically, the NR emission wavelength maximum is converted to emission energy (ΔE_{00}) and then connected to ε using the following two-

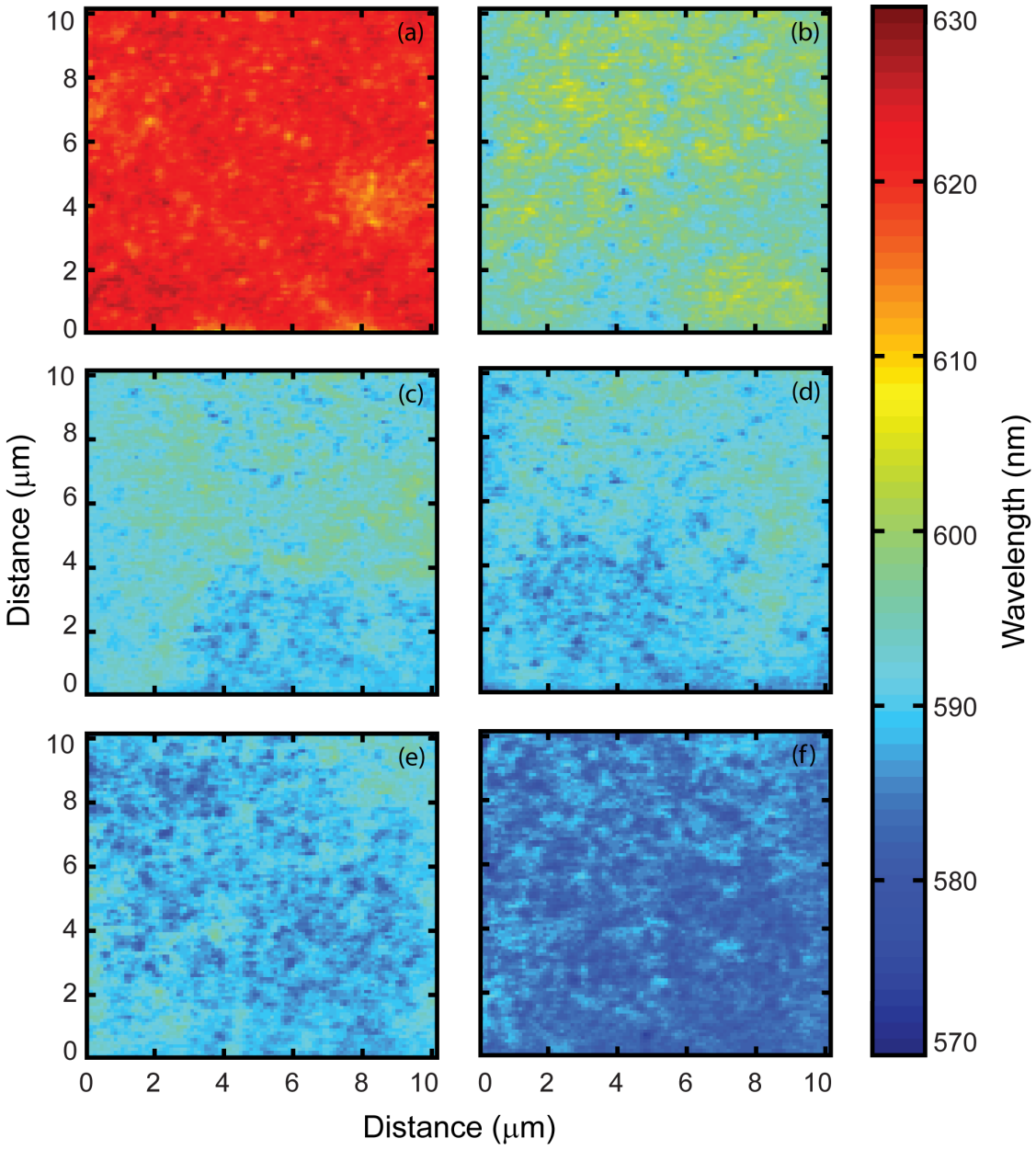

Figure 3.3: 10 μm × 10 μm images of the spatial variation in NR emission wavelength maximum in PVDF films that are (a) non-annealed or annealed at 90 °C for (b) 0.625 hours, (c) 1.25 hours, (d) 1.825 hours, (e) 2.5 hours, and (f) 5 hours.

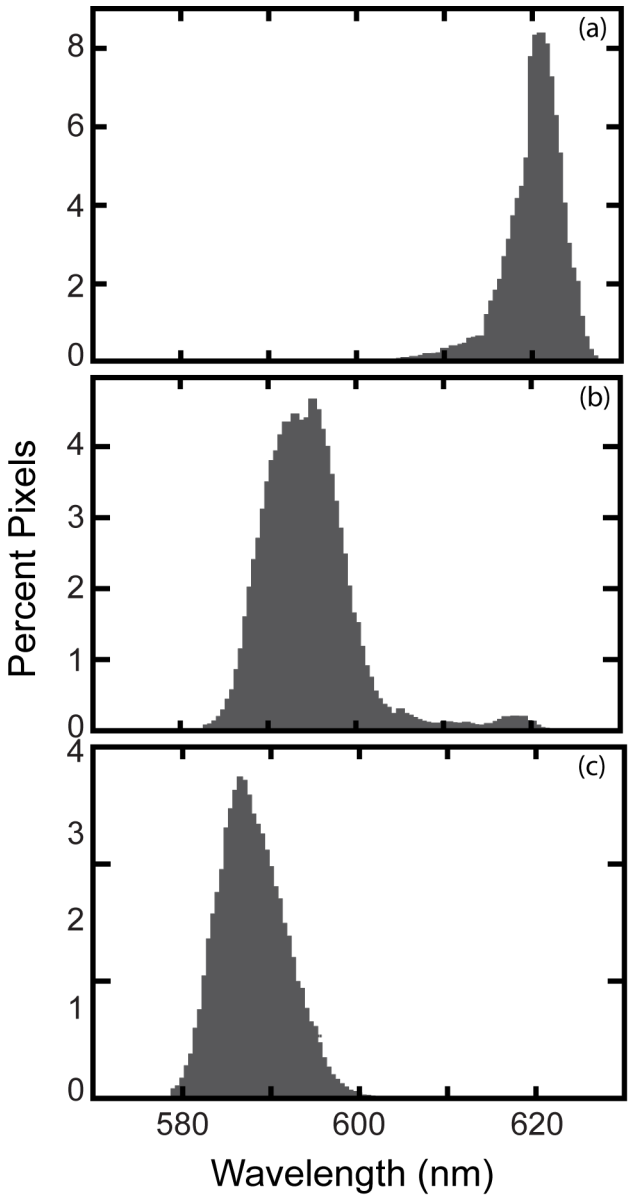

Figure 3.4: Histograms representing the distribution of emission wavelength observed from NR/ PVDF films that are (a) non-annealed and annealed at 90 °C for (b) 0.625 hours and (c) 5 hours. Notice that with annealing time the average emission wavelength shifts to shorter wavelengths. Quantitatively, $\lambda_{average}$ (non-annealed) = 620 nm while $\lambda_{average}$ (annealed 0.625 hours) = 595 nm and $\lambda_{average}$ (annealed for 5 hours) = 588 nm. The histograms presented here contain the data from 10 individual scans collected from multiple films at each time point.

term exponential function.

$$\Delta E_{00}\left(cm^{-1}\right) = 1.077 \times 10^4 e^{-0.8\varepsilon} + 1.67 \times 10^4 e^{-5\times 10^{-4}\varepsilon} \tag{3.1}$$

The above equation is used to convert each pixel of the emission wavelength images shown in Figure 3.3(a-f) to images of ε as shown in Figure 3.5(a-f). The figure shows that a significant difference in ε is observed between the annealed and non-annealed films, with non-annealed films demonstrating larger values of ε in comparison to annealed films, and the films continue to reduce ε as the annealing time increases. These trends are further evidenced in Figure 3.6(a-c) which presents histograms of ε values observed for 10 individual scans from multiple non-annealed, 0.625 hour annealed, and 5 hour annealed films. A much broader distribution of ε is observed in non-annealed versus annealed films consistent with a wide range of dielectric environments being present in the non-annealed films. To confirm that residual DMSO had little impact on these results, films were dried at 60 °C for up to 6 hours, and statistically similar distributions to the distribution presented in Figure 3.6(a) were observed. Attempts to increase the drying temperature resulted in annealing and corresponding conversion of the films to α- and β-phase. Finally, attempts to cast films from dimethylformamide resulted in non-annealed films that demonstrated predominately α- and β-phase as evidenced by measurement of the dielectric distributions and XRD. In summary, the results presented in Figure 3.6(a) are highly dependent on processing conditions.

Figure 3.7 presents plots of the average emission wavelength (λ_{average}) and mean dielectric constant ($\bar{\varepsilon}$) versus annealing time. For Figure 3.7(a), the average emission wavelength maximum was calculated from the emission wavelength histograms in Figure 3.4. For annealed films, the histograms were fit to Gaussian distributions to determine the mean (λ_{average}) and standard deviation (error bars). Figure 3.7(a) clearly demonstrates that λ_{average} decreases with increased annealing time. The ε trend (Figure 3.7(b)) is more difficult to quantify since the distributions for non-annealed and annealed films are significantly different (Figure 3.6(a) versus Figure 3.6(c)).

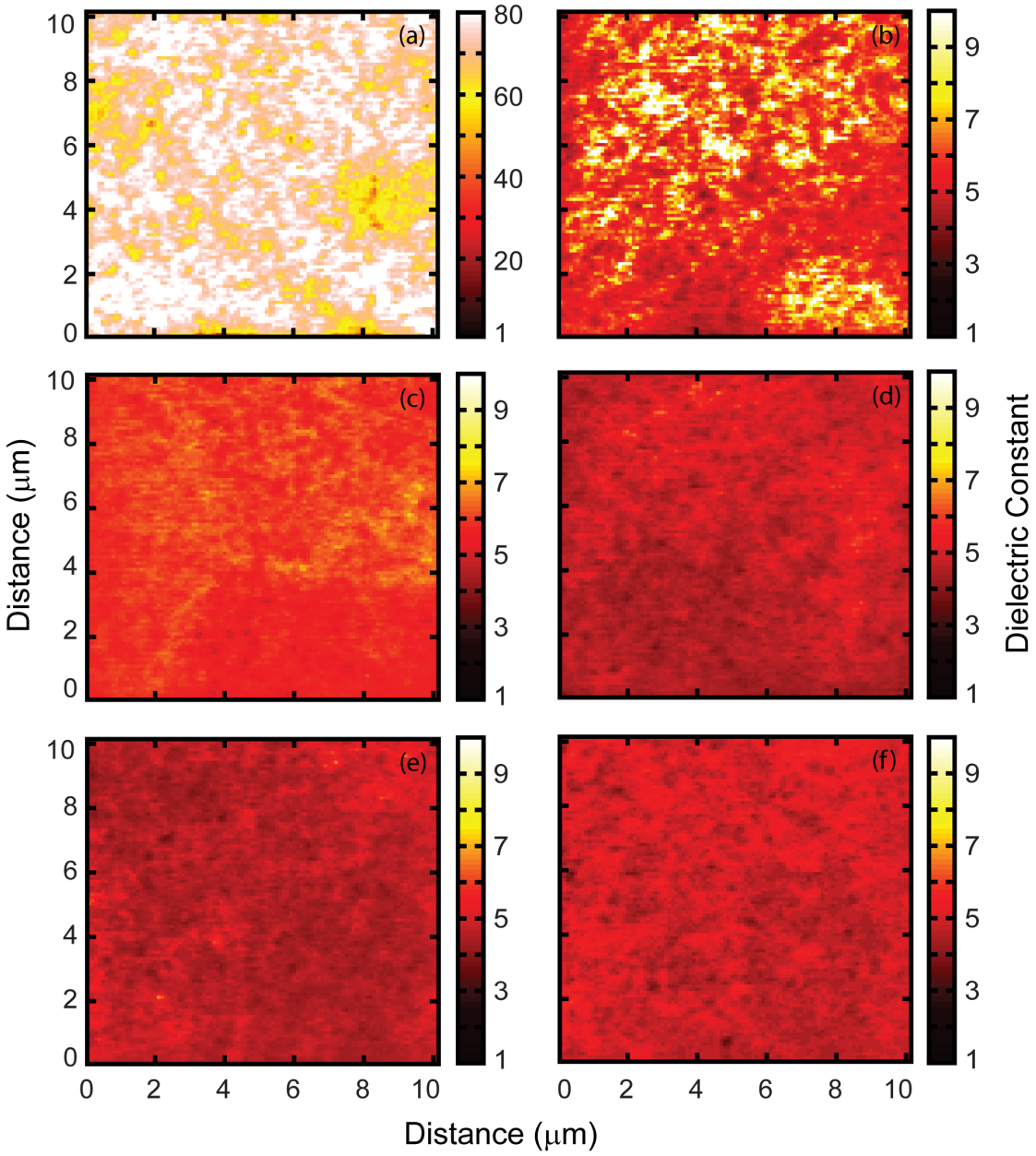

Figure 3.5: 10 μm × 10 μm images demonstrating the spatial variation in ε observed for NR/PVDF films that are (a) non-annealed and that have been annealed at 90 °C for (b) 0.625 hours, (c) 1.25 hours, (d) 1.825 hours, (e) 2.5 hours, and (f) 5 hours. Note the change in magnitude of the color bar scale from non-annealed to any annealed film.

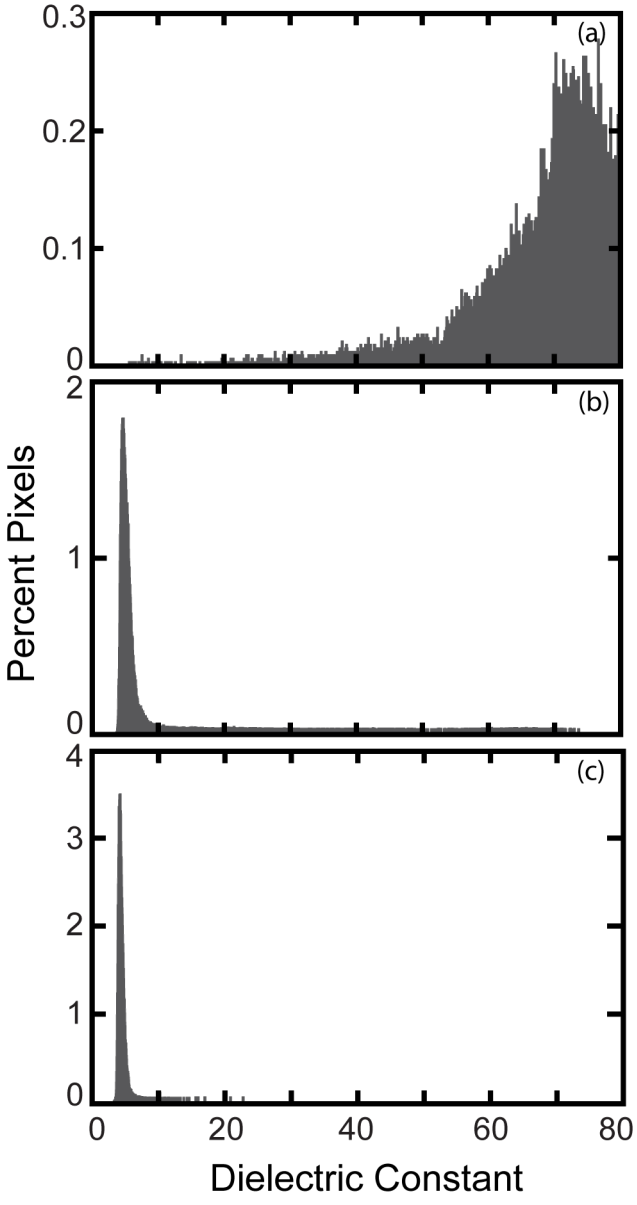

Figure 3.6: Histograms representing the distribution of ε observed for NR/ PVDF films that are (a) non-annealed and that have been annealed at 90 °C for (b) 0.625 hours and (c) 5 hours. Again, the histograms presented here contain the data from 10 individual scans collected from multiple films at each time point.

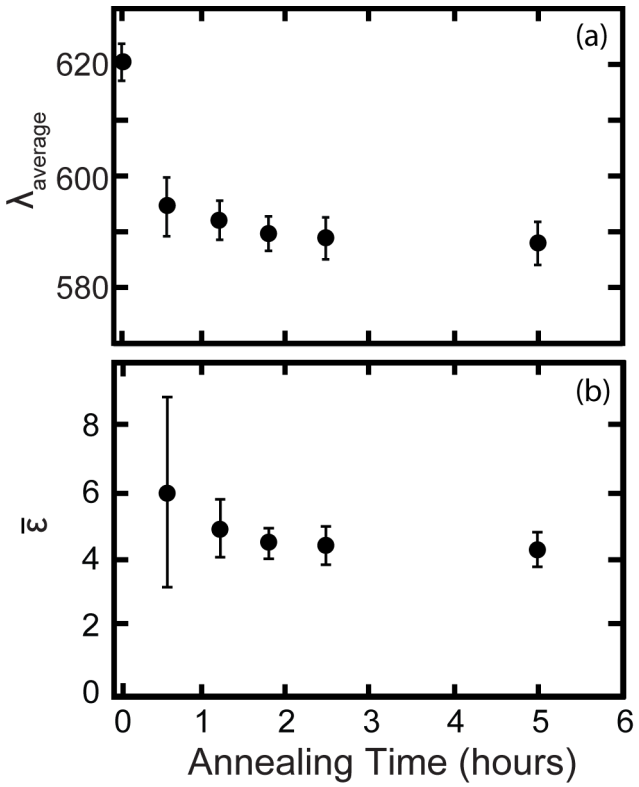

Figure 3.7: (a) Plot of average emission wavelength ($\lambda_{average}$) versus annealing time at a temperature of 90 °C. $\lambda_{average}$ values were calculated by fitting the distributions of emission wavelengths (Figure 3.4) to Gaussian distributions. Error bars correspond to the standard deviation of the Gaussian fit (width of the distribution). (b) Plot of the average ε ($\overline{\varepsilon}$) versus annealing time. For this plot, $\overline{\varepsilon}$ was calculated by fitting a given distribution of ε (Figure 3.6) to the heavy tailed Burr distribution. Error bars correspond to the standard deviation of the Burr distribution (width of the distribution). Note $\overline{\varepsilon}$ for non-annealed films is not presented since the ε distributions of these films is not well represented by a Burr distribution.

While a distribution function that best represents the non-annealed films was difficult to determine, the distributions from the annealed films were found to accurately fit to a Burr distribution (specifically, a Burr type XII distribution). The Burr distribution is a non-negative heavy tailed distribution with the following probability density function (PDF) and cumulative distribution function (CDF):[12]

$$\text{PDF} = ck\frac{x^{c-1}}{(1+x^c)^{k+1}},\ x \geq 0, k > 0, c > 0 \tag{3.2}$$

$$\text{CDF} = 1 - (1+x^c)^{-k},\ x > 0, c > 0, k > 0 \tag{3.3}$$

In the above expressions, c and k determine the shape of the distribution. The observation of a Burr distribution is interesting since it encompasses many common distributions such as lognormal and Weibull distributions that have previously been found to accurately describe single molecule photoluminescence intermittency of organic dyes in complex environments.[11,13,14] By plotting the mean ε ($\overline{\varepsilon}$) of the best fit Burr distribution versus annealing time, with error bars representing the standard deviation and therefore width of the distribution, we confirm the trend that increasing the time spent annealing results in a decrease in $\overline{\varepsilon}$ and a narrowing of the ε distribution.

Figure 3.8 further illustrates the dependence of dielectric constant on annealing through images of the variation in ε present within non-annealed and annealed films. In order to visually represent the ε domains present within these films, 1D line profiles are plotted in Figure 3.8(e) and (f) for non-annealed and annealed films, with the location of the line profile indicated by the dashed line in (c) and (d). This line profile provides further evidence that not only does ε decrease with annealing, but the range of ε is greater in non-annealed films. By plotting the change in ε as a function of both x and y positions in the film, we are able to obtain an even more visually accurate representation of the ε domains present in the PVDF films.

Finally, to correlate the ε trends to the polymorphic phases of PVDF, we return to the XRD spectra of annealed and non-annealed PVDF films. These data demonstrate

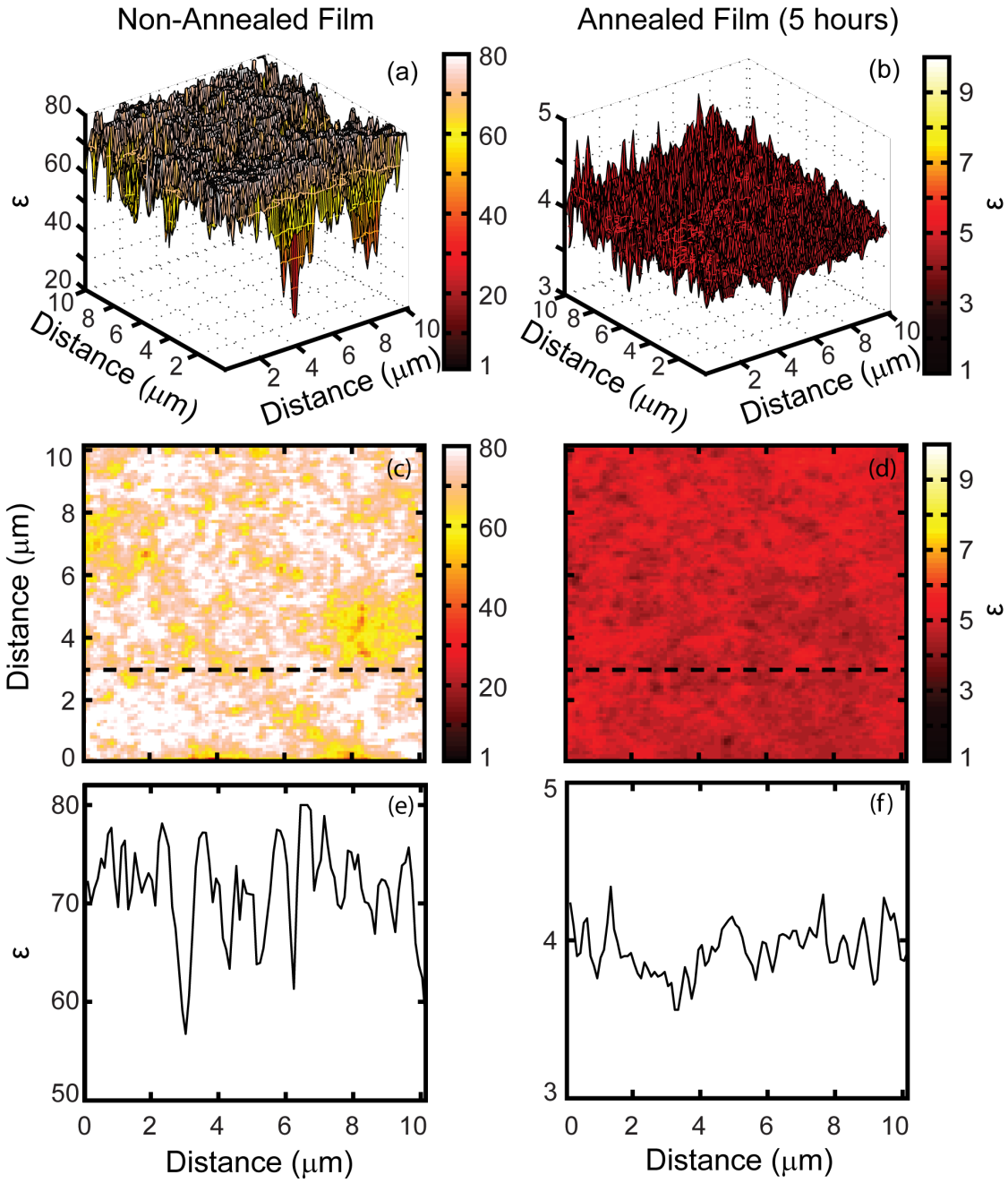

Figure 3.8: Representations of the spatial variation in dielectric constant (ε) observed in NR/PVDF films. Variation in ε across the entire 10 $\times$ 10 μm film is presented for (a) a non-annealed film and (b) for a film that annealed for 5 hours. Note the difference in the color bar scale and ε axis between the two films. Corresponding 2D representation of the variation in ε for (c) a non-annealed film and (d) for a film annealed 5 hour annealed film. The dashed line in (c) and (d) represent the region of the film used to derive the line plots shown in (e) and (f), respectively, demonstrating the spatial variation in ε across these films.

that annealing results in conversion of PVDF from γ-phase to primarily β-phase. Since ε decreases with annealing time, we conclude that the decrease in ε with annealing time is due to the phase transformation from γ- to β-phase. This establishes a correlation between the polymorphic phase of PVDF and ε. Furthermore, the imaging techniques employed here provide a visualization of the effect of phase transformation upon annealing. The results presented here provide support for the hypothesis that the γ-phase is a "kinked" all-trans conformation where the combination of regions of non-polar α-phase with polar β-phase drastically influences the polarizability of the film. This accounts for the extremely large magnitude in ε that we observe, in addition to the broadness of the ε distribution in Figure 3.6. On the other hand, upon annealing, some of the non-ferroelectric α-phase domains shift, allowing for more ferroelectric β-phase domains to exist in the films. This is supported by the increased ferroelectric properties of the film with annealing. As these annealed films contain more β-phase, ε shifts toward lower values consistent with ensemble measurements.[15]

3.5 Conclusion

We have established a direct correlation between the polymorphic phase of PVDF and ε through the use of X-ray diffraction and quasi-SM microscopy. XRD patterns of PVDF films indicate that annealing at 90 °C promotes interconversion from γ-phase to primarily β-phase. By monitoring the effect of annealing time on ε through the use of quasi-SM microscopy, a clear trend to smaller ε with increased annealing time was established. Combining these results, we conclude that the decrease in ε with annealing time is due to the phase transformation from γ- to β-phase. PVDF γ-phase films were found to exhibit much larger ε distributions, both in the magnitude of ε and the broadness of the distribution as compared to β-phase films. Finally, the quasi-SM imaging technique described here allows for visualization of the ε environments present within different polymorphic phases of PVDF.

3.6 Acknowledgements

This material is based upon work supported by the National Science Foundation under DMR 1005819 and CHE 1404674. XRD characterization studies were conducted at the University of Washington NanoTech User Facility, a member of the NSF National Nanotechnology Infrastructure Network (NNIN).

3.7 Bibliography

[1] Lovinger, A.J. (1982). In *Developments in Crystalline Polymers–1*, pp. 195–273. Springer.

[2] Satapathy, S., Pawar, S., Gupta, P., & Varma, K. (2011). *Bulletin of Materials Science* **34**, 727–733.

[3] Salimi, A. & Yousefi, A. (2004). *Journal of Polymer Science Part B: Polymer Physics* **42**, 3487–3495.

[4] Branciforti, M.C., Sencadas, V., Lanceros-Méndez, S., & Gregorio, R. (2007). *Journal of Polymer Science Part B: Polymer Physics* **45**, 2793–2801.

[5] Martins, P., Nunes, J.S., Hungerford, G., Miranda, D., Ferreira, A., Sencadas, V., & Lanceros-Méndez, S. (2009). *Physics Letters A* **373**, 177–180.

[6] Sencadas, V., Costa, C., Moreira, V., Monteiro, J., Mendiratta, S., Mano, J., & Lanceros-Méndez, S. (2005). *e-Polymers* **5**, 10–21.

[7] El Mohajir, B.E. & Heymans, N. (2001). *Polymer* **42**, 5661–5667.

[8] Peng, Y. & Wu, P. (2004). *Polymer* **45**, 5295–5299.

[9] Hess, C.M., Riley, E.A., Palos-Chávez, J., & Reid, P.J. (2013). *The Journal of Physical Chemistry B* **117**, 7106–7112.

[10] Park, Y.J., Kang, Y.S., & Park, C. (2005). *European Polymer Journal* **41**, 1002–1012.

[11] Hess, C.M., Riley, E.A., & Reid, P.J. (2014). *The Journal of Physical Chemistry B* **118**, 8905–8913.

[12] Tadikamalla, P.R. (1980). *International Statistical Review/Revue Internationale de Statistique*, 337–344.

[13] Riley, E., Hess, C., Whitham, P., & Reid, P. (2012). *The Journal of Chemical Physics* **136**, 184508.

[14] Riley, E.A., Hess, C.M., & Reid, P.J. (2012). *International Journal of Molecular Sciences* **13**, 12487–12518.

[15] Brandrup, J., Immergut, E.H., Grulke, E.A., Abe, A., & Bloch, D.R. (1999). *Polymer Handbook*, Volume 89. Wiley New York.

Chapter 4

BEYOND POWER LAWS: A NEW APPROACH FOR ANALYZING SINGLE MOLECULE PHOTOLUMINESCENCE INTERMITTENCY

E. A. Riley, C. M. Hess, P. J. Whitham, and P. J. Reid

Department of Chemistry, University of Washington, Box 351700, Seattle, WA 98195, United States

4.1 Abstract

The photoluminescence intermittency (PI) exhibited by single emitters has been studied for over a decade. To date, the vast majority of PI analyses involve parsing the data into emissive and non-emissive events, constructing histograms of event durations, and fitting these histograms to either exponential or power law probability distribution functions (PDFs). Here, a new method for analyzing PI data is presented where the PI data are used directly to construct a cumulative distribution function (CDF), and maximum-likelihood estimation techniques are used to determine the best fit of a model PDF to the CDF. Statistical tests are then employed to quantitatively evaluate the hypothesis that the CDF (data) is represented by the model PDF. The analysis method is outlined and applied to PI exhibited by single CdSe/CdS core-shell nanocrystals and the organic chromophore violamine R isolated in single crystals of potassium acid phthalate. Contrary to previous studies, the analysis presented here demonstrates that the PI exhibited by these systems is not described by a power law. The analysis developed here is also used to quantify heterogeneity within PI data obtained from a collection of CdSe/CdS nanocrystals, and for the determination of statistically significant changes in PI accompanying perturbation of the emitter. In summary, the analysis methodology presented here provides a more statistically-robust approach for analyzing PI data.

4.2 Introduction

Single molecule (SM) spectroscopy has become an established technique for studying the structure and dynamics of complex systems on molecular length scales.[1–4] Central to these studies is the interpretation of SM emission characterized by discrete changes in emissive intensity with time, referred to as photoluminescence intermittence (PI) or "blinking". Current interest involves determining the underlying photophysical processes responsible for PI, and connecting blinking to the environmental fluctuations that impact PI.[4–10]

PI was first observed from single molecules of perylene embedded in *p*-terphenyl crystals at low temperature.[11] The perylene emission was analyzed by constructing histograms corresponding to the temporal duration of emissive and non-emissive events. Analysis of the histograms revealed that the event durations were exponentially distributed consistent with formation and decay of the lowest-energy triplet-state. Since this first observation of PI, a variety of single emitters have been studied in an attempt to identify the non-emissive states that are populated during PI.[12–14] An intriguing aspect of these studies is that the durations of emissive and non-emissive events are generally not exponentially distributed, and are thus not consistent with a first-order kinetic description of non-emissive or "dark" state formation and decay. In addition, emissive and non-emissive event durations can easily span more than five decades in time making the statistical analysis of PI data challenging.

The first step in connecting PI to underlying molecular processes is quantification of the emission statistics. Similar to the first studies of PI described above, the vast majority of current studies create histograms of emissive or "*on*" and non-emissive or "*off*" event durations, and then connects these histograms to probability distribution functions (PDF). For example, the *on*- and *off*-duration histograms for CdSe/CdS quantum dots and a variety of other systems were found to qualitatively follow a power-law PDF.[15] The power-law PDF is of the form $P(t) = At^{-\alpha}$ where α is the

power-law coefficient with reported values ranging between one and two. An interesting feature of the power-law PDF is that a single scaling parameter (α) describes the probability over all time rendering the PDF linear on a log-probability versus log-time plot. Indeed, a variety of single emitters demonstrate *on*- and *off*-event duration distributions that are apparently linear on a "log-log" plot consistent with a power-law distribution. However, the power-law itself does not point to any particular physical explanation for intermittency. As put in a recent review of the applications of power-laws in physics, "Perhaps the only thing more abundant in both natural and man-made systems than power laws are the models that have been developed to explain them."[16]

The observation of power-law distributed *on*- and *off*-time durations implies that the rate constants for production and decay of the dark state responsible for PI are not constant, but evolve over the timescale of the measurement. The evolution in rate-constant with time is commonly referred to as "dispersed kinetics". For many single-emitters the observation of dispersed kinetics has been assigned to a variation in charge-transfer rates.[17–21] For example, a distribution of static charge-trapping sites on a quantum dot can provide for a corresponding distribution of trapping rates.[22–24] For organic luminophores variation in the barrier for electron transfer between the luminophore and the surroundings could also provide for this evolution in rates.[25,26] Although the power-law PDF has been widely used in PI analyses, deviations from a power-law distribution have been reported.[26–29] These deviations bring into question the essentially ubiquitous application of power-law. Are there other PDFs that more accurately represent PI data? Can quantitative statistical tests be developed to ascertain the "goodness of fit" of a PDF to a specific data set? To address these questions, we present a new method for the analysis of PI data. Following the methods introduced by Clauset *et al.*, the approach described here relies on maximum likelihood estimation to define the fit parameters for a given PDF to the experimental data.[30] Simulated data are generated with these best fit parameters, and compared

to the original data set allowing for the application of statistical test to quantify the extent to which the PDF represents the measured PI. This method is applied to the PI exhibited by CdSe/CdS core/shell quantum dots (QDs) dispersed in thin films of poly(methyl methacrylate) (PMMA), and to single molecules of violamine R incorporated into potassium acid phthalate (KAP). Surprisingly, we find that *on*- and *off*-event duration distributions are not well described by a power-law.

We also present methods that provide a quantitative determination of whether two data sets arise from the same PDF *without* first assuming a functional form for the PDF itself. The utility of this method is illustrated in a comparison of QD data taken at two excitation powers to determine if a statistically significant change in PI can be detected. This is particularly useful since the current approaches involve a simple comparison of power-law exponents, an analysis that is far from statistically robust. The alternative approach outlined here is also useful for characterizing the heterogeneity of a particular ensemble of emitters, and to determine statistically valid changes in PI in the presence of this heterogeneity. These methods are easily employed and provide a bias free interpretation of PI data. The analysis outlined here is well suited to many studies involving SM nanoprobes in different hosts or environmental conditions, as well as in the fundamental investigations of temperature, power, and excitation wavelength dependence of PI. Other applications may extend to studying the emission statistics of coupled emitters and clustered emitters where current methods have shown ambiguous results.[31]

4.3 Experimental Methods

4.3.1 Sample Preparation

All steps in the CdSe/CdS core/shell quantum dot synthesis were performed under nitrogen. The CdSe core was prepared by a hot injection synthesis with 0.4 mmol of CdO, 1.6 mmol of stearic acid and 20.27 mL of octadecene heated under vacuum

at 100 °C. The solution was purged several times and slowly heated to 250 °C where it was held until the solution became clear. The resultant mixture was cooled to room temperature and 2 g of trioctylphosphine oxide and 1.8 g of hexadecylamine were then added. The solution was degassed and heated to 305 °C where 2 mL of a solution consisting of 2 mmol of Se in 1 mL of trioctylphosphine and 1 mL of octadecene was injected. The solution was cooled to room temperature and washed with ethanol and toluene to isolate the CdSe nanocrystals. The CdS shell was grown on the CdSe crystals by first preparing a cadmium oleate solution consisting of 0.67 mmol of CdO, 0.27 mmol of oleic acid and 4 mL of octadecene at 130 °C degassed for 1 hr. The solution was heated to 280 °C, where it clarified and then the temperature was reduced to 60 °C. Trioctylphosphine sulfide (TOPS) was prepared by combining 2 mmol of S and 3 mL of trioctylphosphine. In a separate flask 1.5 mL of oleylamine and 3 mL of octadecene were degassed and heated to 130 °C for 2 hrs. At 60 °C, half of the CdSe nanocrystals were added, the solution was degassed, and the temperature set to 180 °C. To this solution 0.5 mL of the cadmium oleate solution was added drop wise then stirred for 30 min. Next 0.5 mL of TOPS was added drop wise and stirred for an additional 30 minutes. Finally drop wise additions of 0.75 mL were made alternately of each TOPS and cadmium oleate with 30 min stir times between additions. The temperature was then set to 130 °C and left overnight. The CdSe/CdS nanocrystals were isolated with ethanol and toluene. The absorption spectrum of the nanocrystals had a maximum at 570 nm, and an emission maximum at 583 nm with full width at half maximum of 30 nm. TEM images of the nanocrystals show they are spherical in shape and 4 nm $\pm$ 0.1 in diameter. The absorbance cross-section maximum of the QDs was calculated from the molar absorptivity and estimated to be 5×10^{-16} cm^{-2}. QD samples were prepared by spin casting solutions of 1% wt/vol poly(methyl methacrylate) (PMMA) in tolune doped with $\sim 10^{-9}$ M of QDs onto piranha (ammonium hydroxide and hydrogen peroxide) treated glass coverslips.

Violamine R (VR, 60% pure, Aldrich) was purified as described in the literature

to 95% as determined by LC-MS.[32] Dye-inclusion crystals were grown by slow cooling from 46 °C with a cooling slope of 0.08 °C/hour in a customized water bath. The crystals were grown in sealed crystallization dishes that were completely submerged beneath the water to avoid condensation. KAP crystallization solution was prepared in the crystallization dishes by adding 14.3 g of KAP to 75 mL of nano pure water and bringing to a boil. The solutions were cooled slightly and seeded with cleaved sections of small KAP crystals. The seeds dissolved in the hot liquor to smooth the surface. VR concentration of 10^{-7} M yielded crystals with VR concentrations appropriate for single molecule studies. The crystals were harvested after 3.5 days of growth.

4.3.2 Single Molecule Microscopy

Excitation was provided by a 532-nm laser (Spectra Physics Excelsior), and powers of 0.5 and 8.2 μW were employed as measured at the entrance port to the microscope. The excitation beam was focused using a 1.3 NA objective (Nikon, Plan-Fluor) providing a diffraction-limited spot (250-nm dia) at the sample. The resulting photon flux was approximately 0.14 photons/100 ns and 2.3 photons/100 ns for 0.5 and 8.2 μW excitation power, respectively. Single molecules of VR in KAP were excited with a power of 3.2 μW in the same experimental set up. Samples were mounted on a xy-piezoelectric scan stage (Physik Instrumente). Crystal samples were heated with a custom built heating stage described elsewhere.[20] The single molecule emission was collected using an epi geometry, filtered using a 550-nm long-pass filter to reject the excitation field, focused onto a 70-μm pinhole, and directed onto an avalanche photodiode detector (Perkin Elmer SPCM-AQR-16). Single quantum dot emission traces were collected using 10-ms integration for a total acquisition time of 5 minutes. Emission from individual quantum dots was established based on the diffraction-limited spot size of the fluorescence image, sample dispersion of no more than 1 QD per micron, the complete extinction of fluorescence to the shot noise during off-intervals, and irreversible single-step photobleaching. Additional care was taken to check the

concentration dependence on the density of QDs, with a factor of 2 decrease in concentration resulting in a two-fold reduction in the number of QDs in a given area. The QD data was processed by first setting an emissive threshold to delineate *on*- and *off*-events. QDs have been shown to possess a continuous number of emissive states,[33] making the definition of a single emissive threshold a challenge. Cordones *et al.* have shown that the power-dependence as studied using hard thresholding vs. change point detection analyses yielded similar results for QDs.[34] In this study thresholding was employed due to the computational expense of the change point detection algorithm used in previous studies. A threshold of 3 standard deviations above the RMS noise corresponding to 20 counts per 10 ms at 8.2 μW was employed as the threshold, and used for data obtained with lower excitation power. Thresholds of 6 and 9 standard deviations above the RMS noise were also investigated, and did not significantly change the results derived from the 3 standard deviation analysis (see below). PI data for VR in KAP were analyzed using the change point detection (CPD) algorithm as described previously.[35,36] Deconvolved states with intensities greater than one standard deviation above the RMS noise were designated as *on*. This definition of the emissive threshold designates the lowest deconvolved intensity state(s) as non-emissive or *off*. As discussed previously, a fraction of VR molecules are continually emissive and are not included in the *on*- and *off*-interval histograms. All data analysis was performed in MATLAB (version 2011b).

4.4 Results and Discussion

4.4.1 Current Analysis and Maximum Likelihood Estimation

As described in the introduction, the first step in current analyses of PI data is a determination of *on*- and *off*-interval durations. Typically, a threshold is set above the shot noise, and intensities above (below) this threshold are designated as *on* (*off*). Once the data have been parsed into *on*- and *off*-events, histograms of *on*- and *off*-

event durations are constructed and analyzed. If the processes responsible for PI are well described by first-order kinetics (for example, intersystem crossing to a triplet-state) then the *on*- and *off*-interval histograms will be exponentially distributed. However, in most cases the histograms are not well described by an exponential, exhibiting substantial probability at long-time durations. To assist in the analysis of these long-time events, the discrete histograms are converted to continuous probability distributions using the method first proposed by Kuno *et al.*[37] In this approach, each event is divided by the average time between the two closest events thereby creating a continuous probability distribution. The application of this method to the PI data from CdSe/CdS QDs obtained here is shown in Figure 4.1. The discrete duration histograms are shown in Figure 4.1(a) and (b), and the continuous distributions derived from these histograms are shown in 4.1(c) and (d). The transformation to a continuous probability distribution increases the spread in observed probability resulting in enhanced linearity when the data are viewed on a log-log plot. This enhanced linearity encourages the application of a power-law probability distribution function (PDF) to describe the probability distributions with linear least squares regression used to obtain the best fit of the data to a power-law. Figure 4.1 illustrates the fitting of the PI data from the CdSe/CdS QDs to a power law using this approach. Notice that both the *on*- and *off*-times demonstrate a subtle deviation from the power-law fit, especially at longer durations. An additional issue in this analysis is that linear least squares fitting has been found by multiple groups to underestimate the power-law exponent which is used to connect PI data to underlying physical processes.[13,38]

An alternative method for connecting PI data to a power-law PDF involves maximum log-likelihood estimation (MLE). This approach has been outlined by Hoogenboom *et al.* for the specific case of power-law distributed event durations and applied to synthetic QD data.[38] The operative principle in MLE is that if the hypothesized PDF and corresponding parameter values are correct, then the probability of the data corresponding to that PDF should be maximized.[39] This probability is expressed in

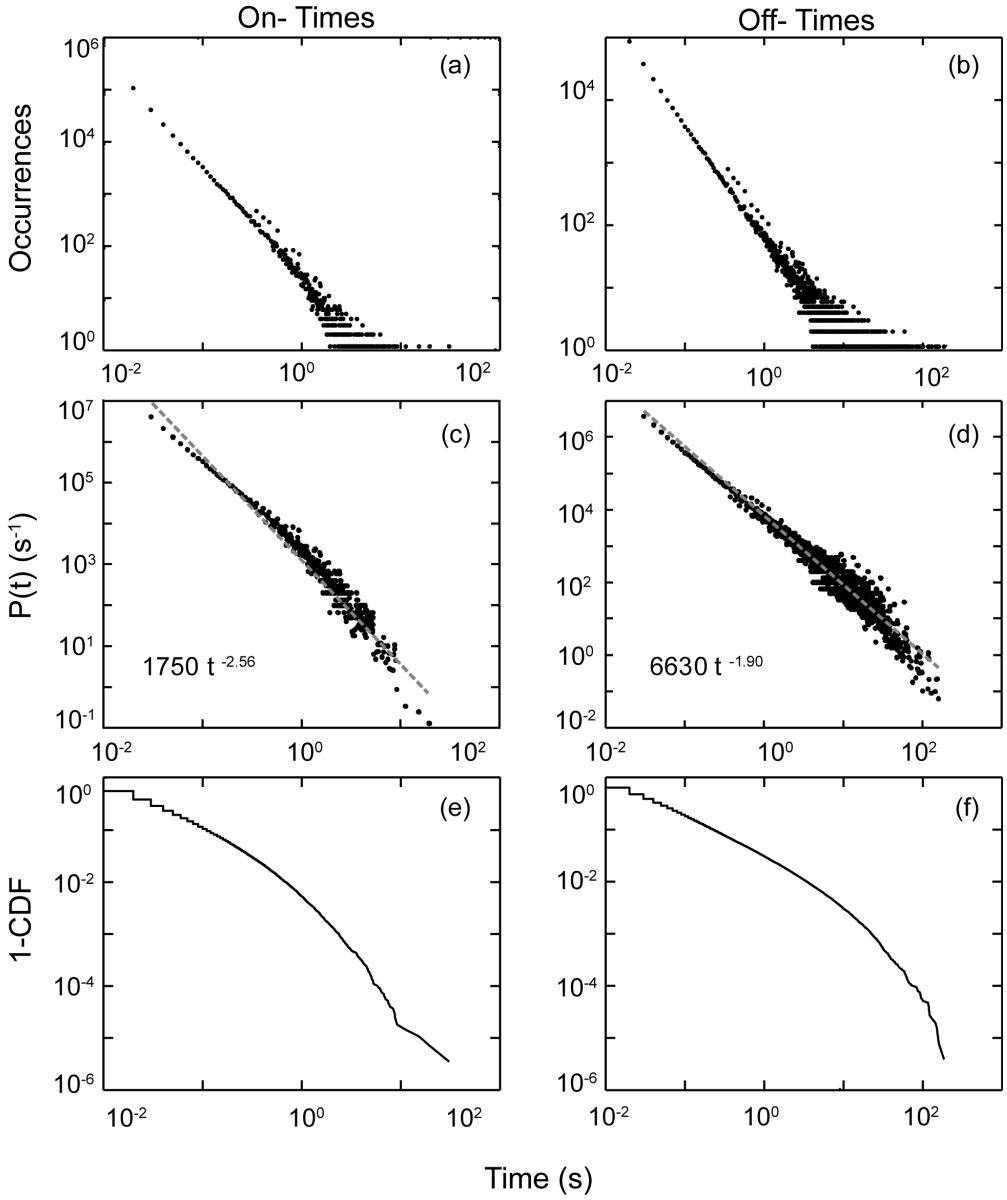

Figure 4.1: *On*- and *off*-event duration histograms for 220 CdSe/CdS QDs in PMMA. (a-b) Raw PI histograms presented on a log-log plot. The tail of the data is fanned, representing sparse events. (c-d) Each point in the raw histogram is divided by the average time to the nearest neighbors, resulting in a continuous probability density. The data in the right are fitted with linear least squares regression to obtain the power-law exponent. (e-f) CDFs generated from the data in (a) and (b), the CDF is a naturally decaying distribution that can be fitted and differentiated to generate the PDF without the need to smooth the data. The curvature of the CDF indicates that the data are not consistent with power-law.

a likelihood function, $\mathcal{L}$, which is the joint probability of the observed data given that the PDF and its parameters are known,

$$\begin{aligned}\mathcal{L}\left(a_1, a_2, \ldots a_m\right) &= f\left(t_1|a_1, a_2, \ldots a_m\right) f\left(t_2|a_1, a_2, \ldots a_m\right) \ldots \times f\left(t_n|a_1, a_2, \ldots a_m\right) \\ &= \prod_{i=1}^{n} f\left(t_i|a_1, a_2, \ldots a_m\right) \end{aligned} \tag{4.1}$$

In the above equation t_i are the data points, and a_n represent the parameters of the PDF. In the case of a power-law PDF, the value of the power-law coefficient that maximizes the likelihood function is the best estimate for the true value of the coefficient,

$$\mathcal{L}\left(\alpha\right) \cong A^n \left[\prod_{i=1}^{n} t_{\mathrm{i}}\right]^{-\alpha} \tag{4.2}$$

The MLE estimate is obtained by differentiating the above expression, setting the derivative equal to zero, and solving for α. Although we have used a power-law PDF to illustrate MLE methods, as long as the likelihood function is differentiable MLE can be employed. In addition, the logarithm transform is commonly used to create a straightforward conversion of products to sums of the likelihood function for ease of computation. This approach has many advantages in analyzing PI data such as ease of use, no binning of the data, and it is an unbiased estimator in the large sample limit (>20).

4.4.2 Cumulative Distribution Functions

The essence of any PI data analysis is determining the probability of observing an event within a given time interval. A related way to express this probability is to ask, "What is the probability of observing an event less than a specified value?" The answer to this question is simply the integral of the PDF up to the time of interest. The cumulative distribution function (CDF) is defined as the probability of an event occurring in a time less than or equal to t, and is related to the integral of the PDF:[39]

$$S\left(t\right) = \int_{t_{min}}^{t} P\left(\tau\right) d\tau \tag{4.3}$$

In the above expression *S(t)* is the CDF and *P(τ)* is the corresponding PDF. The CDF is bound by zero when $t < t_{min}$, and one at the longest observation time. *S(t)* can be computed directly from PI data by employing the correspondence between integrals and sums:

$$S(t) = \frac{1}{N} \sum_{i=1}^{N} 1 \ \{t_i < t\} \tag{4.4}$$

In the above expression t_i is an event duration less than time t, and N is the number of events. This distribution is zero for all times less than t_{min} and one for all times greater than the longest event in the sum. Related to the CDF is the complimentary CDF given by:

$$F(t) = 1 - S(t) \tag{4.5}$$

F(t) is the probability of observing an event at a time greater than t, and is useful for visualizing PI data since the event probabilities are greatest at short times. Figures 4.1(e) and (f) show the complimentary CDFs for the CdSe/CdS QDs described earlier. The most notable feature of the complimentary CDF *is that it is a continually decaying function.* When employing CDFs the PI data do not need additional processing to construct a continuous probability distribution (Figs. 4.1(c) and (d)), greatly simplifying PI data analysis. Because the CDF is directly related to the PDF (Eq. 4.3), the CDF can be constructed and then differentiated to obtain the underlying PDF. For example, since the integral of a power-law is also a power-law, the corresponding CDF has the functional form of a power law and will therefore appear as a straight line on a log-log plot. Any curvature evident in the CDF on a log-log plot is direct evidence that the *on*- and *off*-event durations are not power-law distributed. Figures 4.1(e) and (f) demonstrate that complimentary CDFs for the CdSe/CdS QDs possess curvature over the entire range of times investigated; therefore, the PDF describing these data cannot be a power law.

4.4.3 An Alternative Method for Analyzing PI Data

The alternative approach for analyzing PI data described here is based on the method outlined by Clauset *et al.* for determining if a given data set is described by a power-law.[30] We have adapted this method to the specific case of single molecule PI, and extended the method to arbitrary PDFs. The method involves three basic steps: estimating the best fit parameters for a given PDF, testing to determine the probability that the data are represented by the PDF, and comparing various PDFs to identify the one that best fits the data. Each of these steps is outlined below.

Estimating PDF Best-fit Parameters

To illustrate this method we employ a power law as our example PDF, an extension of this method to other PDFs is provided later. The approach used to identify the best-fit parameters differs slightly from MLE methods described previously in that we also determine both the power-law coefficient (α) and onset-time for the power-law (t_{min}) rather than assuming this value is equal to the time bin used to acquire the PI data. Recall that the power-law PDF is of the form:

$$P(t) = At^{-\alpha} \tag{4.6}$$

In the above expression A is the normalization constant and α is the power-law exponent. The normalization coefficient is determined by integrating *P(t)* from the onset time, t_{min}

$$1 = \int_{t_{min}}^{\infty} P(t')\, dt' \tag{4.7}$$

Integration of the above expression yields the following PDF:

$$P(t) = \frac{\alpha - 1}{t_{min}} \left(\frac{t}{t_{min}} \right)^{-\alpha}, \ \alpha > 1 \tag{4.8}$$

Notice that t_{min} must be finite in order for *P(t)* to be finite. The power-law PDF also has the added complication of being un-normalizable when α is less than one,

which is typically avoided by applying the restriction $\alpha > 1$, or by integrating to a maximum time.

The onset time at which the power-law statistics become operative is usually overlooked when fitting PI data (as is the case in linear least squares approaches described above), or t_{min} is simply set equal to the time of the experiment. To accurately fit the data, it is necessary to determine the best t_{min} so that the data is fit only where the power-law is operative. To obtain this value, we first use MLE to determine α:[30]

$$\alpha = 1 + n \left(\sum_{i=1}^{n} ln \frac{t_i}{t_{min}} \right)^{-1} \tag{4.9}$$

In the above expression n is the sample size and t_i is a given *on*- or *off*-event. To find t_{min}, the scaling parameter is estimated for all possible values of t_{min} starting from the smallest possible value t_{min} can equal to the time resolution of the experiment up to $t_{min} = 0.90 \times t_{max}$ or 90% of the longest time observed. To determine which t_{min} and α pair best fits the data, the difference between the sample CDF (Equation 4.4) and that of the power-law fit is calculated using the Kolomogorov-Smirnov (KS) statistic, D. For example, the CDF for the power-law expression (Equation 4.8) is:

$$S(t)_{fit} = 1 - \left(\frac{t}{t_{min}} \right)^{1-\alpha} \tag{4.10}$$

The KS statistic, D, is defined as:[40]

$$D = max_{-\infty<t<\infty} |S(t)_{fit} - S(t)| \tag{4.11}$$

Equation 4.11 illustrates that D represents the maximum difference between of the two CDF's, and provides a direct measure of how similar the two distributions are. For a perfect fit with no deviation, $D = 0$. Quantitatively, the best fit α and t_{min} pair is defined as that which minimizes D.

Statistically Evaluating PDFs

A statistical test is required to accept or reject the hypothesis that the *on*- and *off*-event duration distributions are consistent with a given PDF. Here, this test is performed using a p-value, defined as the probability of measuring a test statistic at least as extreme as the one observed. The hypothesis that a PDF represents experimental results is then accepted or rejected by comparing the p-value to a significance level. In the analysis outlined here the test statistic is D, defined previously as the maximum deviation between the best fit and experimental CDFs (Eq. 4.11). To determine the p-value, simulated data is generated using the best fit values for the PDF obtained as described earlier. The simulated data sets are then fit in exactly the same manner as the original data, and D_{synth} from these fits is compared to D from the initial fit. It is important to note that D_{synth} is calculated between the synthetic data and the fit to the synthetic data (not the fit to the original data). The fraction of D_{synth} from the simulated data sets equal to or greater than D for the original data is used to calculate the p-value.

Synthetic data sets were created using a "bootstrap method" as illustrated in Figure 4.2. Because the power-law is only operative for $t > t_{min}$, the data less than t_{min} needs to be constructed; however, the functional form of the PDF describing the data for times less than t_{min} is not available. Therefore, simulated data over this early-time interval is obtained by uniform random sampling of the empirical data for times less than t_{min}. To generate data for times equal or greater than t_{min}, random numbers are generated from a power-law distribution employing the best fit parameters. To determine which method is used at any given point in the simulation, a sampling probability is defined as $prob = 1 - (n_{tail}/n)$, where n_{tail} is the number of entries in the original data greater than or equal to t_{min}. If a uniform random number $r < prob$, then the simulated data point (t_s) is generated for the case $t_s < t_{min}$, otherwise t_s is drawn from the power law with the estimated α and t_{min}. The length of the

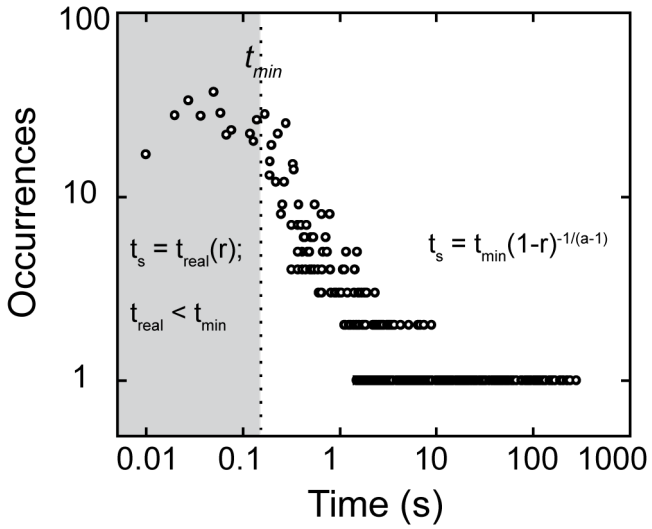

Figure 4.2: An illustration of the process by which simulated data are created. Simulated data sets for the power-law are generated by a uniform sampling of the experimental data below t_{min} with probability $1 - n_{tail}/n$ (shaded region), and randomly from a power-law (or other PDF) employing best fit parameters determined using maximum likelihood estimation with sampling probability n_{tail}/n.

simulated data set is made equal to that of the experimental data set. The random number generator for a power-law is:[30]

$$t_s = t_{min}\left(1-r\right)^{-1/(\alpha-1)} \tag{4.12}$$

In this expression r is a uniformly distributed random number. Each simulated data set is fit exactly as the original data, and D_{synth} is obtained for each simulated data set. The fraction of D_{synth} greater than the D calculated from the experimental data is defined as the p-value,

$$p-\text{value} = \frac{\sum D_{synth} \geq D}{N_s} \tag{4.13}$$

The above equation illustrates that the p-value simply represents the fraction of the simulated data for which D_{synth} is larger than that of the original data. The accuracy of the p-value increases with the number of simulated data sets (N_s) as $1/2\sqrt{N_s}$. To obtain an accuracy of 0.005, simulations were run with 10^4 synthetic sets. A p-value of < 0.05 rejects the hypothesis that the PDF is consistent with the data to 95% confidence interval.

Extension to Other PDFs

In addition to the power-law, there are many other PDFs whose tails are not exponentially bounded (so called "heavy tailed") that may be consistent with PI data. These PDFs include Weibull, lognormal, Generalized Pareto, Beta, Kappa, inverse Gaussian, etc., and it is necessary to explore these PDFs in describing PI data. Here, we fit our PI data to both Weibull and lognormal PDFs since these represent more generalized classes of "heavy-tailed" PDFs.[40] The methods described above were used for these alternative distributions, with best fit parameters determined based on MLE methods for these distributions. The Weibull distribution and corresponding CDF are given by:

$$P\left(t\right) = \frac{A}{\beta}\left(\frac{t}{\beta}\right)^{A-1} e^{-\left(\frac{t}{\beta}\right)^{A}},\ \text{t} > 0, \tag{4.14}$$

$$S(t) = 1 - e^{-\left(\frac{t}{\beta}\right)^{A}} \tag{4.15}$$

Inspection of the above equations reveals that the Weibull distribution is essentially the product of a power-law and a stretched exponential function. Press *et al.* describe the Weibull as a generalization of the exponential distribution that is useful in reliability analysis.[40] This branch of statistics investigates properties such as the time to failure of mechanical systems, or death in biological organisms. With respect to PI, one can think of the duration or "survival" of each *on*- or *off*-intervals. For simple first-order kinetic decay there is a constant probability per unit time for the decay of the emissive state. Dispersed kinetics can be thought of as statistical aging of the system where the probabilities for *on*- and *off*- interval durations change with time. The Weibull distribution incorporates statistical aging through the parameter A where $A > 1$ corresponds to the case where the probability that the molecule will leave a particular emissive state increases with time, and $A < 1$ is the opposite case. This distribution was found to best describe the durations of intensity segments in single molecules of 2',7'-difluorofluorescein overgrown in crystals of potassium acid phthalate which possessed unusually stable emissive states (in preparation).

The standard lognormal distribution and corresponding CDF are given by

$$P(t) = \frac{1}{\sqrt{2\pi}\sigma t} e^{\left(-\frac{1}{2}\left[\frac{log(t)-\mu}{\sigma}\right]^2\right)},\ \mathrm{t} > 0, \tag{4.16}$$

$$S(t) = \frac{1}{2}\ \mathrm{erfc}\left(-\frac{1}{\sqrt{2}}\left[\frac{log(t)-\mu}{\sigma}\right]\right) \tag{4.17}$$

The lognormal distribution occurs when the logarithm of the sampled variable is Gaussian distributed. Lognormal distributions arise in processes well described by multiplicative random walk models.[41,42] Examples include one dimensional diffusion of a particle in the presence of randomly distributed traps,[43] and also the diffusion in the presence of random local electric fields.[44] Physical processes that these models have been applied to include the migration of excitons in mixed organic crystal lattices and in diffusion controlled reactions.[43] These models typically have both lognormal and

power-law regimes, demonstrating that the functions are closely related in physical systems. A consequence of the multiplicative processes that give rise to lognormal distributions is that the operative photophysical processes must be non-Markovian; therefore, "memory" is expected to be observed in systems where PI is described by a lognormal distribution.

The results of fitting the CdSe/CdS and VR/KAP PI data to Weibull and lognormal PDFs are presented in Figures 4.3 and 4.4, respectively. The left-hand side of Figure 4.3 shows the best fits for *on*- and *off*-intervals of the QD data obtained using 0.5 μW excitation. Notice that the data are not well represented by any of the PDFs investigated, with the widely employed power-law PDF providing the worst fit to the data. The second column shows data derived from a single quantum dot. Again these data are also not represented by any of the PDFs investigated. In contrast, Figure 4.4 shows data from single molecules of VR embedded in KAP crystals at room temperature and at 60 °C. The data is not well represented by power-law; however at 60 °C the *on*-intervals are in excellent agreement with the lognormal fit corresponding to a p-value of 0.13 and the *off*-intervals also being close to lognormal.

4.4.4 Comparing PI Data Sets Without PDFs

Here we present an extension of our analysis method for determining whether or not the underlying PDF changes with experimental conditions *without* assuming a functional form for the PDF. The approach presented here can also be used to quantify heterogeneity within a SM ensemble, and to determine statistically significant differences between heterogeneous sample sets. The example data that we will use to describe this method is the excitation-power dependence of the *on*- and *off*-event duration distributions observed for CdSe/CdS quantum dots.

The test statistic, D, described above is distributed according to another PDF called the Kolomogorov-Smirnov (KS) distribution. The KS-distribution is important for application of the statistical test; however, the PDF for the KS-distribution

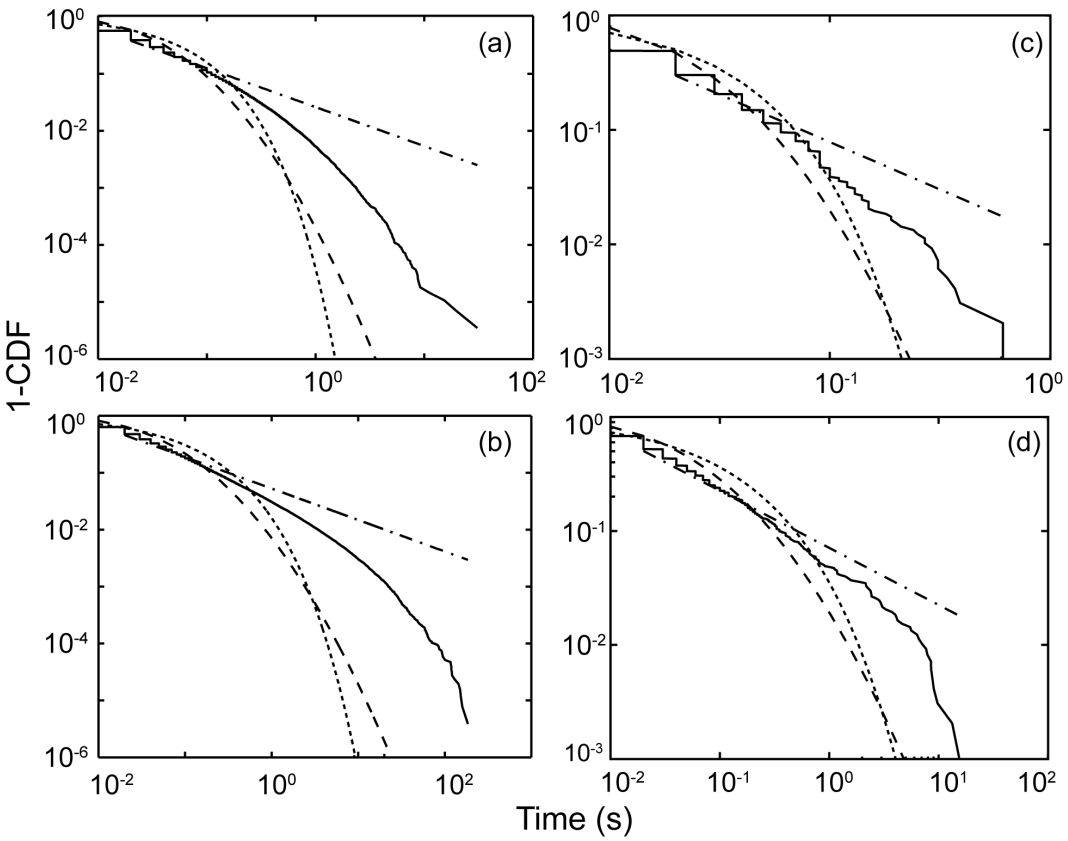

Figure 4.3: Left: Best fits of the 0.5 μW data to power-law(-··-), lognormal(-) and Weibull(·) PDFs for 220 CdSe/CdS quantum dots in PMMA for *on*-times (a) and *off*-times (b). None of the PDFs represent the data, with all fits rejected having p-values < 0.0001 (derived from 10,000 simulated data sets as described in the text). For power-law best fit t_{min} was 0.01 for both *on* and *off* with $\alpha = 1.55$ (*off*) and 1.67 (*on*) Right: Identical analysis applied to the PI data derived from a single CdSe/CdS quantum dot *on*-times (c) and *off*-times (d). The single QD data also fails the statistical test for all three distributions to 0.01. This was performed for all QDs at 0.5 μW, not a single QD (*on* or *off*) was represented by these functions.

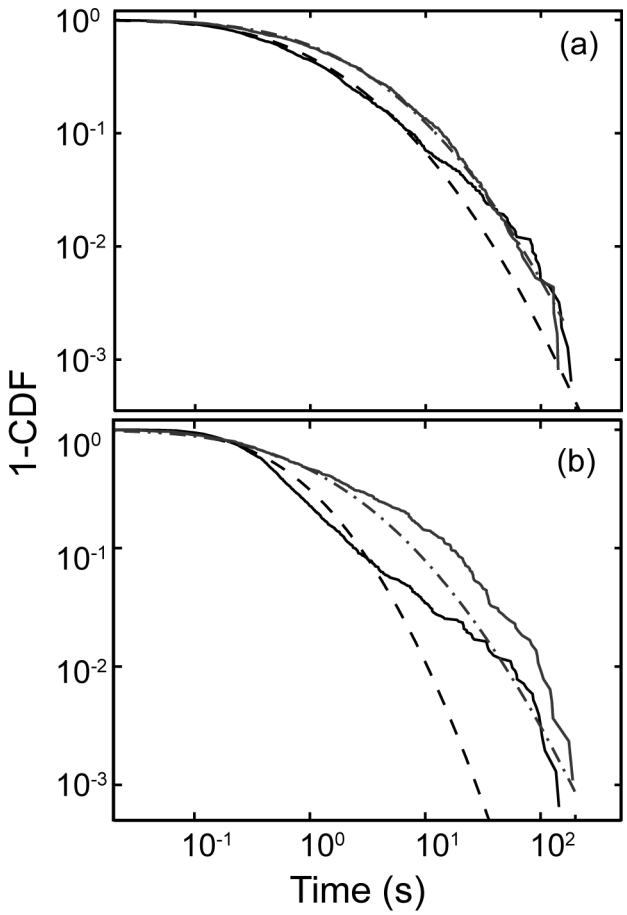

Figure 4.4: Complimentary CDFs for the *on*- (a) and *off*- (b) times observed VR-KAP at room temperature (black) and 60 °C (gray). Best fits to lognormal functions are overlaid on the data (dashed lines). *On*-interval data becomes strongly lognormal at 60 °C (p-value increases from 0.024 to 0.118), but the room temperature tail diverges from the fit. *Off*-interval data is not well fit to lognormal at either temperature (p-values of 10^{-4} and 0.035 for room temperature and 60 °C respectively).

never explicitly enters into the test. Instead, the CDF of the KS-distribution is determined and used to calculate a p-value for a given D determined from the CDF's of two different samples. This is known as the "two sample KS-test", and is commonly used in other applications to determine the probability that two datasets arise from the same underlying PDF.[40,45] Previously, D was employed as a minimization tool for determining best fit parameters. Here, D is used to compare two different sample CDF's as follows:

$$D = max_{-\infty<t<\infty}|S_1(t) - S_2(t)| \tag{4.18}$$

The left panel of Figure 4.5 shows the complimentary CDFs derived from the the CdSe/CdS intermittency data obtained with 0.5 μW and 8.2 μW excitation. To quantify the differences observed between the two CDF's, the p-value is computed from the CDF of the KS distribution, S_{KS}. The CDF is used because all points in the CDF correspond to an integrated area of the PDF, and thus providing the probability of a measured D value. The p-value is calculated as follows:[40]

$$p - \text{value} = S_{KS}\left(\left[\sqrt{N_e} + 0.12 + 0.11/\sqrt{N_e}\right]D\right), \tag{4.19}$$

where S_{KS} is given by:

$$S_{KS}(z) = \sqrt{\frac{2\pi}{z}}\sum_{j=1}^{\infty} exp\left(\frac{-(2j-1)^2\pi^2}{8z^2}\right) \tag{4.20}$$

Additionally, N_e is the reduced data density which accounts for differences in the number of data points for the two CDF's, and is calculated as follows:

$$N_e = \frac{N_1 N_2}{N_1 + N_2} \tag{4.21}$$

The p-value defined using this approach becomes increasingly accurate as the number of points in a data set increases. PI data were obtained for 220 CdSe/CdS quantum dots under identical experimental conditions. The data were randomly assigned to two separate ensembles of 110 dots, and p-values were calculated for the *on*- and *off*-

intervals derived from these two data sets. The randomized partition of the data into two subgroups was repeated 1000 times, and only 35% of the combinations resulted in p-values > 0.05 for the *on*-intervals, and only 40% for the *off*-intervals. That is, the majority of comparisons found that the data are not described by the same PDF, and illustrates one of the main difficulties in analyzing limited data sets obtained from heterogeneous ensembles of single emitters. One reason for this result is that each CDF is comprised of about 90,000 data points, which demands small values for D for the data to be considered consistent with the same PDF. Figure 4.5 (right panel) shows the histograms of D values obtained in this analysis. The shaded regions in the histograms represent D values which correspond to p-values > 0.05 supporting the hypothesis that two data sets are derived from the same PDF. Clearly, enough sample heterogeneity exists such that one needs to be careful about using a p-value alone from two CDF's to evaluate the hypothesis that the data sets arise from the same PDF. To quantify the difference between the two excitation powers employed in the PI measurements of CdSe/CdS (left panel, Figure 4.5), the D histograms were fit to lognormal distributions and the probability of observing a D value as extreme as the one found between the CDFs at two powers was determined. When comparing 110 QDs at 0.5 μW to 110 QDs at 8.2 μW (see Figure 4.2), D values of 0.0397 (*on*-events) and 0.073 (*off*-events) were obtained. Integrating the tail of the normalized lognormal PDF gives 0.36% (*on*-times) and 0.001% (*off*-times) probability that they could be the same, demonstrating a power-dependence for both *on*- and *off*-times.

The choice of threshold can affect the interpretation of PI data, especially for QD PI which exhibits a continuous distribution of intensity levels.[46] As the threshold is increased, the low-lying emissive states can be excluded from the *on*-time events. The effect of threshold was investigated as shown in Figure 4.6 where thresholds of 3, 6 and 9 standard deviations above RMS noise are used to designate *on*- and *off*- times. The D values computed between the 3 and 9 standard deviations are 0.0153 (*on*) and 0.0378 (*off*), demonstrating that employing these two very different threshold values,

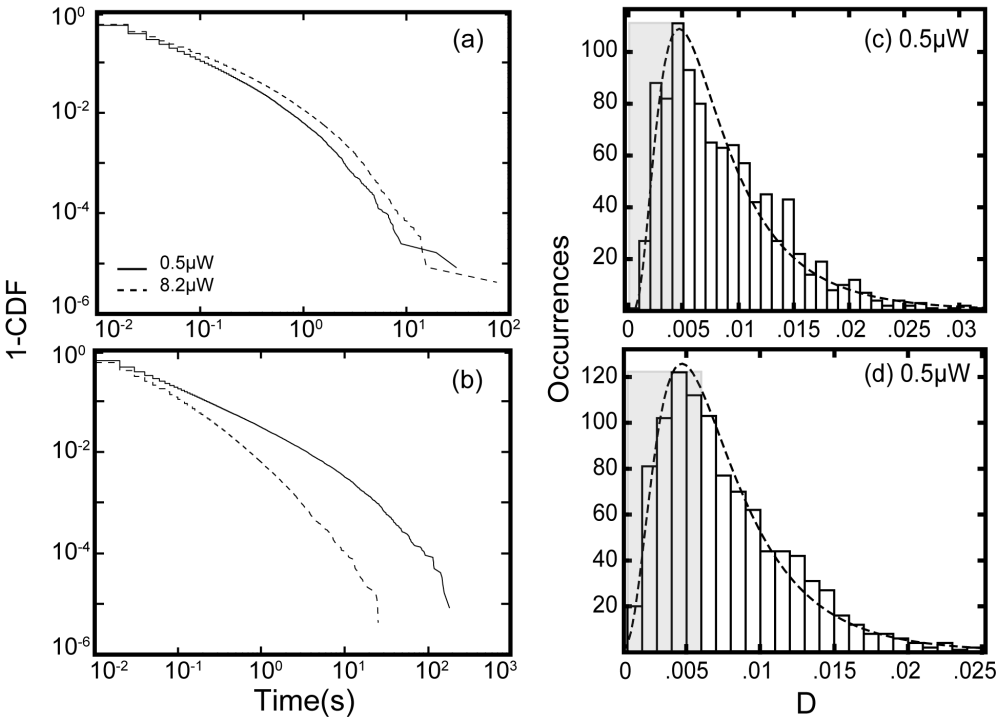

Figure 4.5: Left: Complimentary CDF's on log-log axes for CdSe/CdS QDs *on*- (a) and *off*- (b) times for data taken using 0.5 μW (solid line) and 8.2 μW (dashed line). 110 QDs are used at each power. D values are 0.0397 (*on*-times) and 0.073 (*off*-times). Right: Control study for determining the distribution of observed D values for CdSe/CdS QDs in PMMA with 0.5 μW excitation at 532 nm. The data from 220 CdSe/CdS quantum dots were randomly parsed into two sets and the CDF's for the *on*- (c) and *off*- (d) times were determined and D value computed. The above histogram represents 1000 random trials. The shaded box indicates D values corresponding to p-values that accept the hypothesis that the two distributions are the same. Notice that 60-65% of the time this hypothesis fails. The dashed line represents a lognormal fit to the data. Integrating the tail of the normalized lognormal PDF greater than D obtained from the two power comparison gives 0.36% (*on*-times) and 0.001% (*off*-times) probability that they could be the same, demonstrating a power-dependence for both *on*- and *off*-times.

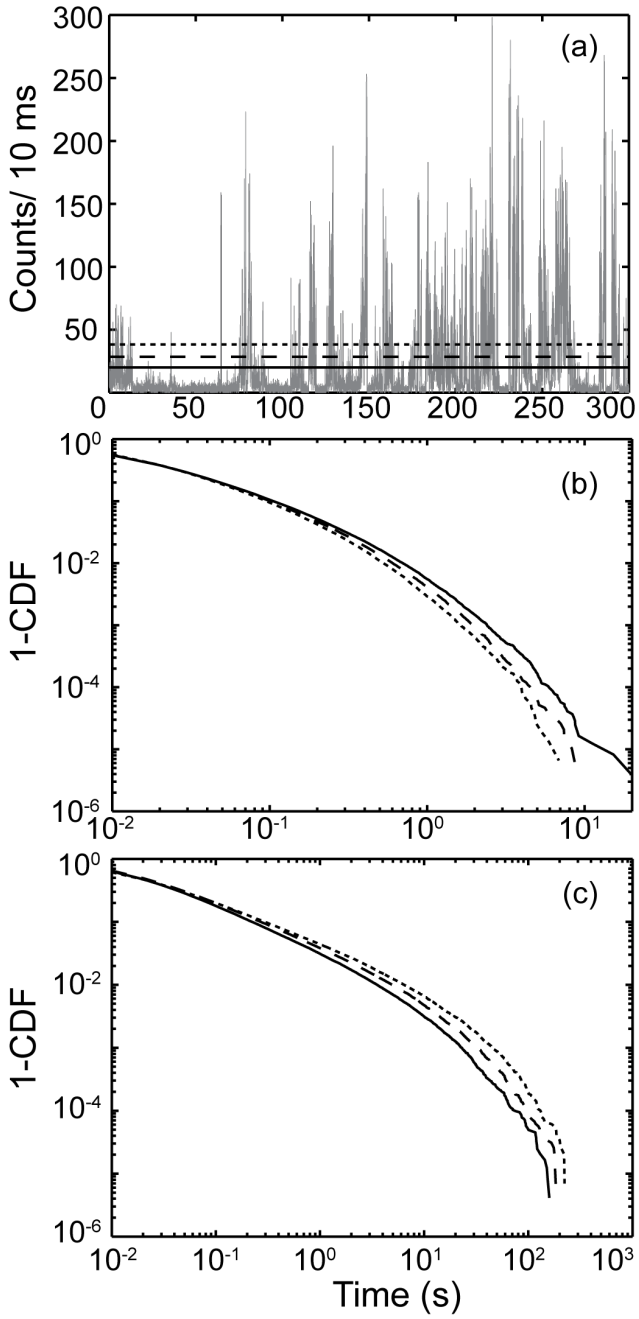

Figure 4.6: 0.5 μW QD CDF's for different thresholds of 3 (solid), 6 (dashed), 9 (dotted) standard deviations above RMS noise depicted in (a). *On*-times (b) show a faster fall off in probability at long-times with increased threshold. D value of 0.0153 between the thresholds of 3 and 9. The opposite is observed in the *off*-times (c), where D is 0.0378 between the thresholds of 3 and 9 standard deviations.

the power-dependence observed in Figure 4.5 remains differentiable.

To further characterize the heterogeneity within the quantum ensembles, CDF's for each individual quantum dot were determined and compared to all others studied. A similar analysis was performed previously for CdSe nanocrystals by Brokmann *et al.*[45] The results of this analysis for the two excitation powers employed in this study are shown in Figure 4.7. The figure illustrates that while the spread in D-values narrows with higher excitation power, the number of p-values > 0.05 decreases slightly. This is due to shorter *off*-event durations at the higher power arising from more transitions between intensity states. The narrowing of the distributions indicates that as *on*- and *off*-event durations decrease, the QDs become less distinguishable on the timescale of the experiment.

The KS statistic is a much more insightful measure of the true degree of heterogeneity than the mean or standard deviation of the *on*- and *off*-time durations for individual quantum dots, a point that is illustrated in Figure 4.7. While it is generally observed that for distributed data the first moments are not sufficient to uniquely define the distribution, the reason for this is very apparent when analyzing individual QDs. Figure 4.8 shows a histogram of the means (left column) and standard deviations (right column) for the CdSe/CdS QDs. The means are narrowly distributed, while the standard deviations demonstrate a modest spread in value. Inspection of Figure 4.7 suggests that the mean and standard deviation should vary little with QD. If the mean and standard deviation are used as test statistics to compare the ensembles of QDs the test passes 97% of the time, far different results than what was obtained earlier. This illustrates the effectiveness of the test statistic D in making quantitative comparisons between datasets. We would also mention again that CDF's are simply calculated and require minimal computational effort, yet they are a powerful tool for detecting differences within both distributed data and heterogeneous sample sets.

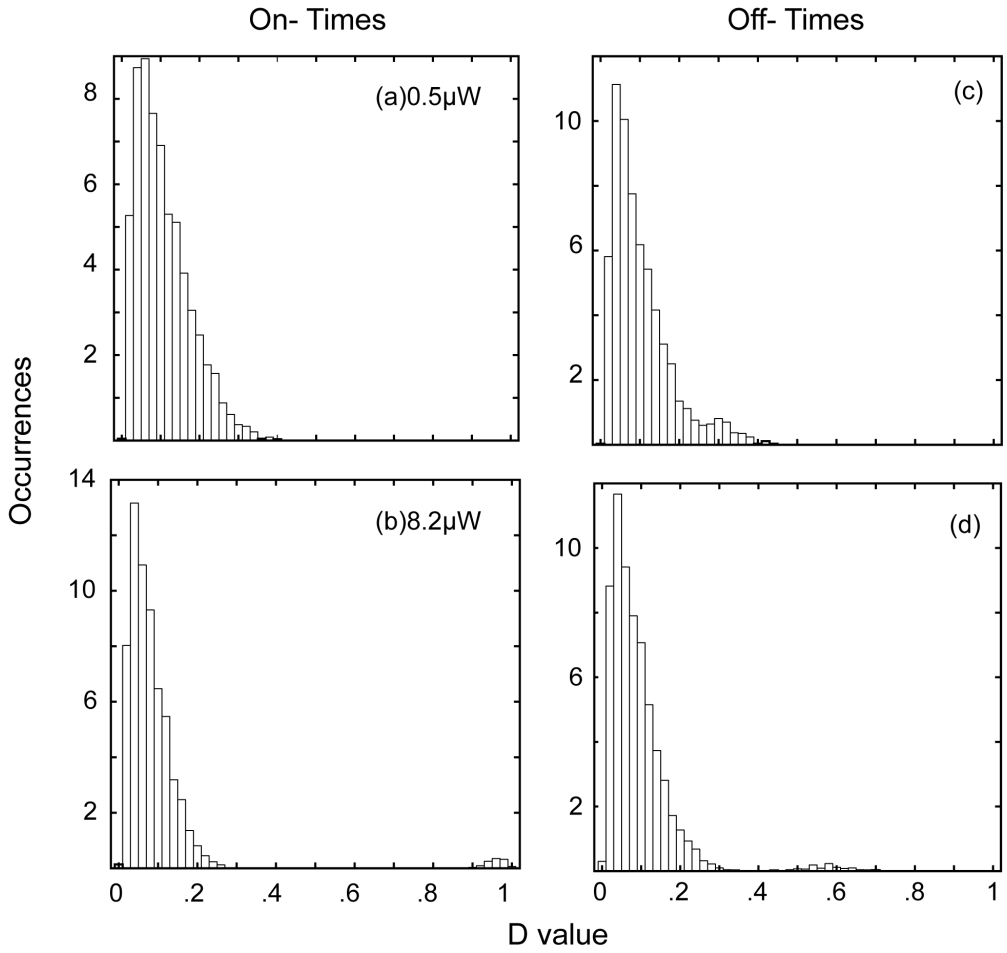

Figure 4.7: D values observed at 0.5 and 8.2 μW between individual quantum QDs within their own ensembles. The *on*- (a, b) and *off*- (c,d) times become more homogeneous with increasing power (the distributions of D shift toward 0). These histograms correspond to the p-value being accepted 41% (*off*, c) and 33% (*on*, a) for 0.5 μW, and 29% (*off*, d) 22% (*on*, b) at 8.2 μW, consistent with a decrease in the *off*-times resulting in more switches.

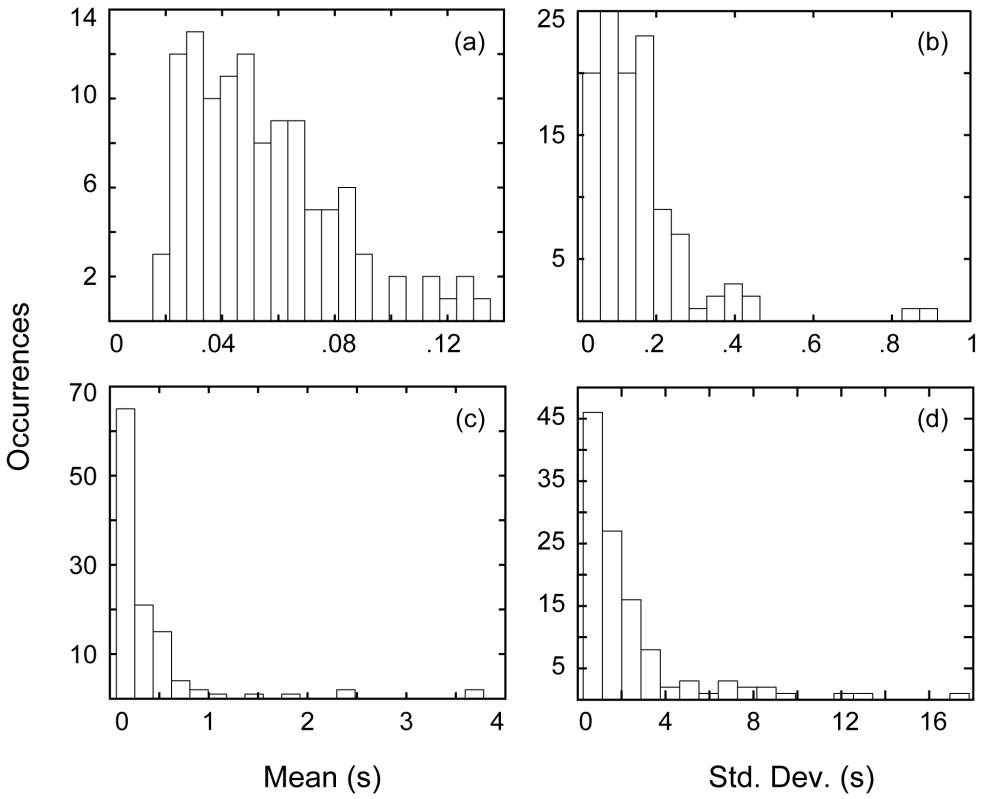

Figure 4.8: The mean and standard deviations of the *on*- (a,b) and *off*- (c,d) intervals computed for the 0.5 μW data. These data illustrate just how difficult it is to judge how similar the QDs are. When the KS test is used on either of these distributions in a simulation like that used on the ensemble CDF's the distributions are considered the same 93% of the time. This illustrates that for the case of distributed data the mean and standard deviation are not reliable methods for capturing the degree of heterogeneity in the ensemble.

4.5 Conclusion

While dispersed kinetics has been evident in the PI of single emitters for years, consensus regarding the underlying photophysical mechanisms has not been achieved for most emitters. In addition, attempts to detect changes in experimental conditions using PI data have been limited due to analysis techniques that frequently rely on comparing power-law exponents. Large variations in power-law exponents due to analysis techniques alone (our QD *on*-time data using linear least squares gave a power-law exponent of 2.56 compared to 1.67 using MLE) place significant restraints on any comparison of power-law exponents. The results presented here demonstrate that power-law distributions do not describe the PI exhibited by the CdSe/CdS QDs deposited in thin films of PMMA or for single VR overgrown in KAP crystals. Instead, alternative PDFs were explored for the VR in KAP data. More importantly, to the authors' knowledge this is the first report of the use of a hypothesis test to determine the accuracy of a PDF in describing PI data. This analysis outlined here provides a more statistically-robust approach for analyzing PI data. We also presented a simple analyses technique to compare PI data associated with an experimental perturbation of the system without the need to define a PDF first. For example, by comparing CDF's with the KS test, the power-dependence in PI of QDs was quantitatively verified, even in the presence of heterogeneity within the small ensemble of single QDs. This method precludes the need to determine the PDF as the first step in analyzing the *on*- and *off*- times of PI. It is also a useful means to characterize the heterogeneity within an ensemble to ensure adequate statistics have been acquired for a particular sample set. Future work will focus on determining fitting procedures for PDFs for which MLE cannot be derived, such as power-law with an exponential cut-off. Our initial studies suggest that this distribution does not fit the PI data observed here from CdSe/CdS quantum dots. It is our hope that the analysis methods presented herein serve as a new starting point for exploring the mechanisms responsible for PI.

4.6 Acknowledgements

This work was supported by the National Science Foundation (NSF)(Grant No. DMR 1005819). Part of this work was conducted at the University of Washington NanoTech User Facility, a member of the NSF National Nanotechnology Infrastructure Network (NNIN).

4.7 Bibliography

[1] Kulzer, F., Xia, T., & Orrit, M. (2010). *Angewandte Chemie International Edition* **49**, 854–866.

[2] Wustholz, K.L., Sluss, D.R., Kahr, B., & Reid, P.J. (2008). *International Reviews in Physical Chemistry* **27**, 167–200.

[3] Vallée, R.A., Marsal, P., Braeken, E., Habuchi, S., De Schryver, F.C., Van der Auweraer, M., Beljonne, D., & Hofkens, J. (2005). *Journal of the American Chemical Society* **127**, 12011–12020.

[4] Li, G.W. & Xie, X.S. (2011). *Nature* **475**, 308–315.

[5] Haase, M., Hübner, C.G., Nolde, F., Müllen, K., & Basché, T. (2011). *Physical Chemistry Chemical Physics* **13**, 1776–1785.

[6] Galland, C., Ghosh, Y., Steinbrück, A., Sykora, M., Hollingsworth, J.A., Klimov, V.I., & Htoon, H. (2011). *Nature* **479**, 203–207.

[7] Califano, M. (2011). *The Journal of Physical Chemistry C* **115**, 18051–18054.

[8] Amecke, N. & Cichos, F. (2011). *Journal of Luminescence* **131**, 375–378.

[9] Plakhotnik, T., Fernée, M.J., Littleton, B., Rubinsztein-Dunlop, H., Potzner, C., & Mulvaney, P. (2010). *Physical Review Letters* **105**, 167402.

[10] Bott, E.D., Riley, E.A., Kahr, B., & Reid, P.J. (2010). *The Journal of Physical Chemistry A* **114**, 7331–7337.

[11] Ambrose, W., Basché, T., & Moerner, W. (1991). *The Journal of Chemical Physics* **95**, 7150–7163.

[12] Knappenberger Jr, K.L., Wong, D.B., Xu, W., Schwartzberg, A.M., Wolcott, A., Zhang, J.Z., & Leone, S.R. (2008). *ACS Nano* **2**, 2143–2153.

[13] Fomenko, V. & Nesbitt, D.J. (2008). *Nano Letters* **8**, 287–293.

[14] Barbon, A., Bott, E.D., Brustolon, M., Fabris, M., Kahr, B., Kaminsky, W., Reid, P.J., Wong, S.M., Wustholz, K.L., & Zanré, R. (2009). *Journal of the American Chemical Society* **131**, 11548–11557.

[15] Frantsuzov, P., Kuno, M., Janko, B., & Marcus, R.A. (2008). *Nature Physics* **4**, 519–522.

[16] Adamic, L. (2011). *Nature* **474**, 164–165.

[17] Cichos, F., Von Borczyskowski, C., & Orrit, M. (2007). *Current Opinion in Colloid & Interface Science* **12**, 272–284.

[18] Kuno, M., Fromm, D., Johnson, S., Gallagher, A., & Nesbitt, D. (2003). *Physical Review B* **67**, 125304.

[19] Schirra, L.K., Tackett, B.S., Blumenfeld, M.L., & Monti, O.L. (2009). *The Journal of Chemical Physics* **131**, 124702.

[20] Riley, E.A., Bingham, C., Bott, E.D., Kahr, B., & Reid, P.J. (2011). *Physical Chemistry Chemical Physics* **13**, 1879–1887.

[21] Sher, P., Smith, J., Dalgarno, P., Warburton, R., Chen, X., Dobson, P., Daniels, S., Pickett, N., & O'Brien, P. (2008). *Applied Physics Letters* **92**, 101111.

[22] Verberk, R., van Oijen, A.M., & Orrit, M. (2002). *Physical Review B* **66**, 233202.

[23] Park, S.J., Link, S., Miller, W.L., Gesquiere, A., & Barbara, P.F. (2007). *Chemical Physics* **341**, 169–174.

[24] Cordones, A.A., Bixby, T.J., & Leone, S.R. (2011). *Nano Letters* **11**, 3366–3369.

[25] Orrit, M. (2010). *Photochemical & Photobiological Sciences* **9**, 637–642.

[26] Tang, J. & Marcus, R. (2005). *The Journal of Chemical Physics* **123**, 054704.

[27] Wang, S., Querner, C., Emmons, T., Drndic, M., & Crouch, C.H. (2006). *The Journal of Physical Chemistry B* **110**, 23221–23227.

[28] Clifford, J.N., Bell, T.D., Tinnefeld, P., Heilemann, M., Melnikov, S.M., Hotta, J., Sliwa, M., Dedecker, P., Sauer, M., Hofkens, J., & Yeow, E.K.L. (2007). *The Journal of Physical Chemistry B* **111**, 6987–6991.

[29] Ko, H., Yuan, C., Lin, S., & Tang, J. (2010). *Applied Physics Letters* **96**, 012104.

[30] Clauset, A., Shalizi, C.R., & Newman, M.E. (2009). *SIAM Review* **51**, 661–703.

[31] Wang, S., Querner, C., Fischbein, M.D., Willis, L., Novikov, D.S., Crouch, C.H., & Drndic, M. (2008). *Nano Letters* **8**, 4020–4026.

[32] Tredwell, C.J. & Osborne, A.D. (1980). *Journal of the Chemical Society, Faraday Transactions 2: Molecular and Chemical Physics* **76**, 1627–1637.

[33] Zhang, K., Chang, H., Fu, A., Alivisatos, A.P., & Yang, H. (2006). *Nano Letters* **6**, 843–847.

[34] Cordones, A.A., Bixby, T.J., & Leone, S.R. (2011). *The Journal of Physical Chemistry C* **115**, 6341–6349.

[35] Wustholz, K.L., Bott, E.D., Kahr, B., & Reid, P.J. (2008). *The Journal of Physical Chemistry C* **112**, 7877–7885.

[36] Watkins, L.P. & Yang, H. (2005). *The Journal of Physical Chemistry B* **109**, 617–628.

[37] Kuno, M., Fromm, D., Hamann, H., Gallagher, A., & Nesbitt, D. (2001). *The Journal of Chemical Physics* **115**, 1028–1040.

[38] Hoogenboom, J.P., den Otter, W.K., & Offerhaus, H.L. (2006). *The Journal of Chemical Physics* **125**, 204713.

[39] Cowan, G. (1998). *Statistical Data Analysis.* Oxford University Press.

[40] Press, W.H., Teukolsky, S.A., Vetterling, W.T., & Flannery, B.P. (2007). *Numerical Recipes: the Art of Scientific Computing. 3rd.* New York: Cambridge University Press.

[41] Limpert, E., Stahel, W.A., & Abbt, M. (2001). *BioScience* **51**, 341–352.

[42] Redner, S. (1990). *American Journal of Physics* **58**, 267–273.

[43] Giacometti, A. & Maritan, A. (1994). *Physical Review E* **49**, 227.

[44] Havlin, S. (1990). *Journal of Statistical Physics* **58**, 653–668.

[45] Brokmann, X., Hermier, J.P., Messin, G., Desbiolles, P., Bouchaud, J.P., & Dahan, M. (2003). *Physical Review Letters* **90**, 120601.

[46] Crouch, C.H., Sauter, O., Wu, X., Purcell, R., Querner, C., Drndic, M., & Pelton, M. (2010). *Nano Letters* **10**, 1692–1698.

Chapter 5

DIELECTRIC DEPENDENCE OF SINGLE MOLECULE PHOTOLUMINESCENCE INTERMITTENCY: NILE RED IN POLY(VINYLIDENE FLUORIDE)

Chelsea M. Hess, Erin A. Riley, and Philip J. Reid

Department of Chemistry, University of Washington, Box 351700, Seattle, WA 98195, United States

Reproduced with permission from Hess, C.M.; Riley, E.A.; Reid, P.J., *The Journal of Physical Chemistry B* **2014**, *118*, 8905-8913.

5.1 Abstract

The dependence of single molecule photoluminescence intermittency (PI) or "blinking" on local dielectric constant (ε) is examined for nile red (NR) in thin films of poly(vinylidene fluoride) (PVDF). In previous studies, variation of the local dielectric constant was accomplished by studying luminophores in chemically and structurally different hosts. In contrast, the NR/PVDF guest-host pair allows for the investigation of PI as a function of ε while keeping the chemical composition of both the luminophore and host unchanged. The solvatochromic properties of NR are used to measure the local ε, while fluctuations in NR emission intensity over time provide a measure of the PI. PVDF is an ideal host for this study since it provides submicron-sized dielectric domains that vary from non-polar ($\varepsilon \approx 2$) to very polar ($\varepsilon \approx 70$). The results presented here demonstrate that local dielectric environment can have a pronounced effect on PI. We find that the NR emissive events increase 5-fold with an increase in ε from 2.2 to 74. A complex dependence on ε is also observed for NR non-emissive event durations, initially increasing as ε increases from 2.2 to 3.4, but decreasing in duration with further increase in ε. The variation in emissive-event durations with ε is reproduced using a photoinduced electron-transfer model involving electron transfer from NR to PVDF. In addition, an increase in NR photostability with an increase in ε is observed suggesting that the dielectric environment plays an important role defining the photostability of NR in PVDF.

5.2 Introduction

Single molecule (SM) spectroscopic techniques are routinely used to study the structure and dynamics of complex materials.[1–4] A current challenge in SM spectroscopy is identifying the guest-host interactions that influence SM phenomena such as photoluminescence intermittency (PI). Investigations of PI generally involve measuring the distributions of emissive (*on*) and non-emissive (*off*) event durations under different environmental conditions, and correlating changes in environment with changes in these distributions.[2,5] Emissive and non-emissive event durations can often span multiple decades in time, and are often assumed to be power-law distributed, although these claims are now under dispute.[6–10] Nevertheless, power-law distributions (and their distributional relatives) can arise when the rate constants for populating and depopulating a non-emissive or "dark" state evolve over the course of the measurement.[7]

For organic luminophores, a common model for dark-state formation is the production of the radical form of the luminophore through photoinduced electron transfer to the surrounding environment. In this model for PI, a distribution of electron transfer sites or energy barriers is presumed to exist within the host, providing for a corresponding distribution of electron transfer rate constants.[3,7,11,12] Also inherent in this model for PI is the expectation that the electron transfer rate constant will depend on the local dielectric constant (ε).[13] The relationship between ε and PI has been explored by others, who proposed that an increase in host dielectric constant serves to stabilize the charge-separated state resulting in prolonged non-emissive event durations. For single terrylene molecules[14] as well as semiconducting nanocrystals[15] the non-emissive event duration distributions shift to longer times with increased ε, consistent with electron transfer being responsible for the PI exhibited by these emitters.

Recently, there has been renewed interest in exploring the relationship between

PI and ε for semiconductor nanocrystals.[16] However, a complicating issue with these studies is that variation in ε was accomplished by changing the chemical composition of the host including their fundamental solvation properties.[14,15] In our recent study of nile red (NR) in poly(vinylidene fluoride) (PVDF) we found that polymer films expressed in the ferroelectric β-phase consist of a wide distribution of dielectric environments ranging from $\varepsilon \approx 2$ to 70.[17] Using the solvatochromic shift of NR, which extends from 520 nm in hexane ($\varepsilon = 1.88$) to 614 nm in acetonitrile ($\varepsilon = 37.5$), we were able to spatially map the dielectric environments of PVDF with domains sizes ranging from a few hundred nanometers to microns in diameter.[18] This finding suggests that the NR/PVDF guest-host system provides a novel opportunity to investigate the dependence of PI on local environment without varying the chemical composition of the luminophore or host.

Here we present a study where both the intensity and emission energy from single NR molecules is measured as a function of time allowing for the simultaneous measurement of PI and the local dielectric constant of the environment. We find that for NR in PVDF the median emissive event durations increase 5-fold with an increase in ε from 2.2 to 74. A more complex dependence on ε is observed for NR non-emissive event durations, with the median non-emissive event duration initially increasing as ε increases from 2.2 to 3.4, but then decreasing in duration as ε continues to increase. Employing the photophysical properties of NR and PVDF, we have constructed a simple model for the photoinduced electron transfer between NR and PVDF. Using this model the variation in emissive-event durations with ε is reproduced. In addition, the photostability of NR increases with ε suggesting that the local dielectric environment plays an important role defining the photostability of NR in PVDF.

5.3 Experimental

5.3.1 Sample Preparation

Thin films of nile red (NR, Aldrich, 99+% pure by LC-MS) embedded in poly(vinylidene fluoride) (PVDF, Sigma Aldrich, MW ≈ 534,000 by GPC) were prepared as described previously.[18] Films were ∼300 nm thick as determined by ellipsometry, with sample preparation tailored to express the ferroelectric β-phase of PVDF as described in the literature.[19] Heavily dyed samples demonstrated no degradation in fluorescence intensity or optical density over periods of months.

5.3.2 Microscopy

Single molecule emission was collected on an inverted scanning fluorescence confocal microscope described elsewhere.[18] The 488-nm (Novalux, Protera) excitation field was circularly polarized using a $\lambda/4$ waveplate to excite all dye orientations within the films. An excitation power of 3 μW, as measured at the entrance port of the microscope, was employed and single molecules were located by raster scanning the film across the objective (Nikon, Plan-Fluor) focal volume in 100 nm steps. The emission was split by a 600-nm short-pass dichroic mirror, with the reflected (R) and transmitted (T) fields focused onto two separate avalanche photodiode detectors (APD, Perkin-Elmer SPCM-AQR-16). An overall emissive intensity threshold of 500 counts per 100 ms was used to trigger automated data collection for 150 s with a bin time of 5 ms.

5.3.3 Data Collection and Analysis

Single molecule PI data were first assessed for overall emissive intensity employing a threshold of 12 counts per 5 ms bin corresponding to three standard deviations above background. PI traces were visually examined and only those demonstrating

R/T group	wavelength range (nm)	range of ε	total molecules	non-blinking (%)[a]	discarded[b]	final sample size
0.5 and below	< 560	< 2.8	148	16 (11%)	3	129
0.5 - 1	560 - 588	2.8 - 4.2	374	61 (16%)	3	310
1 - 1.5	588 - 606	4.2 - 21	220	36 (16%)	3	181
1.5 - 2	606 - 614	21 - 47	105	25 (23%)	1	79
2 and above	> 614	> 47	176	53 (30%)	1	122
total			1023	191 (18%)	11	824

Table 5.1: Data summary for initial data collection and sorting before categorizing based on the BDIC algorithm. [a]Number of molecules without non-emissive events (non-blinking). [b]Molecules that had no emissive information (immediate photodecomposition).

emissive "activity" for at least 20 s were analyzed. In addition, only data from molecules demonstrating > 500 nm separation and single step photodecomposition were included in our analysis. An overall reflected/transmitted ratio (R/T) value was calculated by summing photons on each detector for time points where the sum of the two channels exceeded the threshold, then dividing to obtain the time averaged ratio for emissive events. The data were then categorized into five R/T categories (defined in Table 5.1) as determined for this optical configuration previously.[18] Data were collected until at least 100 molecules populated each R/T category.

The PI data were analyzed by identifying change points in emissive intensity using the Bayesian detection of intensity changes method (BDIC, see the Supporting Information) reported by Ensign and Pande.[20] This approach represents an evolution of the maximum likelihood change point detection (CPD) algorithm previously employed in our laboratory.[21] The BDIC algorithm has one adjustable level of sensitivity, negating the need for look-up tables and error matrices. BDIC also demonstrates greater accuracy at locating change points; however, neither CPD nor BDIC is able to capture short emissive events (10-30 ms) present within long non-emissive segments due to the overwhelming number of background counts relative to a few bins of signal. To detect these emissive bursts, the analysis searches for additional emissive events within long non-emissive segments (below the intensity threshold of 12 counts per bin) defined as exceeding 5 s in duration. A burst is defined as a segment with intensity greater than five standard deviations above the mean non-emissive intensity within the segment in question. In addition, bursts must span at least 10 ms.

Once change points were detected, intensity states greater than two standard deviations above the root-mean-square noise (9 counts/5 ms) were designated as emissive, and those below were designated as non-emissive. An emissive duration is defined as the total time the molecule's intensity exceeds the emissive threshold, with a corresponding definition used for non-emissive durations. Through comparison with the initial sorting threshold of 12 counts/5 ms we found that the results are not im-

pacted by choice of threshold. The BDIC algorithm calculates the average intensity between change points, thereby eliminating spurious crossings caused by noise. The 95% threshold employed avoids confusing low-intensity emissive segments with non-emissive events. Molecules that exhibited at least two emissive periods and at least one non-emissive period before photodecomposition were accepted as "blinking", and included in the final data set.

The conversion of R/T values to the wavelength of the emission maximum has been described in detail elsewhere.[18] Briefly, a mapping of the R/T ratio to emission wavelength maxima was performed by convolving ensemble NR fluorescence emission spectra in hexane, toluene and acetonitrile with the APD efficiency curves, the emission filter transmission curve, and the 600-nm dichroic reflectance and transmission curves to calculate the expected reflected (R) and transmitted (T) spectra.[11] By numerically shifting the solvent spectra and combining them to calculate a hybrid curve that takes into account the emission line shape of NR in solvents of differing polarity, the R/T ratio was transformed to the emission wavelength maximum (λ_{em}) of NR. This wavelength was then converted to energy. Finally, the relationship between energy and dielectric constant was established using the solvatochromic properties of NR. A plot of the emission energy max of NR in these solvents versus the known dielectric constant (Figure 5.1) was fit to a two-term exponential function which provides a conversion from emissive energy to dielectric constant.[18]

$$\Delta E_{00}\left(cm^{-1}\right) = 1.077 \times 10^{4} e^{-0.8\varepsilon} + 1.67 \times 10^{4} e^{-5\times 10^{-4}\varepsilon} \tag{5.1}$$

Analysis of the emissive and non-emissive event durations begins with the construction of cumulative distribution functions (CDFs), defined to be the probability that an observed event duration is between t_{min} and t, and is zero for $t < t_{min}$ and one for t greater than the longest event duration. The method of converting probability distribution functions (PDFs) to CDFs was described previously.[9] The CDF is related to the PDF through an integral and bound by zero when $t < t_{min}$ and one at

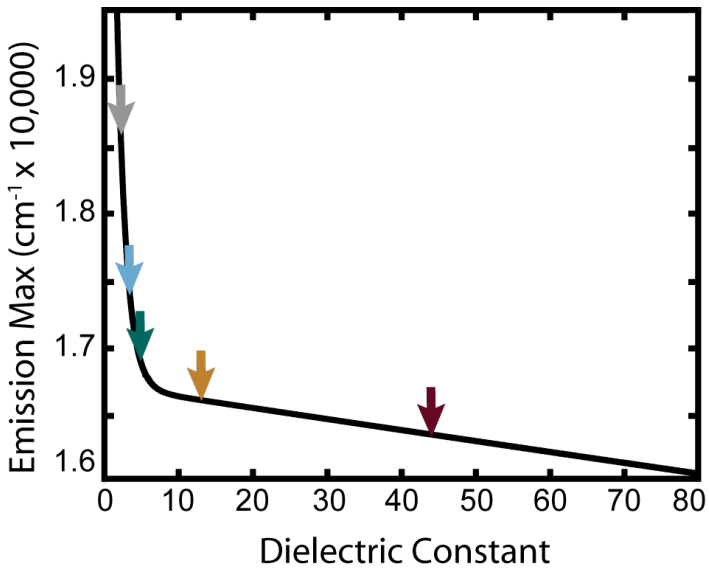

Figure 5.1: Fluorescence maximum of NR (in wavenumbers) versus dielectric constant. The solid line corresponds to Eq. 5.1. Arrows indicate the dielectric constant and average energy of the dielectric categories discussed in the text (shown here are 5 of the 8 categories); ε_1 = 2.2 (grey), ε_2 = 3.4 (cyan), ε_3 = 4.8 (teal), ε_4 = 13 (orange/brown), ε_5 = 44 (dark red). The origin of this relationship is discussed in detail in our previous work.[18]

the longest observation time.

$$\mathrm{CDF}(t) = \int_{t_m in}^{t} \mathrm{PDF}(t')\ dt' \tag{5.2a}$$

The CDF can also be calculated directly from the PI data through the correspondence of integrals to sums by counting events with duration t_i less than time t for all N events

$$\mathrm{CDF}(t) = \frac{1}{N} \sum_{i=1}^{N} 1\ \ \{t_i < t\} \tag{5.2b}$$

Similarly, the complementary cumulative distribution function is defined as:

$$\text{Complementary CDF} = 1 - \mathrm{CDF} \tag{5.3}$$

The complementary CDF is helpful when visualizing PI data as the majority of the event durations occur at short times.

5.4 Results

Table 5.1 provides a summary of the R/T distributions for NR molecules embedded in PVDF. This table is representative of the inherent distribution of NR environments provided by PVDF. The table demonstrates that approximately half of the NR molecules reside in dielectric domains where $\varepsilon < 4.2$. Table 5.1 also shows that the number of molecules that do not demonstrate PI (that is, molecules that continuously emit) increases as the dielectric constant of the environment increases.

A representative PI trace for a single NR molecule embedded in PVDF is presented in Figure 5.2. Overlaid on the total intensity is the result of the BDIC algorithm illustrating the detected intensity levels. Consistent with previous results, the single molecule trajectories depict a distribution of intensity levels.[2] Figure 5.2(a) shows the intensities of the individual transmitted and reflected channels which demonstrate temporal variation in the NR emission energy maximum. The ratios of reflected (R) intensities divided by transmitted (T) intensities were used to calculate the emission

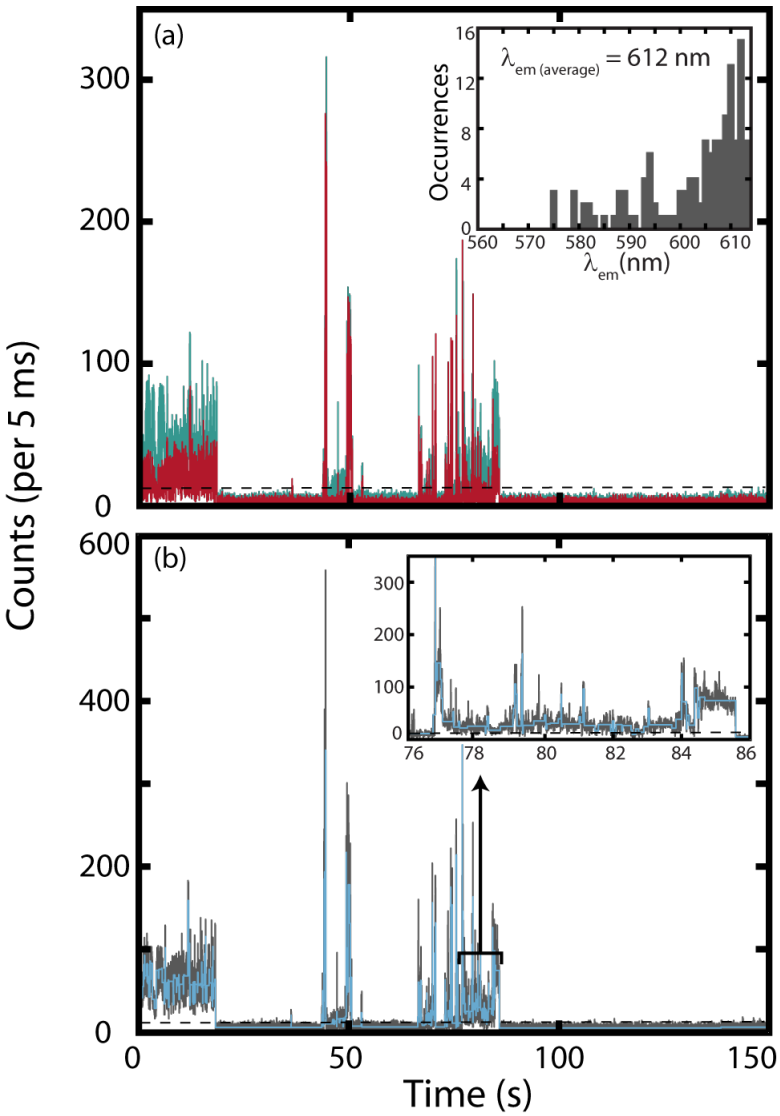

Figure 5.2: (a) Photoluminescence intermittency (PI) trace for a single NR molecule in PVDF. Displayed are reflected (teal, $\lambda_{em} > 600$) and transmitted (red, $500 > \lambda_{em} > 600$) intensities. The inset presents the histogram of emission wavelengths observed from the deconvolved emissive segments with average emission wavelength of 612 nm. (b) PI trace produced by summing the intensities from the reflected and transmitted channels (solid gray line), emissive threshold (dotted black line), and intensity states identified using the Bayesian detection of intensity change-points (BDIC) algorithm (light blue line). The inset presents a 10 s section of the trace enlarged to illustrate the BDIC algorithm's sensitivity to emissive intensity changes.

wavelength range (nm)	range of ε	median ε	category name
501 - 560	$\sim$ 2.0 - 2.8	2.2	ε_1
560 - 571	2.8 - 3.2	3	
571 - 578	3.2 - 3.6	3.4	ε_2
578 - 587	3.6 - 4.2	3.8	
587 - 596	4.2 - 5.7	4.8	ε_3
596 - 607	5.7 - 28	13	ε_4
607 - 616	28 - 58	44	ε_5
616 - 623	58 - 80	74	

Table 5.2: Data summary after categorizing[a] based on the BDIC algorithm.
[a]Each category contains 100 molecules.

energies of intensity segments identified by the BDIC algorithm lying above the emissive threshold. The data were then reduced by sorting the SMs by the time-average dielectric constant, and divided into 8 dielectric categories of 100 molecules. By averaging over the entire emissive trace, we avoid over analyzing instantaneous changes in the emission energy that may be caused by spontaneous fluctuations in the local polarity. These categories provide a basis for the analysis of PI as a function of ε and are summarized in Table 5.2. The proportion of molecules residing in average dielectric domains less than four is consistent with the results in Table 5.1.

Histograms of calculated emission energies for 5 selected dielectric categories (Table 5.2) are shown in the right hand column of Figure 5.3. This figure illustrates that the emissive segments identified by the BDIC algorithm are broadly distributed in terms of emissive energies, even for categories with a narrow range of average dielectric constants. Cumulative distribution functions (CDFs) for the emissive and non-emissive intervals are also provided in Figure 5.3. The motivation for comparing CDFs is the ability to gain mechanistic information without assuming a parametric form for the underlying probability distribution functions (PDFs). Attempts to fit the CDFs to power-law and lognormal distributions were made, but the fits were poor. We have yet to confirm an appropriate parametric form for these data. We note; however, that semi-log representations of the CDFs demonstrate significant curvature across 4 decades in time confirming that the underlying PDFs are not power-law.[14–16] The differing shapes of the emissive and the non-emissive event CDFs indicate that the underlying PDFs are different. This can likely be attributed to different mechanisms for dark state formation and decay. Additionally we see that both the emissive and non-emissive event distributions have significant probabilities at large duration times, with $\sim$10% of the non-emissive events greater than 50 s in duration. Figure 5.3(a) demonstrates that the emissive event durations continuously increases with increasing ε, while Figure 5.3(b) shows an initial increase in non-emissive event durations and subsequent decrease as ε increases.

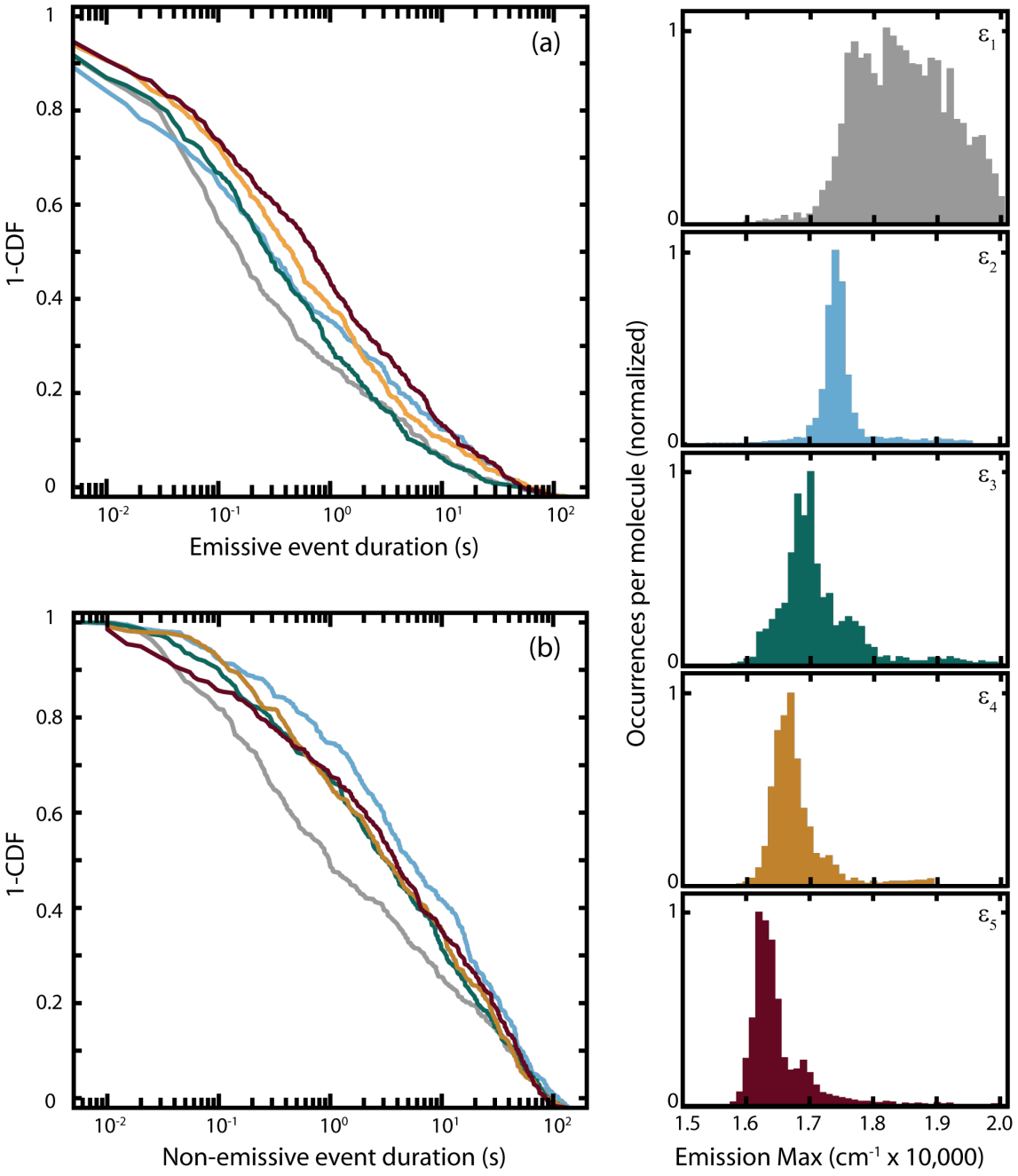

Figure 5.3: Complimentary cumulative distribution functions for the emissive (a) and non-emissive events (b) of single NR molecules in PVDF for the selected ε categories defined in Table 5.2. Color code: ε_1 (grey), ε_2 (cyan), ε_3 (teal), ε_4 (orange/brown), ε_5 (dark red). Right panel contains histograms of emission energy for the deconvolved emissive segments for each ε category. The average number of emissive segments is 44 $\pm$ 11 per molecule.

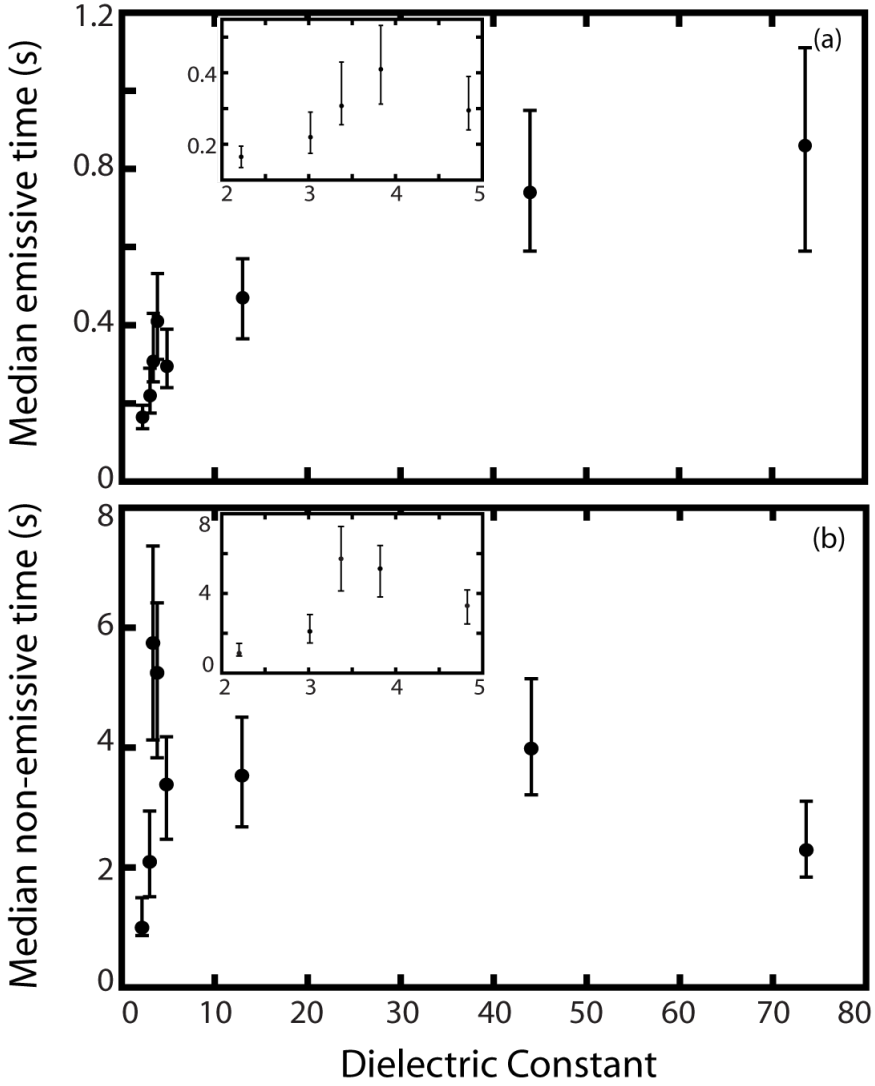

Figure 5.4: Median emissive (a) and non-emissive (b) event durations versus the average dielectric constant for each ε category defined in Table 5.1. Error bars correspond to the 95% confidence interval, calculated from 10,000 bootstrap samples. Insets on both (a) and (b) provide an expanded view of the data from $2 < \varepsilon < 5$.

To explore the relationship between event durations and ε, the median event times were calculated and plotted versus ε for all 8 dielectric categories (Table 5.2) as shown in Figure 5.4. The median is a better measure of central tendency than the mean in heavy tailed distributions as it is insensitive to outliers. The median event duration corresponds to the time at which the CDF is equal to 0.5 (see eq 5.2a). The median emissive event durations demonstrate a 5-fold increase over the range of ε observed here, with most of the increase occurring between $\varepsilon = 2$ and 4. The non-emissive event durations demonstrate a different trend, with the median event duration initially increasing with ε until 3.4, after which a decrease in the median is observed as ε continues to increase. The PI results presented here demonstrate a clear relationship between a simple measure of central tendency in the raw emissive and non-emissive event distributions and ε.

5.5 Discussion

The connection between PI and the local dielectric environment poses a significant issue in interpreting the pattern of emissive intensity exhibited by SMs. Establishing the relationship between the rates of dark-state formation and decay and the polarity of the surrounding environment provides unique insights into potential mechanisms for PI. The results presented here represent a simple, unbiased treatment of SM data which establish that the PI exhibited by NR is indeed sensitive to the local dielectric environments provided by PVDF.

In our analysis three easily implemented statistical tools are used to decompose the PI data into emissive and non-emissive durations and to present the resulting distributions graphically. First, the PI data was parsed using the BDIC algorithm to identify statistically significant changes in emissive intensity using a single adjustable parameter to tune the sensitivity of the algorithm.[20] Using the relationship between emissive energy and ε (Figure 5.1) we are able to determine the average local dielectric constant of each individual NR molecule. Second, generation of the CDFs provides the

ability to analyze changes in the distributions without having to assume a parametric from, while also allowing for a simple investigation into the functional form of the underlying PDF. Finally, by recognizing that the emissive and non-emissive event duration distributions are heavy tailed, we are able to employ the median as a simple measure of the distribution's central tendency which allows us to directly monitor the impact of ε on PI.

The NR/PVDF guest-host pair provides the opportunity to study the effect of local dielectric environment on PI without altering the chemical composition of the guest or host. This is possible as PVDF films expressed in the ferroelectric phase consist of a mixture of non-polar (α - TGTG' configuration) and polar (β - TTTT configuration) domains corresponding to a variation in dielectric constant.[22] Meanwhile, the solvatochromic properties of NR report directly on the different dielectric domains and their stability with time. This is illustrated in the right hand column of Figure 5.3. Spectral diffusion within the dielectric categories is evident by the broad tailing distributions of the emissive segment energies. This indicates that the polarity of the surrounding environment fluctuates consistent with other observations of spectral diffusion in soft and complex matrices.[2,23]

Qualitatively, the CDFs for NR as a function of ε (Figure 5.3) are markedly different for emissive versus non-emissive events. This observation suggests that the mechanism for dark-state formation and decay are not the same. This result is further confirmed through the observation of a variation in median emissive and non-emissive event durations with ε (Figure 5.4). Finally, the non-emissive durations are much longer on average than the emissive durations consistent with a larger driving force for dark-state formation relative to decay of this state.

The prevailing hypothesis for dark-state formation in organic guest-host systems is photoinduced electron transfer. To test the viability of this hypothesis for NR/PVDF, we first consider the physical properties of this guest-host pair. PVDF is aprotic and has been classified as an n-type semiconducting polymer, with electron trap

energies distributed between -0.46 and -0.73 eV below the conduction band. The ferroelectric properties of PVDF are highly dependent on the movement of electrons with filling of the electron traps proposed to be part of the mechanism for domain alignment.[24] NR has been extensively used as a solvent polarity probe, with the photo excited state of NR depending on solvent.[25] For instance, in polar aprotic solvents photoexcited NR has a planar geometry and is classified as a locally excited state with a change of $\sim$5 D in dipole moment.[13] In polar protic solvents twisted intramolecular charge transfer can occur between the donor amine and phenoxazinone moiety which quenches fluorescence.[25] Flash photolysis studies of NR in acetonitrile have confirmed the formation of a radical cation with absorption at 680 nm.[26] This observation is consistent with an oxidation potential of NR in acetonitrile of +0.95V.[27] Further electrochemical and physical parameters for NR and PVDF are presented in Table 5.3. These parameters suggest photoinduced electron transfer between electron donor NR and acceptor PVDF as a possible mechanism for PI. NR is expected to be the donor due to the favorable formation of the radical cation, and the poor capacity for aprotic solvents to stabilize anion formation. A corresponding energy level diagram derived using the parameters reported in Table 5.3 is presented in Figure 5.5. This figure illustrates that PVDF electron traps are in energetic proximity to the LUMO of NR allowing for photoinduced electron transfer between NR and these traps.

A simple model for NR/PVDF photoinduced electron transfer can be constructed using the semi-classical Marcus expression for the electron transfer rate (k_{et})[28,29]

$$k_{\mathrm{et}} = \kappa_{\mathrm{el}} \times \frac{1}{\sqrt{4\pi\lambda k_{\mathrm{B}} T}} \times e^{-(\lambda+\Delta G_{\mathrm{el}})^2/4\lambda k_{\mathrm{B}} T} \tag{5.4a}$$

$$\kappa_{\mathrm{el}} = \frac{2\pi}{\hbar}|H_{\mathrm{el}}|^2 \tag{5.4b}$$

$$H_{\mathrm{el}} = H_{\mathrm{el}}^0 e^{-\beta d_{\mathrm{cc}}} \tag{5.4c}$$

parameter	NR	parameter	PVDF
${}^{a}E^{0}_{(D_{+}/D)}$(acetonitrile)[a]	-0.95 V	binding energy[e]	-10 eV (from vacuum)
${}^{a}E^{0}_{(D/D_{-})}$(acetonitrile)[a]	-2.087 V	band gap [f]	6.5 eV
HOMO [b]	-5.5 eV	measured trap distribution[g]	-0.46 to -0.73 eV (from conduction)
LUMO[b]	-3.2 to -3.5 eV	index of refraction[h]	1.42
NR^{+} band gap[c]	1.82 eV	domain size[i]	12 Å
radii[d]	4.08 Å		

Table 5.3: Electrochemical and physical parameters for NR and PVDF. [a]Data from ref 27. [b]Data from ref 30. [c]Data from ref 31. [d]Data from ref 32. [e]Data from ref 33. [f]Data from ref 34. [g]Data from ref 24. [h]Data from ref 17. [i]Data from ref 35.

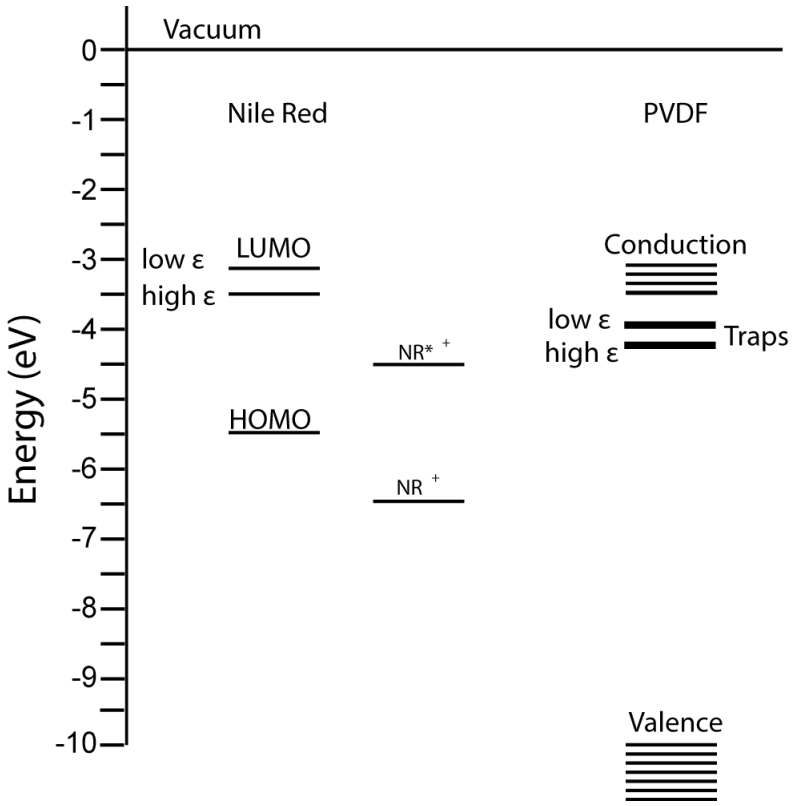

Figure 5.5: Energy level diagram for NR, NR^+, PVDF and PVDF traps. In the proposed photoinduced electron-transfer model, electron transfer from NR to traps generates NR^+ and the transferred electron "fills" the trap, promoting population of the conduction band. Electrochemical and physical parameters used to construct this diagram are listed in Table 5.3.

In the above expressions, κ_{el} represents the electronic coupling energy between the reactant and product states, λ is the reorganization energy, ΔG_{el} is the free energy, k_{B} is the Boltzmann constant, and T is temperature. The electron transfer rate has two contributing parts, the energetics of the reaction corresponding to the reorganization energy and the free energy for the reaction, and the coupling between states (κ_{el}). The electronic-coupling is modeled as shown in eq 5.4c where d_{cc} is the distance between reaction centers of the donor and acceptor and β describes the fall off of the orbital interaction between the donor and acceptor with distance. We approximated the distance to the nearest trap to be on the order of the PVDF domain size which range from 10-40 nm.[35] Using a typical value of $\beta = 0.85$ Å^{-1} we estimate H_{el} to be $\sim 1 \times 10^{-6}$ eV.[28]

The reorganization energy in eq 5.4a represents the sum of internal reorganization energy (structural changes within the donor and acceptor) and the "outer shell" reorganization energy (solvent reorganization). Under the assumption that the NR cation ground-state structure is similar to that of neutral NR, the internal reorganization energy will be small and solvent reorganization will dominate the total reorganization energy. The solvent reorganization energy is modeled using[28]

$$\lambda\,(\mathrm{eV}) = \frac{e^2}{4\pi\epsilon_0}\left\{\frac{1}{\eta^2} - \frac{1}{\varepsilon}\right\}\left\{\frac{1}{2r_{\mathrm{D}}} + \frac{1}{2r_{\mathrm{A}}} - \frac{1}{d_{\mathrm{cc}}}\right\} \tag{5.5}$$

In the above expression $r_{\mathrm{D/A}}$ are the radii of the donor and accepter species, respectively, η is the index of refraction of the solvent, e is electronic charge, ϵ_0 is the permittivity of free space, and ε is the dielectric constant of the solvent.

With regards to the driving force for the reaction the oxidation potential of the donor ($E^0{}_{\mathrm{D^+/D}}$) is known; however, to account for the fact that we are considering photoinduced electron transfer, the free energy is adjusted by the energy difference between the equilibrated neutral excited state and the neutral ground state (ΔE_{00}) of the donor. Additionally, to account for the oxidation potential of NR being measured in acetonitrile ($\varepsilon = 37$), we include a solvent separated ion pair energy term (an

approximation commonly attributed to Rehm and Weller) in determining the reaction driving force. Finally we include the energy released upon coulombic attraction of the two ions, resulting in the full expression for ΔG_{el}.[28]

$$\Delta G_{\mathrm{el}}\,(\mathrm{eV}) = e\left(E^0_{\mathrm{D}^+/\mathrm{D}} - E^0_{\mathrm{trap/trap}^-}\right) - \Delta E_{00} - \frac{e^2}{8\pi\epsilon_0}\left(\frac{1}{r_{\mathrm{D}}}+\frac{1}{r_{\mathrm{A}}}\right)\left(\frac{1}{37}-\frac{1}{\varepsilon}\right) - \frac{e^2}{4\pi\epsilon_0\varepsilon d_{\mathrm{cc}}} \tag{5.6}$$

The solvent-dependence of ΔE_{00} has been measured previously, and is given by eq 5.1.[18] While most of the parameters needed to evaluate eq 5.6 have been measured, the final quantity needed is the reduction potential of the PVDF electron traps ($E^0{}_{\mathrm{trap/trap}^-}$). Previous single emitter studies found that the power-law exponent describing the non-emissive event durations decreased with an increase in environment polarity (achieved by changing the chemical composition of the host) consistent with increased stabilization of the charge separated state in more polar environments.[15,16] This stabilization energy is proportional to ~1 - $(1/\varepsilon)$. Building on this earlier study, the reduction potentials of the traps are modeled using the field stabilization energy and the initial trap potential (E_{trap})[16]

$$E^0\left(\mathrm{trap/trap}^-\right) \approx E_{\mathrm{trap}} - \Delta E\left(1-\frac{1}{\varepsilon}\right) \tag{5.7}$$

In the above expression, $\Delta E(1 - \varepsilon^{-1})$ can be thought of as representing the width of the trap distributions, measured to be ~0.3 V, over the range of observed dielectric constants. Correspondingly, E_{trap} can be viewed as trap depth. For our model we estimate the initial trap reduction potential to be E_{trap} = -2.35 eV, consistent with resistance to filling an electron trap. Using E_{trap} as the only adjustable parameter, the median emissive events were modeled using the half-life as a proxy for the median emissive event duration (half-life = $\log(2)/k_{\mathrm{et}}$). The results of this modeling are shown in Figure 5.6. The increase in half-life with dielectric constant is in qualitative agreement with the increase in median emissive event durations as shown in Figure 5.4. Specifically, the model predicts a rapid increase in half-life as ε increases from 2 to 5,

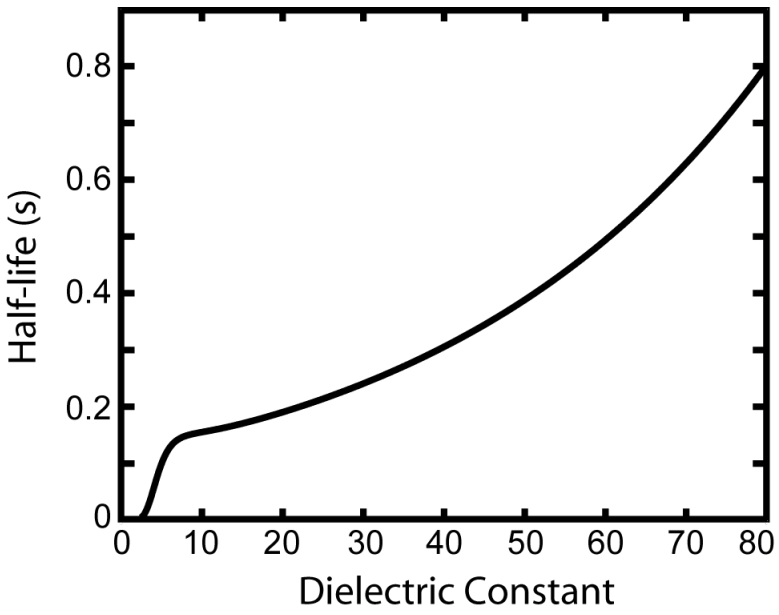

Figure 5.6: Result of modeling the photoinduced electron-transfer from NR to PVDF. The half-life serves as a proxy for the median emissive event durations. The observed trend for half-life with dielectric constant is consistent with median emissive event durations shown in Figure 5.4(a).

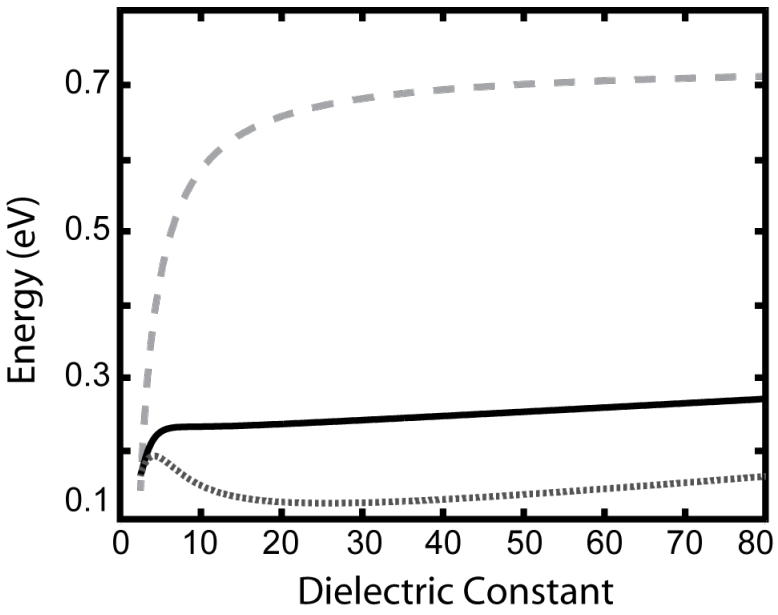

Figure 5.7: Reorganization energy λ (light grey dashed line), free energy ΔG_{el} (dark grey dotted line) and activation energy ΔG^{*} (black solid line) vs. dielectric constant. Energies were calculated using Eqs. 5.5, 5.6 and 5.8 respectively. These three parameters define the relative position and crossings of the reactants and products potentials for the electron transfer.

then a slower increase with further increase in ε. These results show that using a basic approximation for the free energy that considers the solvent effects on the oxidation and reduction potentials of the donor and acceptor, the energetics of the NR excited state, and the PVDF dynamic trap energies, the evolution in median emissive-event durations can be reproduced.

Finally, we calculate the activation energy (ΔG^*) for the electron transfer using[28]

$$\Delta G^* = \frac{\lambda}{4}\left(1 + \frac{\Delta G_{\mathrm{el}}}{\lambda}\right)^2 \tag{5.8}$$

The variation in λ, ΔG_{el} and ΔG^* with dielectric constant from our model is shown in Figure 5.7. Figure 5.7 demonstrates that $\lambda > \Delta G_{\mathrm{el}}$ at all dielectric constants indicating electron transfer occurs in the normal Marcus regime. The activation barrier increases with dielectric constant, which gives rise to a decrease in k_{et} with increasing ε. In addition, $\Delta G_{\mathrm{el}} > 0$, indicating that the reaction is "uphill" in energy. This is consistent with the observation of a larger number of non-blinking molecules with an increase in ε (Table 5.1), as well as a narrowing in the emissive energy histograms with increasing ε (Figure 5.3).

While the emissive event durations can be modeled using a photoinduced electron-transfer mechanism, the non-emissive events are not as simply described by a back electron transfer model. While the initial increase in non-emissive event durations is consistent with the hypothesis that an increase in ε provides for stabilization of the charge separated state (and correspondingly longer non-emissive event durations as others have suggested[14–16]), the subsequent decrease in non-emissive event durations as ε continues to increase is more difficult to explain. It could be that the back-electron transfer occurs through another mechanism (e.g., tunneling) as the comparison of the emissive and non-emissive event CDFs suggests. Differentiation between these electron-transfer mechanisms should be evidenced by different probability distributions functions (PDF) describing emissive and non-emissive event durations. The challenge is to directly determine the PDFs from the PI data without a priori assump-

tions of the PDF functional form, a new PI analysis tool we will report on shortly.

5.6 Conclusion

We have measured the variation in PI with local dielectric environment for NR in PVDF. Employing the NR/PVDF guest-host system a direct correlation between PI and ε can be determined while maintaining the chemical composition of both the guest and host. Through comparative analysis of the CDFs and the median event durations we find that the emissive event durations continually increase with ε. In contrast, the NR non-emissive event durations initially increase with ε, but then gradually decrease with a further increase in ε. We were able to demonstrate that the emissive event results can be rationalized using a photoinduced electron-transfer model for PI. In addition, an increase in NR photostability with an increase in ε is observed suggesting that the dielectric constant plays an important role defining the molecular photostability in PVDF.

5.7 Acknowledgements

This work was supported by the National Science Foundation (DMR-1005819). Part of this work was conducted at the University of Washington NanoTech User Facility, a member of the NSF National Nanotechnology Infrastructure Network (NNIN). EAR supported by the UW NIEHS-sponsored Biostatistics, Epidemiologic and Bioinformatic Training in Environmental Health (BEBTEH) Training Grant (T32ES015459).

5.8 Supporting Information

A more detailed description of the Bayesian Detection of Intensity Changes (BDIC) method employed in this study is available free of charge via the internet at http://pubs.acs.org.

5.8.1 Description of Bayesian Detection of Intensity Traces (BDIC)

The general assumption that molecule emission is Poisson distributed is employed. A Bayes factor is computed by comparing the probability for the hypothesis (H_1) that there is no change point in the data (D) and the probability for the alternate hypothesis (H_2) that there are two emitting states separated by a change point at time t_s. Assuming no prior knowledge of which hypothesis is likely to be true, the odds that there is a change point is simply the ratio of the two probabilities. The probabilities of the two hypotheses given the data are computed as the likelihoods, with the ratio being the Bayes factor (B):

$$B = \frac{P\left(D|H_2\right)}{P\left(D|H_1\right)} \tag{5.9}$$

After incorporating the appropriate details for the Poisson case and prior probabilities, the Bayes factor is[20]

$$B = \frac{2}{\pi}\frac{N^C}{(C-1)!\,(N-1)}\sum_{t_s}\frac{C_1!C_2!}{N_1^{C_1+1}N_2^{C_2+1}}\left[\left(\frac{C_1}{N_1}\right)^2+\left(\frac{C_2}{N_2}\right)^2\right]^{-1} \tag{5.10}$$

In the above expression t_s is the possible location of a change point, C_1 is the number of photons before the change point and C_2 is the number of photon counts after the change point, and C is the total number of photon counts in the trace. Analogously, N_1 is the number of time points before t_s, N_2 is the time points after the change point, and N is the total number of time points. The probability naturally sums over all the possible change points in the trace. The Bayes factor must be sufficiently large to contain substantial evidence for which hypothesis is appropriate. If there are only the two outcomes, then a Bayes factor of 4 is interpreted as 4:1 odds in favor of H_2, in terms of probabilities there is a $4/(4+1) \times 100\% = 80\%$ probability that H_2 is correct. We chose the authors recommendation for B = 10, as an appropriate level of skepticism at 91% confidence.

Once it is determined that a change point is probable, then the location must be

estimated. This is the maximum of the posterior probability distribution of t_s:

$$P\left(t_s|D,H_2\right) \propto \frac{C_1!C_2!}{N_1^{C_1+1}N_2^{C_2+1}}\left[\left(\frac{C_1}{N_1}\right)^2+\left(\frac{C_2}{N_2}\right)^2\right]^{-1} \tag{5.11}$$

Once the change point location is determined, a recursive algorithm is employed to find the remaining change points. Once all the change points in the trace have been located, a clean-up algorithm is employed to check the change points by calculating the Bayes parameters for the change point (i) in the trace segments between change point(i-1) and (i+1), and spurious change points are eliminated. One can go further and group the intensity states; however, we were not interested in this particular aspect at this time.

In our algorithm we explicitly calculate B and $P(t_s/D,H_2)$ by simplifying the factorials in the above equation with the following form of Stirling's approximation:

$$ln\left(n!\right) \cong \left(n+\frac{1}{2}\right) ln\left(n\right) - n + \frac{ln\left(2\pi\right)}{2} \tag{5.12}$$

This allows for the calculation of very large B values and makes possible the calculation of $P(t_s/D,H_2)$ which can also be very large. The following expressions were used in our program:

$$\begin{aligned} B =& \frac{2}{\pi}\sum_{t_s}\exp\left[C_1\ln\left(\frac{C_1}{N_1}\right)+C_2\ln\left(\frac{C_2}{N_2}\right)-C\ln\left(\frac{C}{N}\right)\right. \\ &\left.+\ln\left(\frac{\sqrt{C_1C_2\left(C-1\right)}}{N_1N_2\left(N-1\right)}\right)\right]\left[\left(\frac{C_1}{N_1}\right)^2+\left(\frac{C_2}{N_2}\right)^2\right]^{-1} \end{aligned} \tag{5.13}$$

$$\begin{aligned} P\left(t_s|D,H_2\right) =& \frac{2}{\pi}\exp\left[C_1\ln\left(\frac{C_1}{N_1}\right)+C_2\ln\left(\frac{C_2}{N_2}\right)-C\ln\left(\frac{C}{N}\right)\right. \\ &\left.+\ln\left(\frac{\sqrt{C_1C_2\left(C-1\right)}}{N_1N_2\left(N-1\right)}\right)\right]\left[\left(\frac{C_1}{N_1}\right)^2+\left(\frac{C_2}{N_2}\right)^2\right]^{-1} \end{aligned} \tag{5.14}$$

Where the constant pre-factor from the Bayes parameter is used in the calculation of $P(t_s/D,H_2)$ to keep the calculation constrained.

5.9 Bibliography

[1] Orrit, M. (2010). *Photochemical & Photobiological Sciences* **9**, 637–642.

[2] Riley, E.A., Hess, C.M., & Reid, P.J. (2012). *International Journal of Molecular Sciences* **13**, 12487–12518.

[3] Wustholz, K.L., Sluss, D.R., Kahr, B., & Reid, P.J. (2008). *International Reviews in Physical Chemistry* **27**, 167–200.

[4] Kulzer, F., Xia, T., & Orrit, M. (2010). *Angewandte Chemie International Edition* **49**, 854–866.

[5] Clifford, J.N., Bell, T.D., Tinnefeld, P., Heilemann, M., Melnikov, S.M., Hotta, J., Sliwa, M., Dedecker, P., Sauer, M., Hofkens, J., & Yeow, E.K.L. (2007). *The Journal of Physical Chemistry B* **111**, 6987–6991.

[6] Kuno, M., Fromm, D., Hamann, H., Gallagher, A., & Nesbitt, D. (2000). *The Journal of Chemical Physics* **112**, 3117–3120.

[7] Cichos, F., Von Borczyskowski, C., & Orrit, M. (2007). *Current Opinion in Colloid & Interface Science* **12**, 272–284.

[8] Frantsuzov, P., Kuno, M., Jankó, B., & Marcus, R.A. (2008). *Nature Physics* **4**, 519–522.

[9] Riley, E., Hess, C., Whitham, P., & Reid, P. (2012). *The Journal of Chemical Physics* **136**, 184508.

[10] Schmidt, R., Krasselt, C., Göhler, C., & von Borczyskowski, C. (2014). *ACS Nano* **8**, 3506–3521.

[11] Riley, E.A., Hess, C.M., Pioquinto, J.R.L., Kaminsky, W., Kahr, B., & Reid, P.J. (2012). *The Journal of Physical Chemistry B* **117**, 4313–4324.

[12] Verberk, R. & Orrit, M. (2003). *The Journal of Chemical Physics* **119**, 2214–2222.

[13] Hou, Y., Bardo, A.M., Martinez, C., & Higgins, D.A. (2000). *The Journal of Physical Chemistry B* **104**, 212–219.

[14] Schuster, J., Cichos, F., & von Borczyskowski, C. (2005). *Applied Physics Letters* **87**, 051915.

[15] Issac, A., von Borczyskowski, C., & Cichos, F. (2005). *Physical Review B* **71**, 161302.

[16] Issac, A., Krasselt, C., Cichos, F., & von Borczyskowski, C. (2012). *ChemPhysChem* **13**, 3223–3230.

[17] Brandrup, J., Immergut, E.H., Grulke, E.A., Abe, A., & Bloch, D.R. (1999). *Polymer Handbook*, Volume 89. Wiley New York.

[18] Hess, C.M., Riley, E.A., Palos-Chávez, J., & Reid, P.J. (2013). *The Journal of Physical Chemistry B* **117**, 7106–7112.

[19] Satapathy, S., Pawar, S., Gupta, P., & Varma, K. (2011). *Bulletin of Materials Science* **34**, 727–733.

[20] Ensign, D.L. & Pande, V.S. (2009). *The Journal of Physical Chemistry B* **114**, 280–292.

[21] Watkins, L.P. & Yang, H. (2005). *The Journal of Physical Chemistry B* **109**, 617–628.

[22] Bassett, D.C. (1982). *Developments in Crystalline Polymers*, Volume 2. Springer.

[23] Wustholz, K.L., Bott, E.D., Kahr, B., & Reid, P.J. (2008). *The Journal of Physical Chemistry C* **112**, 7877–7885.

[24] Chand, S., Bhatheja, R., Sharma, G., & Chandra, S. (1994). *Applied Physics Letters* **64**, 2507–2508.

[25] Freidzon, A.Y., Safonov, A.A., Bagaturyants, A.A., & Alfimov, M.V. (2012). *International Journal of Quantum Chemistry* **112**, 3059–3067.

[26] Anandan, S. & Yoon, M. (2004). *Spectrochimica Acta Part A: Molecular and Biomolecular Spectroscopy* **60**, 885–888.

[27] Miyata, S. (1997). *Organic Electroluminescent Materials and Devices*. CRC press.

[28] Kavarnos, G.J. (1993). *Fundamentals of Photoinduced Electron Transfer*, Volume 1. VCH New York etc.

[29] Marcus, R. (1990). *Journal of Physical Chemistry* **94**, 4963–4966.

[30] Liu, Y.X., Summers, M.A., Scully, S.R., & McGehee, M.D. (2006). *Journal of Applied Physics* **99**, 093521–093521.

[31] Andersson, S.B. (2011). *Applied Physics B* **104**, 161–173.

[32] Mohanty, J., Pal, H., & Sapre, A. (2003). *Photochemistry and Photobiology* **78**, 153–158.

[33] Bureau, C., Chong, D.P., Endo, K., Delhalle, J., Lecayon, G., & Le Moël, A. (1997). *Nuclear Instruments and Methods in Physics Research Section B: Beam Interactions with Materials and Atoms* **131**, 1–12.

[34] Duan, C.g., Mei, W.N., Hardy, J.R., Ducharme, S., Choi, J., & Dowben, P.A. (2003). *EPL (Europhysics Letters)* **61**, 81.

[35] Guan, F., Wang, J., Pan, J., Wang, Q., & Zhu, L. (2010). *Macromolecules* **43**, 6739–6748.

Appendices

Appendix A

ACRONYMS AND SYMBOLS

APD: Avalanche Photodiode Detector
BDIC: Bayesian Detection of Intensity Changes
CDF: Cumulative Distribution Function
CPD: Change Point Detection
DMSO: Dimethyl Sulfoxide
ε: Dielectric Constant
EO: Electro-Optical
KAP: Potassium Acid Phthalate
KS: Kolomogorov-Smirnov
λ: Wavelength
LE: Locally Excited
LUMO: Lowest Unoccupied Molecular Orbital
MLE: Maximum Likelihood Estimates, $\mathcal{L}$
NNIN: National Nanotechnology Infrastructure Network
NR: Nile Red
NSF: National Science Foundation
PDF: Probability Distribution Function
PI: Photoluminescence Intermittency
PMMA: Poly(methyl methacrylate)
PVA: Poly(vinyl alcohol)
PVDF: Poly(vinylidene fluoride)
QD: Quantum Dot
R: Reflected
S_0: Ground State
SM: Single Molecule
T: Transmitted
TICT: Twisted Intramolecular Charge Transfer
TOPS: Trioctylphosphine Sulfide
VR: Violamine R
WT.%: Weight Percent
XRD: X-Ray Diffraction

Appendix B

MICROSCOPE COMPONENTS

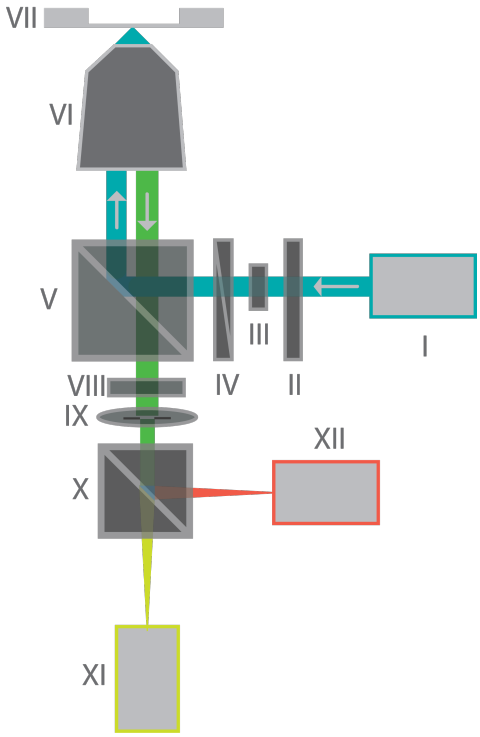

Figure B.1: Confocal fluorescence microscope in epi-geometry.
I: Continuous-wave laser, 488-nm (Novalux, Protera)
II: Excitation filter
III: Polarizing beam splitter cube, 488-nm
IV: $\lambda/4$ waveplate, 488-nm
V: Longpass dichroic mirror, 488-nm
VI: 1.3 NA objective (Nikon, Plan-Fluor)
VII: Piezoelectric nanopositioning stage (Queensgate, NPS-XY-100B)
VIII: Emission filter, 500-nm longpass (Chroma, HQ500LP)
IX: Pinhole (CVI, 75-μm diameter)
X: Dichroic mirror, 600-nm shortpass
XI: Avalanche photodiode detector, "Transmitted" (Perkin-Elmer SPCM-AQR-16)
XII: Avalanche photodiode detector, "Reflected" (Perkin-Elmer SPCM-AQR-16)

VITA

Chelsea Hess Haupt (formerly Chelsea Marie Hess) is the daughter of Christine and Howard Hess, born in Reno, Nevada on July 18, 1988. After receiving her high school diploma from Truckee High School in Truckee, California in 2006 she attended the University of Washington in Seattle, Washington where she earned a Bachelor of Science in Chemistry in 2010. Following her undergraduate degree she remained at the University of Washington for graduate school where she obtained a Master of Science in Chemistry in 2013 and a Doctor of Philosophy in 2015.